ISTANBUL TECHNICAL UNIVERSITY ★ GRADUATE SCHOOL OF SCIENCE
ENGINEERING AND TECHNOLOGY

NUMERICAL INVESTIGATION OF POWER CYLINDER LUBRICATION AND FRICTIONAL PERFORMANCE CONSIDERING PISTON ELASTIC DEFORMATIONS

Ph.D. THESIS

Özgür GÜNELSU

Department of Mechanical Engineering

Mechanical Engineering Doctorate Programme

MARCH 2016

ISTANBUL TECHNICAL UNIVERSITY ★ GRADUATE SCHOOL OF SCIENCE
ENGINEERING AND TECHNOLOGY

NUMERICAL INVESTIGATION OF POWER CYLINDER LUBRICATION AND FRICTIONAL PERFORMANCE CONSIDERING PISTON ELASTIC DEFORMATIONS

Ph.D. THESIS

Özgür GÜNELSU
(503062011)

Department of Mechanical Engineering

Mechanical Engineering Doctorate Programme

Thesis Advisor: Assoc. Prof. Dr. Özgen AKALIN

MARCH 2016

İSTANBUL TEKNİK ÜNİVERSİTESİ ★ FEN BİLİMLERİ ENSTİTÜSÜ

GÜÇ SİLİNDİRİ YAĞLAMA VE SÜRTÜNME PERFORMANSININ PİSTON ELASTİK DEFORMASYONLARININ ETKİSİ İLE BİRLİKTE SAYISAL İNCELENMESİ

DOKTORA TEZİ

Özgür GÜNELSU
(503062011)

Makina Mühendisliği Anabilim Dalı

Makina Mühendisliği Doktora Programı

Tez Danışmanı: Doç. Dr. Özgen AKALIN

MART 2016

Özgür GÜNELSU, a Ph.D. student of ITU Graduate School of Science Engineering and Technology 503062011 successfully defended the thesis entitled “NUMERICAL INVESTIGATION OF POWER CYLINDER LUBRICATION AND FRICTIONAL PERFORMANCE CONSIDERING PISTON ELASTIC DEFORMATIONS”, which he prepared after fulfilling the requirements specified in the associated legislations, before the jury whose signatures are below.

Thesis Advisor : **Assoc. Prof. Dr. Özgen AKALIN** ....
Istanbul Technical University

Jury Members : **Prof. Dr. Cem SORUŞBAY** ....
Istanbul Technical University

Asst. Prof. Dr. Osman Akın KUTLAR ....
Istanbul Technical University

Prof. Dr. İrfan YAVAŞLIOL ....
Yıldız Technical University

Prof. Dr. İsmail LAZOĞLU ....
Koç University

Date of Submission : 25 January 2016
Date of Defense : 4 March 2016

To my family,

FOREWORD

First of all, I would like to thank my Advisor Dr. Akalın for not only his academic support, but also for his sincere efforts to mentally keep me in this study.

I also thank all my colleagues at ITU, Automotive Division, for encouraging me to continue my studies and for all the knowledge that they shared with me about my field of work and life.

I would like to mention that my life during this thesis study would be far more difficult without the people of ITU Initiative of Assistant Solidarity.

I want to thank the people of IZTECH (Izmir Institute of Technology) for the friendly atmosphere which helped me work in peace.

In addition, thanks to all my friends who made my life better with either their encouragement to end my thesis or their existence only.

And the most important and special thanks go to my parents Gülşen and Cevat for their patience and their great support to my insistence in academic studies as well as to all thirty-five years of my life, and to my wife, Seda, for everything she has been for the past 6 years.

This thesis has been completed under the grant provided by "The Scientific and Technological Research Foundation of Turkey" (TUBITAK Project No. 104M274). The scholarship and financial support by this grant is gratefully acknowledged.

March 2016

Özgür GÜNELSU
M.Sc

TABLE OF CONTENTS

Page

ABBREVIATIONS

ATS : Anti-thrust side (Minor thrust side)
BC : Boundary condition
BDC : Bottom dead center
CCD : Charge-coupled device
CPU : Central processing unit
DLC : Diamond-like carbon
EHD : Elastohydrodynamic
FC/PC : Fiber channel/Physical contact
FD : Finite difference
FE : Finite element
fmep : Friction mean effective pressure
FTDC : Firing top dead center
ICE : Internal combustion engine
imep : Indicated mean effective pressure
JFO : Jakobsson-Floberg-Olsson
LHS : Left hand side
PSD : Piston secondary dynamics
RHS : Right hand side
SI : Spark ignition
TDC : Top dead center
TS : Thrust side (Major thrust side)

LIST OF TABLES

LIST OF FIGURES

Page

LIST OF SYMBOLS

c : Skirt clearance

d_{ba} , d_{ba} : Local deviations from nominal skirt diameter due to barrel and oval profiles

d_C : Horizontal distance to piston pin center from crankshaft axis (crank offset)

d_{CM} : Distance to piston mass center from cylinder axis

d_P : Distance to piston pin center from cylinder axis (pin offset)

d_{th} , d_{el} : Local changes in skirt raidus due to thermal and elastic deformations

e_b , $\dot{e}_b$, $\ddot{e}_b$: Eccentricity w.r.t. cylinder axis, lateral velocity and acceleration of piston skirt bottom

e_{CM} : Eccentricity of piston mass center w.r.t. cylinder axis

e_P : Eccentricity of piston pin center w.r.t. cylinder axis

e_t , $\dot{e}_t$, $\ddot{e}_t$: Eccentricity w.r.t. cylinder axis, lateral velocity and acceleration of piston skirt top

g : Gravitational acceleration

h , H : Nominal film thickness (dimensional and non-dimensional)

h_{max} : Supply oil thickness

h_{min} : Minimum film thickness

h_T : Local film thickness

h_2 : Local film thickness at outlet location

h_3 : Local film thickness at rupture location

m : Piston mass

m_B : Connecting rod mass

n : Rotational speed

p , P : Local pressure (dimensional and non-dimensional)

p_c : Asperity contact pressure

p_L : Lubricant film leading edge pressure

p_T : Lubricant film trailing edge pressure

p_w : Wavy contact pressure

r : Crank radius

t , T : Time (dimensional and non-dimensional)

x , X , x' : Axial position (dimensional, non-dimensional and fixed to piston)

x_f , x_4 : Lubricant film reformation location

x_i , x_1 : Lubricant film inlet location

x_o , x_2 : Lubricant film outlet location

x_p , x_3 : Lubricant film rupture location

y , Y : Circumferential position (transverse direction for lubricant flow) (dimensional and non-dimensional)

y_p : Lubricant film rupture location in circumferential direction

z , z' : Lateral position (global and fixed to piston)

A_{Bx} , A_{Bz} : Connecting rod lateral and axial acceleration

A_{Px} , A_{Pz} : Piston lateral and axial acceleration

AN , AS , AW , AE , AP , S : Coefficients of discretized Reynolds equation

C , D , DC , DD : Parameters used in the FD solution of Reynold's equation

C_{CM} , C_P : Distance to piston mass center and wrist-pin axis from piston skirt top

C_{MB} : Distance to connecting rod mass center from big end bearing axis

C_{MP} : Connecting rod length (between bearing axes)

E : Modulus of elasticity

F_f : Tangential force acting on the piston skirt

F_g : Gas force

F_h : Normal force acting on the piston skirt

F_{Mx} : x-component of reaction force on the connecting rod applied by the crankshaft

F_{Mz} : z-component of reaction force on the connecting rod applied by the crankshaft

F_{rx} : x-component of reaction force on the piston applied by the connecting rod

F_{rz} : z-component of reaction force on the piston applied by the connecting rod

H_σ : Film thickness ratio ($\frac{h}{\sigma}$)

I_B : Connecting rod moment of inertia around mass center

I_P : Piston moment of inertia around pin axis

L : Skirt length

L_{lub} : Effective lubricated length

M_f : Moment acting on the piston due to F_f

M_h : Moment acting on the piston due to F_h

M_{pin} : Moment due to piston pin friction

N : Rotational speed

P_c , P_g	Crankcase and combustion chamber pressures
P_w	Wavy contact load
R	Piston radius
U_1 , U_2	Absolute velocities of sliding surfaces
U , U^*	Piston velocity (dimensional and non-dimensional)
V_{r1} , V_{r2}	Surface roughness variance
α	Piston circumferential coordinate
α_{lub}	Circumferential length of lubricated zone
β	Angular position of connecting rod w.r.t cylinder axis
β^*	Squeeze film factor
γ	Surface roughness orientation factor
δ	Indentation of a wave peak
ζ	Angle of tilt of piston
η	Dynamic viscosity
θ	Crankangle
κ	Angle of inclination of cylinder w.r.t Earth's gravity
λ	Wave length of surface waviness
μ	Kinematic viscosity
σ , σ^*	Surface roughness (dimensional and non-dimensional)
τ	Viscous shear stress
ϕ_c	Contact factor
ϕ_f	Correction factor
ϕ_x , ϕ_y	Pressure flow factors
Φ_s , ϕ_s	Shear flow factors (for a single surface and for two surfaces in contact)
Φ_{fs} , ϕ_{fs}	Shear stress factors (for a single surface and for two surfaces in contact)
χ	Angular coordinate
ω	Crank speed
Ω	Surface waviness

NUMERICAL INVESTIGATION OF POWER CYLINDER LUBRICATION AND FRICTIONAL PERFORMANCE CONSIDERING PISTON ELASTIC DEFORMATIONS

SUMMARY

This study aims to predict the behavior of an oil-lubricated piston reciprocating inside a cylinder in the context of its lateral motion, and to state its contribution to total piston assembly friction. For this purpose, a detailed model was constructed and a MATLAB code was written solving secondary motion of a piston in mixed lubrication and calculating friction losses arising from skirt-liner interaction. In regard to its effects on the operation of the piston, skirt lubrication was focused on. Effects of surface finish of skirt and liner were taken into account using the modified form of Reynolds equation with pressure and shear flow factors. An asperity contact model was introduced for the effect of solid-to-solid contact of surfaces. In addition, continuity of lubricant film between skirt and liner surfaces was investigated. Reynolds flow separation approach was used to determine film rupture boundary for the two-dimensional flow of lubricant. Thermal expansion of the piston was calculated to obtain the skirt profile under steady-state engine running conditions for a known cold profile. Change in the lubricated surface of skirt during operation were taken into account by calculating the piston's elastic deformation under the effect of lubricant pressure and contact loads at each time step.

Simulation results for a number of cases were presented for effects of the skirt profile. Different cases are obtained by changing barrel form, the bulge location and ovality of piston. Setting the radius at the bulge location as the nominal skirt radius, radial reduction towards skirt top and bottom were increased and reduced for the effect of barrel form only. A second set was obtained by moving the bulge location up and down while the radial reduction due to barrel form was kept constant as moved away from the bulge. The third set contains two different oval profiles with increased and reduced radial drops in the circumferential direction while the barrel profile on the plane of symmetry which is perpendicular to pin axis was kept constant. Resulting friction losses were compared and used to suggest an alternative skirt profile for improved lubrication performance. Furthermore, oil viscosity which has transverse effects on hydrodynamic lubrication was selected as another focus design parameter. The model was tested to be used as a tool to predict an optimized viscosity for its effects on viscous shear and solid-to-solid contact behavior.

These analysis were carried out with two different inlet oil supply conditions. 20 μm oil thickness available at the leading edge was assumed for partially-flooded inlet whereas 40 μm was taken for fully-flooded condition.

Generally it was found that critical period in terms of frictional loss and solid contact started at around 40°CA after FTDC. Boundary friction was more dominant in partially-flooded inlet cases whereas hydrodynamic losses were higher for fully-flooded inlet ones, as expected.

In partially-flooded inlet analysis, minimum and maximum frictional loss values were found for the change in oval form of the skirt. It was also seen that baseline oil type can be used since lower viscosities results in increased power loss and higher one offered negligible benefit. In the end, a skirt profile was suggested with the combination of three parameters. However, the friction mean effective pressure was found to be higher than the value obtained by only changing the oval form. Therefore, it was concluded that effects of changes in skirt profile parameters were not linear for the given engine operation condition with the partially-inlet. A reduction in oval form alone could be more beneficial in terms of frictional power loss.

Fully-flooded inlet resulted in significantly less frictional power loss due to reduced solid contact. Barrel form had a transverse effect in this case compared to partially-flooded inlet. In addition, it was seen that reduction in power loss with increased oil viscosity was not negligible this time. Combined effect of skirt profile parameters and oil type were observed to give the best frictional performance for the suggested case with a fully-flooded inlet.

In conclusion, this study presented a series of recommendations for selected design parameters defining skirt profile and lubricant viscosity in order to achieve an improved frictional performance of a medium-duty diesel engine piston. A comprehensive model for skirt lubrication and piston secondary dynamics were built and used for case studies. Keeping in mind that the design process of an ICE power cylinder requires an integrated analysis of any design parameter with its effects on the performance of other important components such as rings as well, the resulting model can be a base tool to be developed further for use in more advanced analysis.

GÜÇ SİLİNDİRİ YAĞLAMA VE SÜRTÜNME PERFORMANSININ PİSTON ELASTİK DEFORMASYONLARININ ETKİSİ İLE BİRLİKTE SAYISAL İNCELENMESİ

ÖZET

Geleneksel içten yanmalı motorlar ve bazı kompresörlerde olduğu gibi öteleme hareketli piston kullanan makinalarda, silindir ekseni boyunca öteleme hareketinin yanında piston bu eksene dik olarak yanal yönde de hareket eder. Piston eteği ile silindir arasındaki boşluğun mikron mertebelerinde olduğu düşünlürse, ortaya çıkan yanal hareket de çok küçük olmaktadır. Ancak, bu hareket pistonun ve segmanların yağlama performansı, dolayısıyla sürtünme kayıpları ve aşınmalar üzerindeki belirleyiciliği ile motor performansı ve ömrü üzerinde oldukça etkilidir. Piston-segman-gömlek yüzeyleri arasındaki etkişim, motorun verimini doğrudan etkileyen bir faktör olarak ve aynı zamanda yakıt ekonomisi, egzoz gazı emisyonları ve gürültü açısından da her daim incelenmeye devam edilecek bir konu olacaktır.

Bu çalışma silindir içinde hareket eden içten yanmalı motor pistonunun yanal hareketini ve etek sürtünmesinin güç silindirinin toplam sürtünme kayıpları içindeki payını belirlemeyi amaçlamaktadır. Bu amaçla, detaylı bir model oluşturularak karma yağlama rejiminde piston ikincil dinamiğini çözen ve piston eteği ile silindir duvarı arasındaki etkileşimden kaynaklanan sürtünme kaybını hesaplayan bir MATLAB kodu yazılmıştır. Piston hareketi üzerindeki etkilerinin öneminden dolayı etek yağlaması üzerinde özellikle durulmuştur. Pürüzlü yüzeyler ile pürüzsüz yüzeyler arasındaki akışların karşılaştırılmasına olanak sağlayan basınç ve kesme akış faktörleri eklenerek uyarlanmış Reynolds denklemi kullanılarak etek ve gömlek yüzey işleme özelliklerinin yağ filmi üzerindeki etkisi hesaba katılmıştır. Yüzey pürüzlerinin katı temasının modellenmesi amacıyla bir pürüz temas modeli eklenmiştir. Bunun yanında, yağ filminin sürekliliği de incelenmiş ve iki boyutlu akışta yağ filminin koptuğu sınır, Reynolds akış ayrılması yaklaşımı kullanılarak hesaplanmıştır. Oda sıcaklığındaki profili bilinen soğuk piston eteğinin durağan çalışma şartlarındaki sıcaklıklarda göstereceği değişim ısıl genleşmesinin hesaplanması ile elde edilmiştir. Yağ basıncı ve temas yükleri altında gerçekleşen ve çalışma esnasında etek yağlama bölgesindeki profilin değişmesine yol açan elastik deformasyonların etkisi ise her zaman adımında anlık değerlerinin hesaplanması ile modele katılmıştır.

Model ile elde edilen ve farklı şartlara ait sonuçlar verilerek karşılaştırılmıştır. Etek profilinin etkisinin incelenmesi amacıyla tepe noktası ile beraber fıçı profili ve pistonun ovalliği değiştirilerek farklı örnek durumlar ortaya çıkarılmıştır. Sadece fıçı profilin incelendiği durum çalışmasında, tepe noktası nominal etek çapı olmak üzere, üst ve alt noktalara doğru olan çap daralması değiştirilerek, arttırılmış ve azaltılmış fıçı etkisi yaratılmıştır. Tepe noktasının konumunun etkisi için ikinci bir inceleme grubu, fıçı formun bozulmadan aşağı ve yukarı kaydırılması ile elde edilmiştir. Üçüncü grup ise perno eksenine dik olan simetri düzlemi üzerindeki profil sabit olmak üzere çevresel yönde gerçekleşen çap daralmasının arttırılıp azaltılması ile oluşan oval profil değişimini içermektedir. Bu farklı profiller ile elde edilen sürtünme kayıpları

karşılaştırılmış ve daha yüksek yağlama performansı sağlayacak alternatif bir etek profili önerilmiştir. Bunun yanı sıra, hidrodinamik yağlama üzerinde iki yönlü etkisi olan yağ viskozitesi de incelenen tasarım parametrelerinden biri olarak seçilmiştir. Viskozitenin artması ile azalan katı temasına karşı viskoz kesme kuvvetlerinin artış göstermesi beklenen bir sonuçtur. Model, bu paramatrenin nihai etkisinin hesap edilerek optimum değerler önerilmesi amacıyla kullanılmıştır.

Hidrodinamik yağlamaya etki eden önemli faktörlerden biri de pistonun hareket yönüne göre önünde mevcut olan, silindir duvarı üzerindeki yağ miktarıdır. Yukarıda anlatılan farklı tasarımlar iki farklı giriş yağ miktarı sınır şartı için ayrı ayrı incelenmiştir. İlki kısmi yağlama olarak adlandırılmış olan 20 μm yağ film kalınlığı, ikincisi ise 40 μm ile tam yağlama şartı olarak alınmıştır. Bu şekilde etek ve silindir arasına yağ taşıyan mekanizmaların piston sürtünmesine etkisi de araştırılmıştır.

Elde edilen sonuçlara bakıldığında genel olarak sürtünme kaybı ve yüzeylerin katı teması açısından kritik zaman aralığının ateşlemenin gerçekleştiği üst ölü noktadan yaklaşık 40° krank mili açısından itibaren başladığı görülmüştür. Ayrıca beklendiği üzere, kısmi yağlama şartları altında sınır yağlamanın sürtünme kaybı üzerinde daha etkili olduğu, tam yağlama durumunda ise hidrodinamik kayıpların arttığı gözlemlenmiştir.

Kısmi yağlama şartlarında, yağ viskozitesinin düşmesi sürtünmeyi arttırdığı, yükselmesinin de belirgin bir iyileşme sağlamadığı görüldüğünden refereans motor yağının kullanılabileceği sonucuna varılmıştır. Ayrıca, incelenen durumlar arasında en düşük ve en yüksek sürtünme kayıpları etek oval formunun, sırasıyla, azaltılmış ve arttırılmış durumlarında gözlemlenmiştir. Fıçı profilin artması ve tepe noktasının etek uzunluğunun %10'u kadar aşağı kaydırılması ile sürtünme kayıplarının az da olsa düştüğü görülmüştür. Ayrı ayrı incelenen bu üç parametrenin en iyi sonucu verdiği durumların birleştirilmesi suretiyle alternatif bir etek profili önerilerek model tekrar çalıştırılmıştır. Ancak elde edilen sürtünme kaybının oval formun tek başına azaltılarak elde edildiği durumdan daha yüksek olduğu görülmüştür. Bu durumda, kısmi yağlamada ve verilen motor çalışma şartlarında incelenen etek profil parametrelerindeki değişimin etkisinin lineer olmadığı sonucuna varılmıştır. Yalnızca oval formun değiştirilmesi sürtünme kayıpları açısından en olumlu etkiyi yapabilmektedir.

Piston eteği ile silindir arasına giren yağ miktarının artması ile katı temasının azalması sonucu sürtünme kayıplarında belirgin bir iyileşme elde edilmiştir. Tam yağlama şartlarında, fıçı profilindeki değişimin kısmi yağlamaya göre ters bir etki gösterdiği gözlemlenmiştir. Bunun yanında, yağ viskozitesindeki artışın da tam yağlama için ihmal edilemeyecek kadar etkili olduğu bulunmuştur. Alternatif etek profili ve yüksek viskoziteli yağın kullanıldığı önerilen durum için bu çalışma şartlarında oldukça düşük sürtünme kaybı sonuçlarına varılabileceği görülmüştür.

Sonuç olarak bu çalışma ağır ticari karayolu taşıtlarında kullanılan bir dizel motorun sürtünme performansını iyileştirecek şekilde etek profilini belirleyen tasarım parametreleri ve yağ viskozitesi için değişiklik önerileri öne sürmüştür. Bu öneriler, oluşturulan kapsamlı yağlama modeli ve piston ikincil dinamiği çözücüsü yardımıyla incelenmiştir. İçten yanmalı motor güç silindirinin tasarımında, herhangi bir tasarım parametresinin piston grubunun özellikle segman gibi diğer önemli parçaları üzerindeki etkilerinin de dikkate alınması gerekliliğinin farkında olmak kaydıyla, elde edilen modelin daha gelişmiş analizlerde kullanılmak üzere geliştirilebilecek temel bir araç olarak kullanılmaya uygun olacağı söylenebilir.

1. INTRODUCTION

In reciprocating piston machines such as conventional internal combustion engines and reciprocating compressors, beside the reciprocation inside the cylinder in the axial direction, piston also moves in the lateral direction causing piston secondary motion. Considering the clearance between piston skirt and cylinder liner, the displacement of the piston in the lateral direction is very small. However, engine performance is greatly affected by secondary motion of the piston, since it determines the conditions of lubrication at the piston skirt and rings. Depending on the lubrication quality, engine friction loss in piston–piston ring-cylinder liner assembly constitutes 25-50% of the total mechanical losses in an internal combustion engine as can be seen in Figure 1.1 [2]. In terms of mechanical power generated by the engine, loss in piston-cylinder liner interaction can be estimated as 5-6% of the indicated power (Figure 1.2) [3]. Therefore piston and ring friction can be a major draw-back for engine performance.

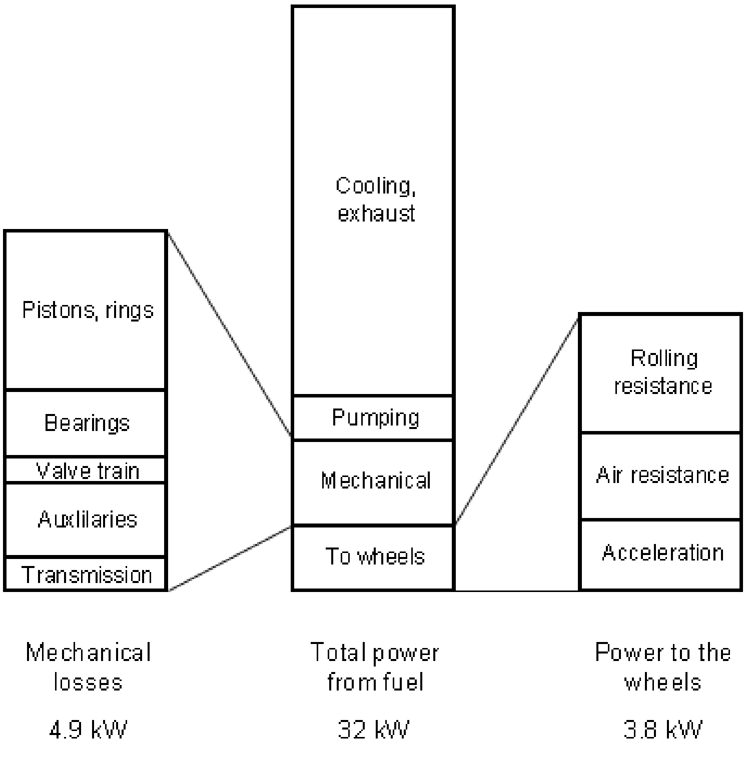

Figure 1.1 : Fuel energy utilization for a medium size passenger car during an urban cycle [2].

Furthermore, skirt lubrication has significant effects on fuel economy, oil consumption, exhaust emissions, durability and noise emission.

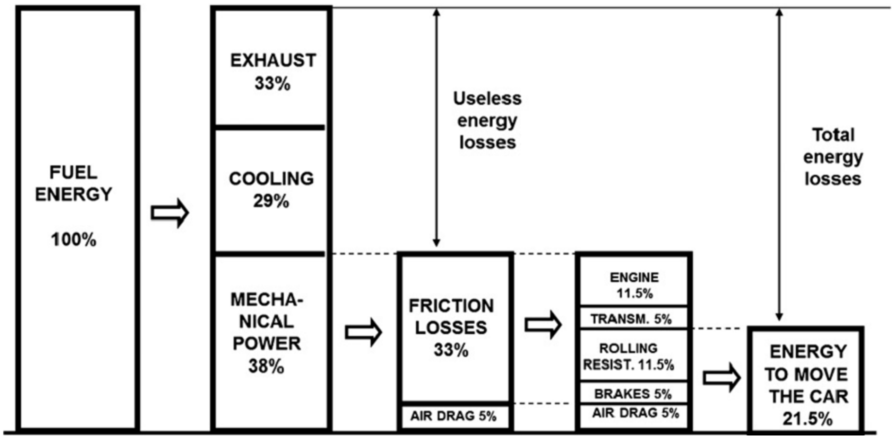

Figure 1.2 : Breakdown of passenger car energy consumption [3].

Piston secondary dynamics also plays an important role in noise emission. When the lateral speed of the piston is over certain values as it approaches the cylinder wall, oil film fails to cushion the piston skirt and it hits the bore causing piston slap [14, 15].

Some design parameters such as skirt profile, piston pin offset, crank offset, quality of the lubricated surfaces and oil characteristics are worth mentioning for the smooth operation of piston in the context of its secondary motion [4–7, 16].

1.1 Effects of Piston Secondary Motion on Engine Performance

Friction loss in piston-cylinder assembly is one of the major factors that reduce the mechanical efficiency of a power cylinder system. Providing a lubricant film between piston surface and cylinder liner acts in favor of low friction. However, since piston is subjected to a transient motion throughout a complete crank cycle, it is difficult to maintain a continuous film all over the piston skirt surface. Therefore piston design should be optimized in order to minimize the overall friction loss for a complete crank cycle, at every engine load and speed.

Wear is another result of the interaction of the sliding surfaces and it should be considered at the design stage for increased durability. Even when the two surfaces are completely separated with a lubricant film in-between, viscous wearing occurs. However it is insignificant when compared to wear due to dry contact. In other words, it is the rupture of fluid film between the surfaces that causes wear of piston skirt, rings and liner.

Film rupture can be avoided by having large clearance filled with high amount of lubricant, but in this case the problem of excessive oil consumption arises. One of the mechanisms that give rise to oil consumption is the oil-throw off from the top ring. While the piston is moving towards TDC, top ring on an ICE piston makes use of the oil left on the cylinder wall during the movement of the piston towards BDC. If the fluid film on the cylinder wall is thicker than the instantaneous clearance between ring and bore, the ring scrapes the excessive oil. Some of the oil accumulated on the ring escapes to the combustion chamber under the effect of high acceleration. As the clearance increases, the extent of piston's capability to move in the lateral direction and the amount of oil scraped increase. High oil consumption is also undesired since it makes the control of exhaust emissions more difficult. Therefore oil consumption in the piston-piston ring-cylinder assembly is one of the major design criteria [17, 18].

1.2 Parameters Affecting Piston Secondary Motion

The parameters affecting piston secondary motion can be investigated under three topics:

- Geometry
- Lubrication characteristics
- Elastic and thermal deformations

Geometry is the major parameter since it also determines the quality of lubrication and the extent of deformations with material properties. Geometric properties of primary importance are radial clearance, piston skirt length and barrel profile, pin and crank offset.

Radial clearance factor has already been discussed in the previous section, but barrel-shaped profile is not mentioned. Barrel shape of the lubricated surfaces provides a convergent passage during both upstroke and downstroke (Figure 1.3). This convergent passage is the major characteristic that forces the lubricant film to develop hydrodynamic pressure.

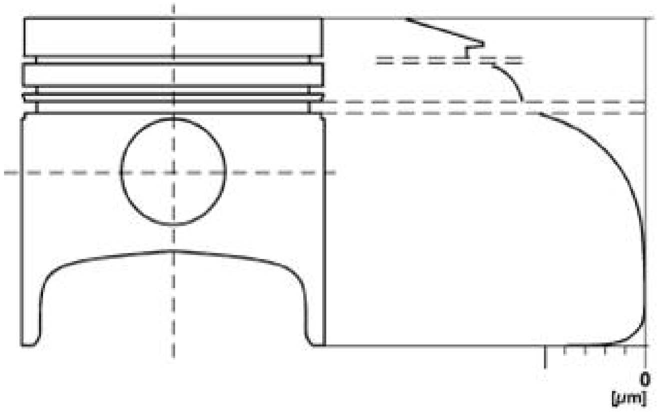

Figure 1.3 : Barrel-shaped piston skirt.

Piston skirt maintains the smooth operation of the piston and rings by keeping piston tilt at low values. In addition, skirt provides a large surface for the support of lubricant film. Increasing the skirt length reduces the tilt and increases the load carrying capacity of the lubricant. However, it also increases the friction force and piston mass. Therefore it should be handled as an optimization problem.

Offsetting the pin or crank axes from the cylinder axis, are two of the methods two smoothen piston lateral motion. Due to varying gas pressure acting on piston top during the cycle, higher lateral forces are generated on the piston pin in one direction. A crankshaft offset towards minor thrust side (Figure 1.4), leads to lower thrust, and higher anti-thrust side forces, in addition to slight improvement in combustion performance of internal combustion engines. Offsetting the pin axis changes the

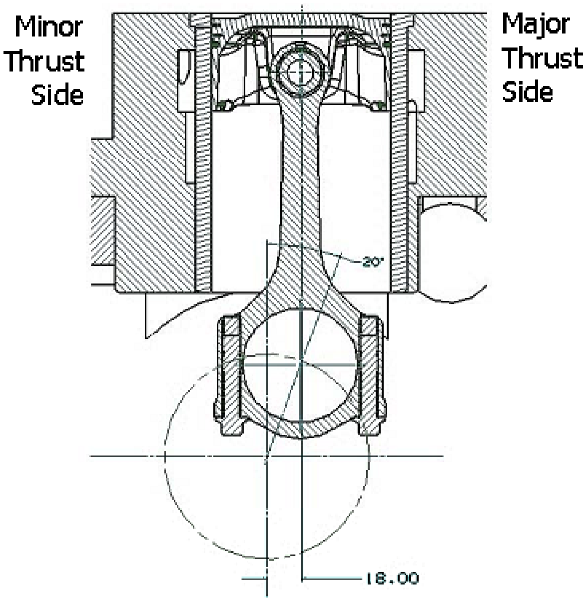

Figure 1.4 : Crankshaft offset towards minor thrust side [4].

moment on the piston due to gas pressure and is a helpful design application to prevent excessive tilt of the piston.

In lubrication quality, side clearance, barrel profile, surface finish and oil properties are important parameters. Side clearance and barrel profile have already been discussed above.

Asperities on the lubricated surfaces are in the orders of one tenth of microns [2, 16]. These microscale roughness characteristics are considered to have no effect on lubrication quality if the film thickness is approximately 7-8 times higher [1, 11]. However, even though there is not sufficient theoretical studies on the subject, experimental investigations reveal that macroscale surface finish applications such as honing, coating or laser surface texturing provide considerable improvement in lubrication characteristics. Microscale surface asperities are effective in relatively small clearance applications. Both microscale and macroscale surface irregularities, to some extent, aid hydrodynamic load carrying capacity by acting as barriers to the flow, but in friction point of view, especially in mixed and boundary lubrication regimes, they cause an increase in power loss due to solid-to-solid contact [16, 19].

Viscosity is the main characteristic determining the damping and frictional behavior of the lubricant. Decreasing the viscosity is advantageous for viscous friction; however it decreases damping, and thus load carrying capacity of the lubricant and leads to lower film thicknesses.

1.3 Literature Review

1.3.1 Studies on piston secondary dynamics and skirt lubrication

Reciprocating engine piston friction losses have been investigated since the middle of the last century. Secondary dynamics has been in focus for vibration and oil consumption concerns. In years, friction loss and wear have become as important as the other topics with the concerns of fuel economy and engine lifetime [20–24].

In the early studies, the piston was rigid and not lubricated. Lubrication effects and elastic deformations are gradually added to the models.

Greenwood and Tripp [25] developed the asperity contact model for two rough surfaces. Most models used to consider one of the contacting surfaces to be smooth. Elastic deformations of the asperities were also taken into account in the model.

Patir and Cheng [1, 11] modified the Reynolds equation adding the effect of three-dimensional roughness on hydrodynamic lubrication. They introduced pressure and shear flow factors and a factor for the extent of combined roughness of both surfaces into the equation. Effects of orientation of the surface patterns were also considered in the determination of flow factors.

Average Reynolds equation was used by Zhu et al. [13, 26] in the analysis of piston skirts in mixed lubrication. In this study, flow factors were defined in terms of surface waviness and roughness parameters, based on a geometrical model approximating the surface profile of a piston as sawtooth-shaped transversely-oriented identical waves and asperities. For the case of contact of surfaces, wavy and asperity contact pressures were discussed considering elastic deformations, however deformations were not included in the solution in this first part of the study. Coulomb friction was assumed for the boundary film lubrication in possible solid-to-solid contact between piston skirt and cylinder bore.

A comprehensive skirt lubrication model was constructed by Keribar and Dursunkaya [27] for further use in a piston secondary dynamics analysis. Mixed lubrication was modeled without surface roughness effects on flow, using average Reynolds equation. Elastic deformations could be included in the solution as an input. In order to take the oil starvation into account, a parameter called the extent of lubrication was also used as an input and Reynolds equation was modified by a coordinate transformation for partially-flooded cases. Cavitation was treated by half-Sommerfeld condition as in fully-flooded case, even in partially-flooded lubrication conditions. This model was then coupled to a secondary dynamics model consisting of two parts for conventional and articulated piston assemblies and described by Dursunkaya and Keribar [28]. In this study, wrist-pin hydrodynamic and boundary lubrication and its motion within its bearing were also analyzed. To reduce the CPU time, a technique equivalent to the inverse of the “mobility map” scheme (impedance maps), often utilized in bearing analysis, was used. Hydrodynamic and contact pressure calculations for the pin are first carried out in a pre-processing code, and then inserted into the secondary dynamics model. Later on, Dursunkaya et al. [29] used these coupled models and presented the results making comparisons between elastic and rigid skirts and between conventional and articulated pistons.

Wong et al. [30] investigated piston secondary motion and piston slap in partially-flooded elastohydrodynamic skirt lubrication. They employed the average Reynolds equation of Patir and Cheng [11] with the flow factors of Zhu et al. [13]. Partial lubrication was dealt by setting the hydrodynamic pressure to ambient pressure at the starvation points where the clearance increased beyond a reference value. For ring forces, a basic model was created and pre-processed. Negative clearance issue, which is caused by piston diameters larger than the bore diameter during normal operating conditions after the piston is fit cold into the cylinder, was prevented by setting a minimum clearance value at each grid point at the start of the iteration and continuing the iteration until non-negative clearance values are reached. Later, Mansouri and Wong [16] developed this model incorporating the effects of piston skirt surface waviness, roughness, axial skirt profile, bulk elastic deformations and thermal distortion, lubrication and friction, and improving the numerical procedure for better computational efficiency. Parameters such as piston skirt profile, piston to liner clearance, surface roughness, and oil availability are examined for design purposes.

A multi-body dynamics simulation program for reciprocating engine system with elastically deformable piston skirt was developed by Kimura et al. [31] in order to examine the secondary motion of piston. The program uses specialized equations of motion using only the rotational degree of freedom of each component taking the transient crank speed into account. Friction calculations were done simply using the Stribeck diagram.

Based on their previous studies, Etsion and Gommed [32] optimized the design of a non-cylindrical, gas-lubricated, ringless piston. In the solution for pressure distribution, they used the dimensionless form of Reynolds equation without flow factors. They considered piston stability and gas leakage for optimization and presented some profiles with improved characteristics. Prata et al. [33] also studied on ringless pistons for small reciprocating compressors. They developed a simple model for oil-lubricated pistons, using average Reynolds equation without considering surface roughness effects on lubricant flow. Piston and liner were taken as rigid and hydrodynamic lubrication was assumed. Using a transparent test setup, this assumption had been observed to be valid for almost entire engine cycle.

Yang et al. [5] constructed a detailed model for secondary motion of the piston taking hydrodynamic lubrication, asperity contact and surface roughness effects on lubricant flow into account. Elastic deformations are considered in asperity contact condition only. Broyden method was used in the numerical solution, which was found out to have more tendency to converge than any other previously-used methods did. They also ran tests to validate their model. Laser induced fluorescent method was adopted in the equipment which is shown in Figure 1.5.

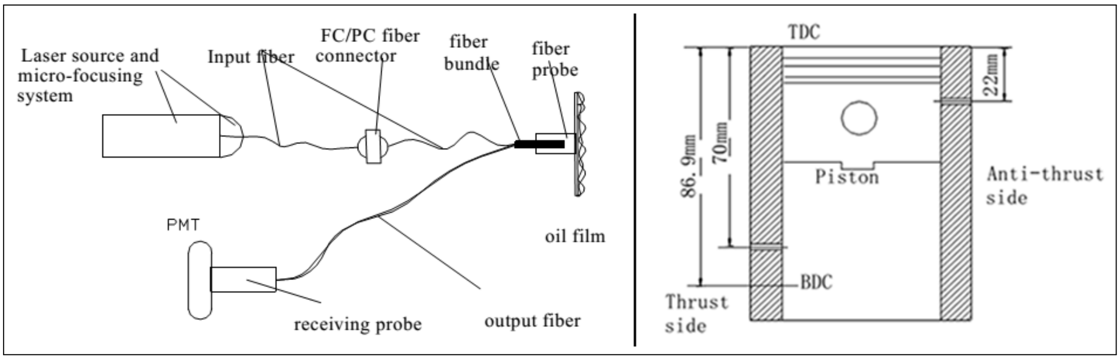

Figure 1.5 : Schematic drawing of oil film thickness measuring equipment and position of the fiber probe [5].

A simple algorithm was developed by Scholz and Bargende [34] for hydrodynamic contact lubrication. Roughness contact pressure was calculated and cavitation was included in the model. Secondary dynamics was not analyzed but this model is coupled to a FE model to solve for a piston-liner assembly. Results were compared to those of a previously-run test. However, they were not found in good agreement with each other.

Duyar et al. [19] improved the model of Dursunkaya et al. [29] by incorporating the partially-flooded lubrication case and cavitation analysis. To deal with the extent of lubrication, the mass conserving Reynolds equation solver of journal bearing analysis code, ORBIT, was adopted for skirt-liner lubrication. A variable called a nodal switch was used in the equations to distinguish between the flooded and cavitated nodes. Mass fluxes in the two-dimensional mass conserving Reynolds equation were expressed in terms of these nodal switches in the discretized form. In addition to allowing for the specification of an oil supply, the cavitation region is more accurately represented since the appropriate Reynolds boundary condition for oil film detachment and the Jakobsson-Floberg-Olsson (JFO) boundary condition for subsequent film re-attachment are applied.

1.3.2 Studies on piston ring lubrication

Beside skirt lubrication analysis, studies on piston ring-liner interaction have been carried out in order to determine lubrication characteristics and dynamic behavior of rings.

Chung et al. [35] analyzed fire ring wear. They solved Reynolds equation for uni-directional flow without roughness effects. They calculated hydrodynamic friction force from pressure distribution and read the boundary friction coefficient from the Stribeck diagram. For mixed lubrication case, they used both hydrodynamic and boundary friction coefficients with a factor representing the extent of metal-to-metal contact. Piston secondary motion and cavitation were not taken into account.

Jun et al. [36] used a contact factor and simplified the average Reynolds equation to save computational time. They assumed uni-directional lubricant flow and used Greenwood and Tripp's [25] asperity contact approach.

Yu et al. [8] gave an analytical solution of piston ring pack lubrication. They used full mass conservation boundary conditions theory defined by JFO to model cavitation. They also presented the details of open and enclosed cavitation patterns. JFO boundary condition was applied at the points of reformation of the oil film in enclosed cavitation.

Stanley et al. [37] constructed a simplified friction model for piston-ring assembly. They generated Stribeck curves using Reynolds equation for different ring profiles and used them in the calculation of the ring friction. They also modeled skirt friction with two-dimensional Reynolds equation. In ring friction, effects of surface characteristics, such as geometry and roughness, were included by means of a coefficient in the equation. In skirt lubrication part, surface roughness was neglected.

Zhang et al. [38] performed a two-dimensional piston ring lubrication analysis. They included flow factors of Patir and Cheng [1, 11], asperity contact model of Greenwood and Tripp [25], Roeland's equation for viscosity-temperature-pressure effects, lubricant temperature variation and cylinder liner deformations.

Akalin and Newaz [39] solved uni-directional Reynolds equation as in the model of Yun et al. [36] and included cavitation algorithm. They used Reynolds (Swift-Stieber) boundary conditions at film rupture locations. Surface roughness and asperity contact were considered. Contact load was calculated using Greenwood and Tripp's [25] model. In the second part of their study, Akalin and Newaz [40] correlated the results of their model with data from a bench test system developed by Akalin and Newaz [41].

Priest et al. [9] studied on cavitation in piston rings. They made a detailed review of different boundary conditions defined in the literature for film rupture and reformation. In their model, they applied these conditions and compared the results.

1.3.3 Experimental analysis of piston secondary dynamics

Test runs have been performed by several researchers to get experimental data and validate simulation results.

Teraguchi et al. [6] made experiments on the effects of oil supply on the cylinder block vibration, piston friction force, slap motion and oil consumption. Tests were run on a 1.7 liter, four-cylinder diesel engine varying the position of oil supply as shown in Figure 1.6.

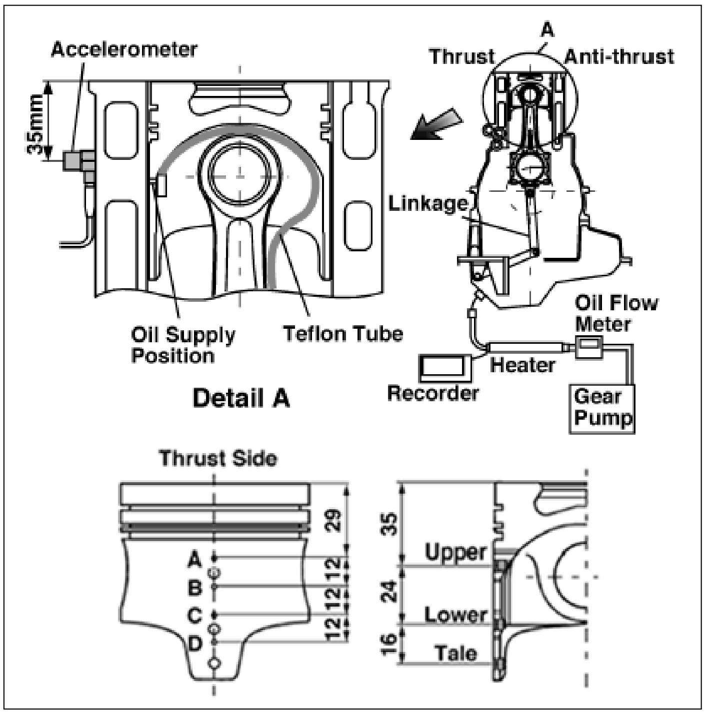

Figure 1.6 : Oil supply system and measuring points in the experiments held by Teraguchi et al. [6].

Friction losses for pistons with different surface roughness and finish methods were investigated by Sato et al. [7]. A single-cylinder diesel engine was adapted to the floating liner method as shown in Figure 1.7 and friction force was measured. Surface treatment methods such as plateau honing, etching and DLC coating were tested and comparisons were presented.

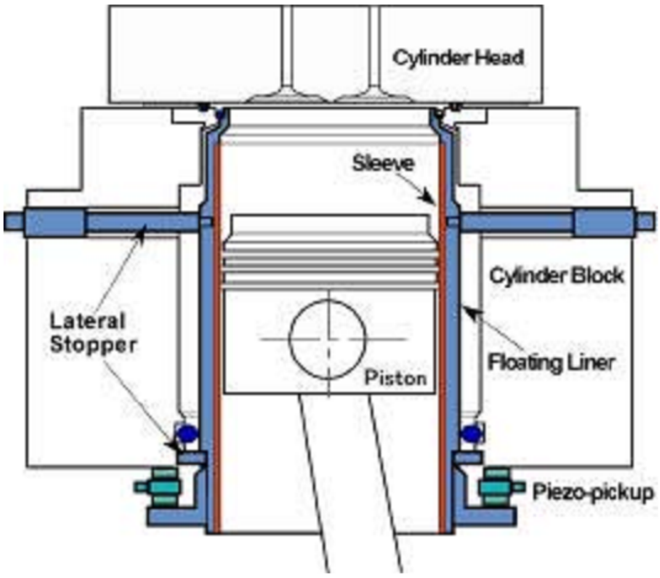

Figure 1.7 : Floating liner device modified into sleeve type [7].

Shin et al. [4] tried to validate previous numerical studies for the effect of offset crankshaft on friction performance of an internal combustion engine. A 4.2-liter I6 engine with an offset of 18 mm (Figure 1.4) was constructed and measurements were compared to those obtained from the baseline version of the same engine.

Dellis and Arcoumanis [42] ran experiments on a reciprocating test rig to visualize cavitation between a piston ring and liner throughout the stroke using a charge-coupled device (CCD) camera. Different cavitation patterns such as fern, fissure, string cavities and bubbles were observed and discussed.

2. THEORY

2.1 Lubrication Theory

2.1.1 Lubrication regimes

In the case of contact of two sliding rough surfaces, three different behaviors of the lubricant are observed. These are:

- Boundary lubrication
- Mixed lubrication
- Hydrodynamic lubrication
    - Elastohydrodynamic lubrication

In hydrodynamic lubrication regime, a full fluid film forms between two completely-separated surfaces. The most important property is dynamic viscosity of the lubricant. Elastohydrodynamic lubrication is similar to hydrodynamic lubrication in the context of surface separation, but as a result of relatively high normal load to be carried by the contact or relatively small clearance, the effect of elastic deformations is more significant. In addition, pressure dependence of viscosity becomes important in this regime due to high lubricant pressure. Likely, in the case of thermally transient applications, effects of thermal deformations and temperature dependence of viscosity should also be taken into consideration.

In boundary lubrication regime, surfaces slide quite like a dry contact. Since the surfaces are too close to each other, a full fluid film cannot form within the spaces between asperities. The effect of lubricant stays at the level of chemical actions of thin films of molecular proportions.

In mixed lubrication regime, there is asperity contact to some extent. Fluid film forms in available spaces but is continuously deformed by asperities passing through. Characteristics of both hydrodynamic and boundary lubrication are observed.

In the literature, starved, partial and fully-flooded lubrication terms are also used for boundary, mixed and hydrodynamic lubrication, respectively. Patir and Cheng [1, 11] defines $H_\sigma = 3$ as the point of transition from mixed to hydrodynamic regime and names the lubrication of contacts with $H_\sigma < 3$ as partial lubrication.

In Figure 2.1, effect of lubrication regimes on friction can be seen. The diagram was drawn in the light of Richard Stribeck's experiments on plain journal bearing friction, the results of which were subsequently reordered by Ludwig Gumbel. Stribeck diagram shows the variation of friction coefficient with Sommerfeld grouping, $(\eta N/P)$, where η is dynamic viscosity, N is the rotational speed for a journal bearing (or sliding velocity, in general) and P is specific pressure (or normal load, in general). To make the behavior of rough surfaces clear, film thickness ratio (H_σ), which is defined as the ratio of effective film thickness to surface roughness, can be used on the abscissa as well [2]. As the surfaces move away from each other, the number of asperity peaks high enough to interact with those of the other surface decreases and the regime tends to be more hydrodynamic.

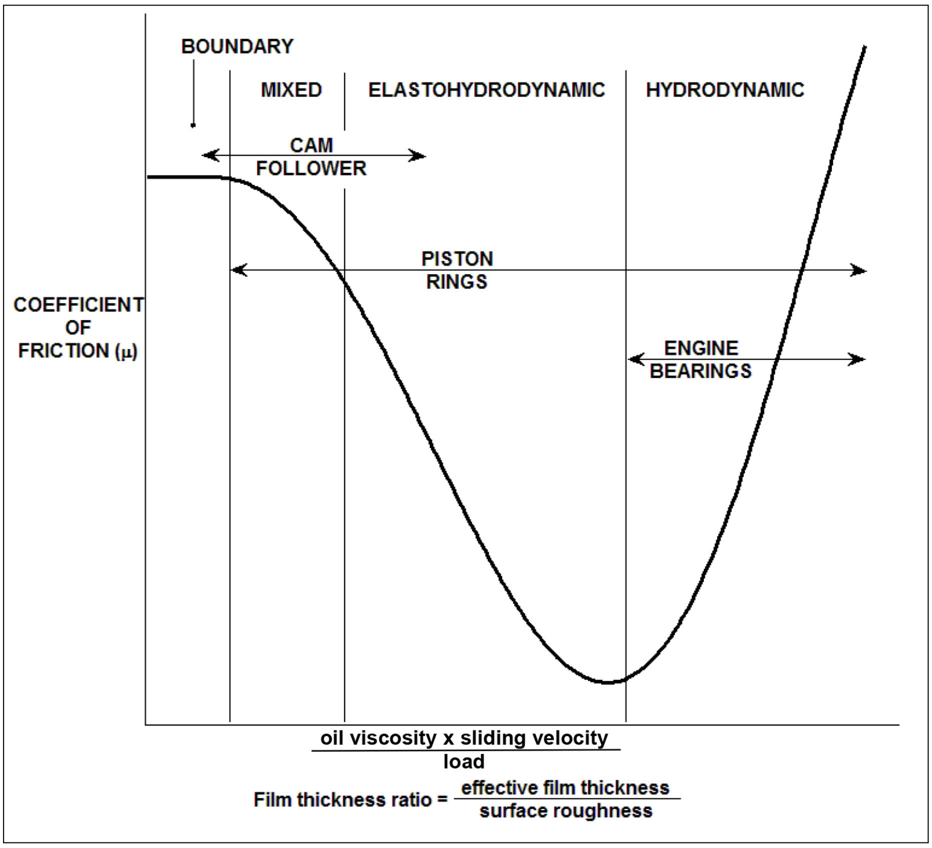

Figure 2.1 : Stribeck diagram.

Friction coefficient remains approximately constant in boundary lubrication regime. It is not affected by the change in lubricant viscosity, relative velocity or normal contact load. From the film thickness ratio point of view, up to a certain value of film thickness, friction coefficient does not vary. With a further increase in film thickness, fluid film starts to build up and become effective in load carrying. At the point of transition to mixed lubrication regime, friction coefficient starts decreasing, as expected. It decreases until the asperity contact gets insignificant or ceases completely, and the regime turns to hydrodynamic lubrication. Therefore, for a steady-state EHD contact application, operation in the transition region from mixed to hydrodynamic lubrication should be aimed in order to minimize friction loss. To prevent solid-to-solid contact and reduce wear, Sommerfeld group may be shifted slightly towards hydrodynamic region. In practice, at a steady-state application, after some time of operation in the transition region, high peaks will be worn first and hydrodynamic lubrication will be obtained.

However, in the case of ICE or compressor piston assembly lubrication, steady-state lubrication is impossible because of the variable forces acting on the piston during a complete power cycle, even at constant speed and load conditions. Figure 2.1 shows lubrication characteristics in an automobile engine piston assembly, together with other lubricated components. Piston ring and skirt lubrication falls in a wide range that spans mixed and hydrodynamic lubrication regions.

2.1.2 Inlet and outlet conditions of lubricant film

2.1.2.1 Effect of oil supply at the inlet

Amount of lubricant supplied to the EHD contact has great importance on the quality of lubrication. First of all, the sliding surface in the hydrodynamic contact requires enough amount of oil present at its leading edge in order to form a film layer. As this amount decreases, the lubrication regime shifts towards boundary lubrication.

The amount of oil supply can be represented with the thickness of oil on the cylinder liner at the leading edge side. As a result of the geometry of the convergent section of barrel profile, inlet location shifts towards the leading edge side and effective lubrication length increase as the supply oil film thickness increases. This can be seen in Figure 2.2. For an ICE piston skirt, this thickness is set by the operation of oil control ring while the piston is moving towards TDC, and by the amount left from the previous cycle of the piston and wetting mechanisms such as oil jet and splashing of crank while the piston is moving towards BDC. Therefore, design of the oil supply mechanisms is quite important.

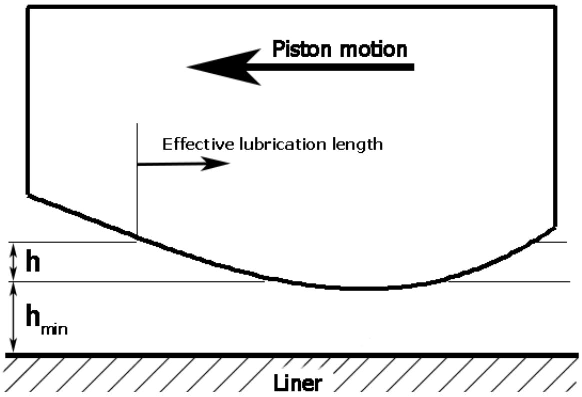

Figure 2.2 : Effect of supply oil thickness on effective lubricated length.

Depending on the amount of oil supplied to the skirt, inlet conditions can be named as:

- Fully-flooded inlet
- Partially-flooded inlet
- Starved inlet

and sufficiency can be decided comparing the existing oil thickness to the reference value predicted at design stage.

In most of the lubrication studies, fully-flooded inlet condition is assumed and a stationary inlet location is set. If the thickness of supply oil can be calculated, the exact inlet location can be found using the instantaneous orientation of the piston and geometric relations of barrel profile. Since the calculation of the supply oil thickness brings too much complexity to the problem, rough predictions may be more practical.

2.1.2.2 Outlet conditions and cavitation

Lubricant film loses its capacity to carry load at the outlet location and separates from the sliding surface. Having the outlet location close to the trailing edge increases the effective lubrication length and provides a smoother operation to the piston. In piston skirt lubrication, the approach is to determine piston skirt length according to the possible outermost inlet and outlet locations. If a section at the leading or trailing edge is not wetted at all under any operating conditions, either the barrel profile can be flattened to make use of the whole skirt length or unwetted section can be cut out to reduce piston mass.

In transient lubrication conditions, especially in the case of skirt lubrication, it is difficult to predict a fixed outlet location due to cavitation. Cavitation term is used for the rupture of fluid film at locations where pressure drops under a certain value. This value may be the saturation pressure of air which is close to ambient pressure or the trailing edge pressure. Under no-cavitation conditions, this drop to trailing edge pressure is expected to happen at the end of the effective lubrication length. Rupture before the outlet location takes place because of the incapability of the lubricant to have pressures below ambient or in other words to carry tensile load. Reason for pressure drop is the increase in local film thickness due to the divergent section of the barrel profile and/or negative squeeze film effect.

In the case of piston skirt and ring lubrication, locations at which the fluid film ruptures in no-cavitation and cavitation conditions are shown in Figure 2.3. x_i, x_o and x_p are inlet, outlet and rupture locations, respectively, and p_L and p_T are leading and trailing edge pressures, respectively. L_{lub} is the predicted effective lubrication length.

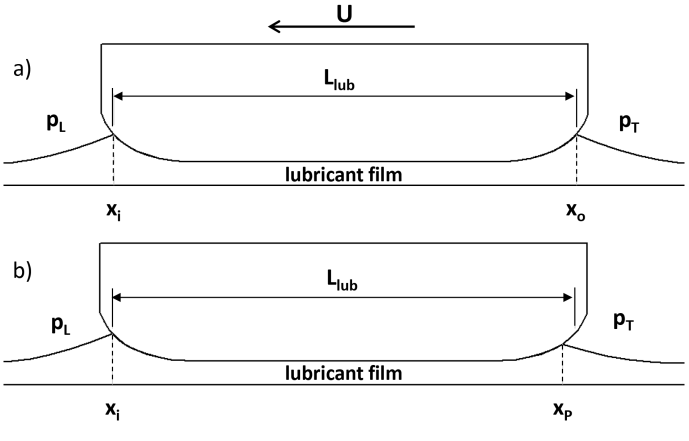

Figure 2.3 : Lubricated length on a piston skirt or ring surface in a) no-cavitation and b) cavitation conditions

Two types of cavitation, schematics of which are shown in Figure 2.4, have been defined by Ma et al. [43]:

- Enclosed cavitation
- Open cavitation

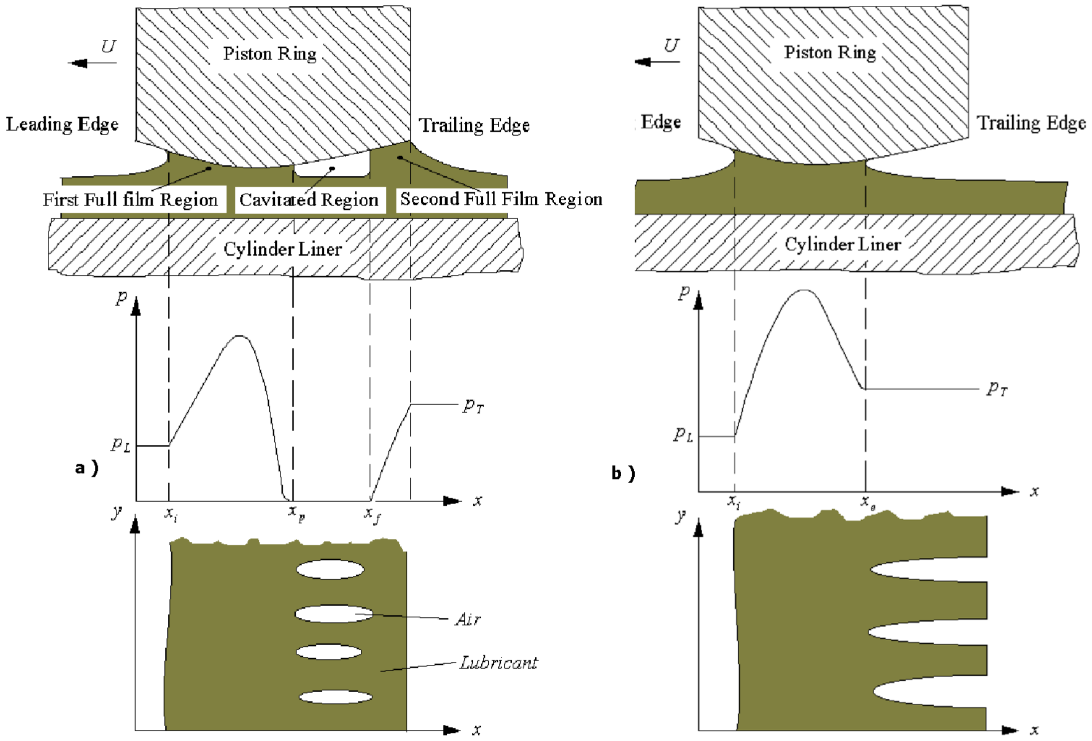

Figure 2.4 : a) Enclosed and b) open cavitation patterns [8]

In enclosed cavitation, fluid film ruptures at x_p, a point inside the divergent passage, and reforms at x_f since trailing edge pressure is higher than that in the cavitated region. Reason for cavitation is the drop in the local pressure to values below the saturation pressure of air which is dissolved in the oil. According to JFO theory, pressure inside the cavitated zones is constant and close to ambient pressure [43].

In open cavitation case, film rupture occurs at x_p and cannot reform at the downstream. In this case, the reason is oil starvation. Pressure at the cavitated zone is the trailing edge pressure. At the strips of lubricant between the cavitated zones, high pressure cannot develop. Although those areas are wetted with lubricant, oil film cannot provide additional support to piston skirt. This behavior of lubricant film is also called flow separation.

In Figures 2.5 and 2.6, pressure distributions along the lubricant film according to a number of different approaches are given [9]. In Figure 2.5, inlet, film rupture, film reformation and outlet locations are shown by x_1, x_2, x_3 and x_4, respectively.

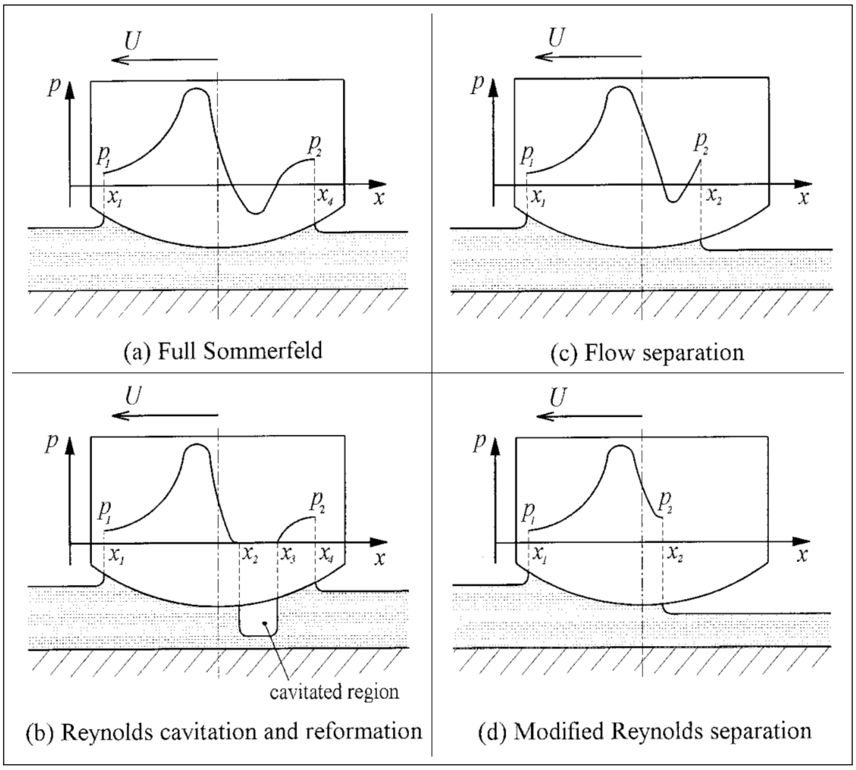

(a) Full Sommerfeld

(c) Flow separation

(b) Reynolds cavitation and reformation

(d) Modified Reynolds separation

Figure 2.5 : Pressure distribution along fluid film according to different boundary condition approaches [9]

The simplest approach was suggested by Sommerfeld in 1904 [9]. Outlet pressure was set to trailing edge pressure.

$$\begin{aligned} at \quad x = x_1, \quad p = p_L \\ at \quad x = x_4, \quad p = p_T \end{aligned} \tag{2.1}$$

These boundary conditions lead to large negative pressures in the divergent passage, Figure 2.5a. In 1921, Gümbel recognized the inability of oil film to carry tensile stress

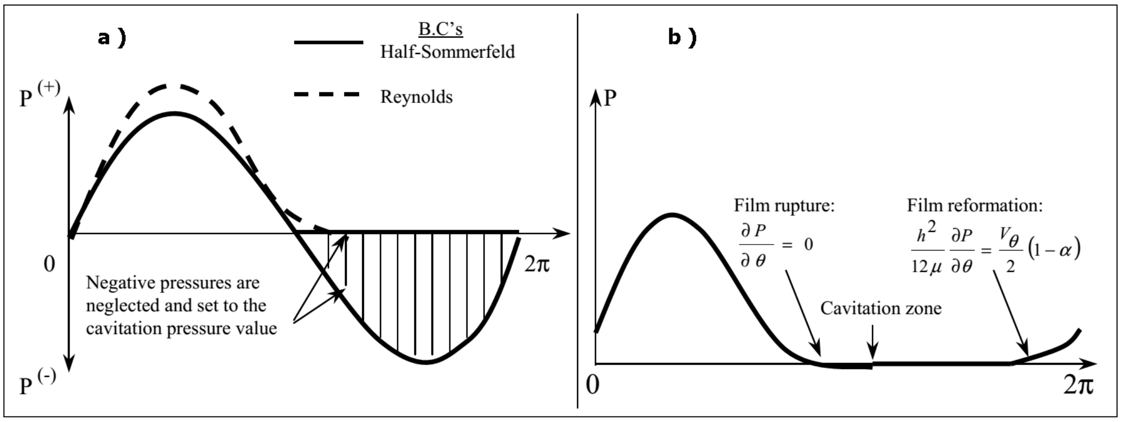

Figure 2.6 : Film pressure distributions according to different approaches: a) Half-Sommerfeld cavitation and Reynolds flow separation and b) Reynolds cavitation and JFO film reformation [10]

and simply set the negative pressures to ambient pressure or zero gauge, practically creating a cavitated region [9]. These conditions are referred to as Gümbel or Half-Sommerfeld boundary conditions (Figure 2.6a). However, this approach violates the mass continuity in the flow field [9].

Reynolds appreciated the role of cavitation in his classical work on lubrication theory [44], leading later to the formulation of the Reynolds cavitation condition independently by Swift [45] and Steiber [46].

$$\begin{aligned} &at \quad x = x_1, \quad p = p_L \\ &at \quad x = x_4, \quad p = p_T \, , \, \frac{\partial p}{\partial x} = 0 \end{aligned} \tag{2.2}$$

which is superior to Half-Sommerfeld boundary conditions since it correctly accounts for oil flow continuity across the cavitation boundary. Film reformation condition was then formulated by Dawson et al. again from the oil flow continuity [47].

$$at \quad x = x_3, \quad p = 0 \, , \, \frac{\partial p}{\partial x} = 6\mu U \frac{h_2 - h_3}{{h_3}^3} \tag{2.3}$$

An alternative approach belongs to Dawson and Taylor, proposing that flow separation occurs rather than cavitation [48]. The simplest flow separation model is referred to as full-fluid-film condition leading to the formulation derived from Navier-Stokes equations.

$$at \quad x = x_2, \quad p = 0 \, , \, \frac{\partial p}{\partial x} = \frac{2\mu U}{{h_2}^2} \tag{2.4}$$

However, the full-fluid-film condition is approximate since a full fluid film is assumed and no development of the lubricant-gas interface is considered. This assumption was dropped by introducing the following boundary conditions:

$$at \quad x = x_2, \quad p = 0 \, , \, \frac{\partial p}{\partial x} = \frac{6\mu U}{{h_2}^2} \left(1 - 2\frac{h_\infty}{h_2}\right) \tag{2.5}$$

where h_∞ is the asymptotic film thickness downstream of the separation point whose relationship with the film thickness at the point of separation, h_2, may be determined from tabulated data given by Coyne and Elrod [49,50].

In flow separation approach, the hydrodynamic pressure profile is characterized most significantly by a small sub-ambient pressure loop upstream of the point of separation as shown in Figure 2.5c.

Wakuri et al. [51] proposed that cavitation occurs in the lubricant with no reformation. The justification for this proposal was the equality of saturation pressure of the gas to trailing edge pressure. Richardson and Borman [52] and Taylor et al. [53] applied these boundary conditions but treated the rupture as flow separation rather than cavitation based on their experimental observations. This case (Figure 2.5c) is referred to as modified Reynolds separation with the boundary conditions being the same as Reynolds cavitation.

$$at \quad x = x_2, \quad p = p_T \; , \; \frac{\partial p}{\partial x} = 0 \tag{2.6}$$

The last approach that will be mentioned here is the JFO (Jakobsson-Floberg-Olsson) reformation conditions. After rupturing according to the Reynolds pressure gradient condition, lubricant film reforms such that:

$$at \quad x = x_3, \quad p = 0 \; , \; \frac{\partial p}{\partial x} = \frac{6\mu U}{{h_3}^2}(1-\alpha) \tag{2.7}$$

where α is the mass fraction variable details of which is given in [10].

2.2 Governing Equations

2.2.1 Equations of motion

Equations of motion were written for piston and connecting rod in order to solve the lateral motion of the piston. The coordinate system used and necessary geometrical parameters are shown in Figure 2.7. x-z coordinates are fixed to the cylinder block whereas x'-z' coordinates are moving with the piston. Direction of Earth's gravity is shown, as well, to be used in the case that the cylinder block has an inclined orientation.

Forces acting on the piston are gas force, pin force due to the reaction from connecting rod, normal force and friction on the piston skirt surface due to lubricant interaction and solid-to-solid contact. Moments on the piston are pin moment due to lubricant pressure and skirt friction. Making use of these forces and moments shown in Figure

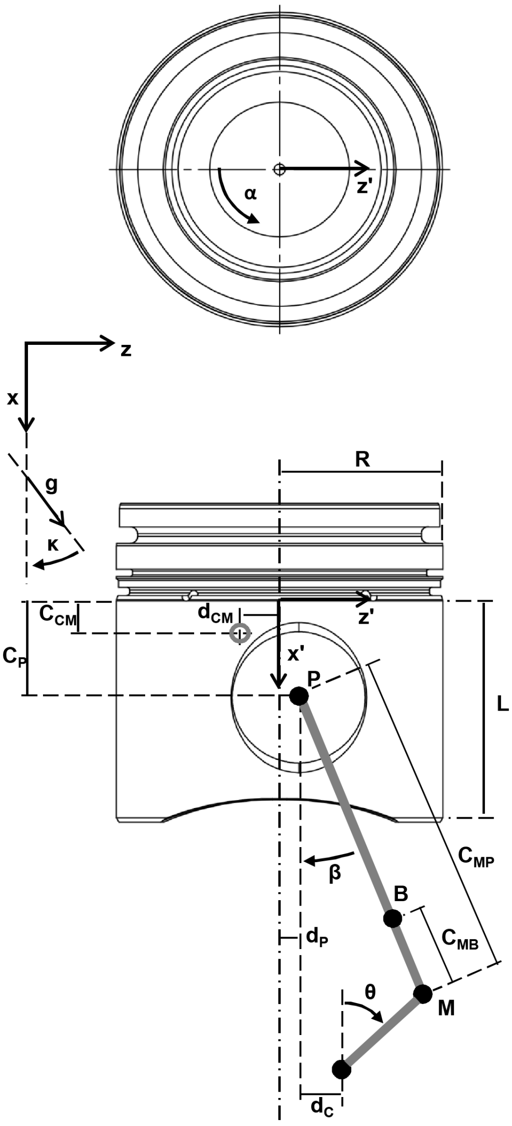

Figure 2.7 : Coordinate system and geometry of the piston assembly

2.8, equations of motion for piston are written as

$$F_h \cos\zeta - F_f \sin\zeta - F_g \sin\zeta + F_{rz} + mg\sin\kappa = mA_{Pz} \tag{2.8a}$$

$$-F_h \sin\zeta + F_f \cos\zeta + F_g \cos\zeta + F_{rx} + mg\cos\kappa = mA_{Px} \tag{2.8b}$$

$$M_{pin} + M_h + M_f + mg\sin\kappa(C_P - C_{CM}) - mg\cos\kappa(d_{CM} + d_P) = I_P\ddot{\zeta} \tag{2.8c}$$

Making use of $\sin\zeta = 0$ and $\cos\zeta = 1$ for small ζ, and neglecting M_{pin}, equation 2.8 reduces to

$$F_h + F_{rz} + mg\sin\kappa = mA_{Pz} \tag{2.9a}$$

$$F_f + F_g + F_{rx} + mg\cos\kappa = mA_{Px} \tag{2.9b}$$

$$M_h + M_f + mg\sin\kappa(C_P - C_{CM}) - mg\cos\kappa(d_{CM} + d_P) = I_P\ddot{\zeta} \tag{2.9c}$$

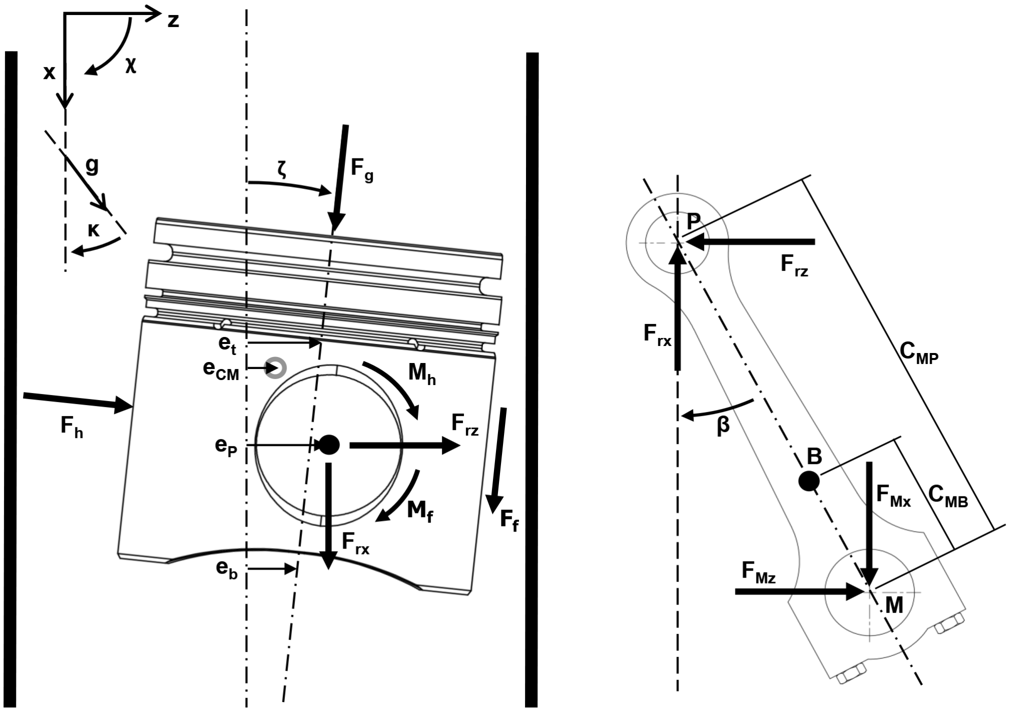

Figure 2.8 : Free-body diagram for piston and connecting rod

Equations of motion for the connecting rod are

$$F_{Mz} - F_{rz} = m_B A_{Bz} \tag{2.10a}$$

$$F_{Mx} - F_{rx} = m_B A_{Bx} \tag{2.10b}$$

$$\begin{aligned}&(F_{rx}(C_{MP} - C_{MB}) + F_{Mx} C_{MB}) \sin\beta \\ &\qquad -(F_{rz}(C_{MP} - C_{MB}) + F_{Mz} C_{MB}) \cos\beta = I_B \ddot{\beta}\end{aligned} \tag{2.10c}$$

Equations 2.9a and 2.9c are used to form the set of equations to be solved for piston motion, where F_{rz} can be rewritten as

$$\begin{aligned}F_{rz} =& \frac{C_{MB}}{C_{MP}} m_B [(A_{Bx} - g\cos\kappa)\tan\beta - (A_{Bz} - g\sin\kappa)] \\ &+ [m(A_{Px} - g\cos\kappa) - F_g - F_f]\tan\beta + \frac{I_B\ddot{\beta}}{C_{MP}\cos\beta}\end{aligned} \tag{2.11}$$

after arranging equations 2.9b and 2.10.

In order to solve the equations, forces and moments on the piston must be calculated. Gas force, F_g, can be calculated once the combustion chamber pressure is known, therefore it is a function of crank angle. Normal force acting on the piston skirt, F_h, results from lubricant film pressure and asperity contact pressure in case of solid-to-solid contact of skirt and bore surfaces. Tangential force, F_f, is a result of viscous interaction between skirt and lubricant as well as solid friction. These two forces and corresponding moments can be calculated after the lubrication analysis which depends on the relative motion of skirt and bore. Axial piston velocity is also a function of crank angle and can be obtained from kinematic relations. On the other hand, lateral motion of the piston is to be solved using the forces acting on it. This brings a coupled solution to the lateral motion, skirt lubrication and forces.

Lateral position of the piston can be represented by any two of the variables, e_t, e_b, e_{CM}, e_P and ζ which are the eccentricities of skirt top, skirt bottom, piston mass center and pin center, and angular displacement of piston from cylinder axis, respectively. These are shown in Figure 2.8. In this study, piston position with respect to cylinder axis is represented in terms of skirt top and bottom eccentricities. Therefore, mass center eccentricity and tilt angle is written as

$$e_{CM} = \left(1 - \frac{C_{CM}}{L}\right) e_t + \frac{C_{CM}}{L} e_b \tag{2.12a}$$

$$\zeta = \frac{e_t - e_b}{L} \tag{2.12b}$$

Furthermore, lateral and angular velocities are

$$\dot{e}_{CM} = \left(1 - \frac{C_{CM}}{L}\right) \dot{e}_t + \frac{C_{CM}}{L} \dot{e}_b \tag{2.13a}$$

$$\dot{\zeta} = \frac{\dot{e}_t - \dot{e}_b}{L} \tag{2.13b}$$

and lateral and angular accelerations are

$$\ddot{e}_{CM} = \left(1 - \frac{C_{CM}}{L}\right) \ddot{e}_t + \frac{C_{CM}}{L} \ddot{e}_b \tag{2.14a}$$

$$\ddot{\zeta} = \frac{\ddot{e}_t - \ddot{e}_b}{L} \tag{2.14b}$$

Letting $A_{Pz} = \ddot{e}_{CM}$ and substituting equations 2.14 into equations 2.9a and 2.9c, equations of motion can be written as functions of piston top and bottom accelerations

$$F_h + F_{rz} + mg \sin\kappa = m \left[\left(1 - \frac{C_{CM}}{L}\right) \ddot{e}_t + \frac{C_{CM}}{L} \ddot{e}_b \right] \tag{2.15a}$$

$$M_h + M_f + mg \sin\kappa (C_P - C_{CM}) - mg \cos\kappa (d_{CM} + d_P) = I_P \frac{\ddot{e}_t - \ddot{e}_b}{L} \tag{2.15b}$$

where the solution for piston lateral motion reduces to

$$\begin{bmatrix} m\left(1-\dfrac{C_{CM}}{L}\right) & m\dfrac{C_{CM}}{L} \\ \dfrac{I_P}{L} & -\dfrac{I_P}{L} \end{bmatrix} \begin{bmatrix} \ddot{e}_t \\ \ddot{e}_b \end{bmatrix} = \begin{bmatrix} F_h + F_{rz} + mg\sin\kappa \\ M_h + M_f + mg\left[\sin\kappa(C_P - C_{CM}) - \cos\kappa(d_{CM} + d_P)\right] \end{bmatrix} \tag{2.16}$$

2.2.2 Reynolds equation

For an isothermal, incompressible lubricant, the pressure in elastohydrodynamic contacts is governed by Reynolds equation

$$\frac{\partial}{\partial x}\left(\frac{{h_T}^3}{12\mu}\frac{\partial p}{\partial x}\right) + \frac{\partial}{\partial y}\left(\frac{{h_T}^3}{12\mu}\frac{\partial p}{\partial y}\right) = \frac{U_1+U_2}{2}\frac{\partial h_T}{\partial x} + \frac{\partial h_T}{\partial t} \tag{2.17}$$

with x being the sliding direction. U_1 and U_2 are absolute velocities of the sliding surfaces and h_T is local gap (or local film thickness).

In equation 2.17, the two terms on the LHS are the mass transport in x and y-directions, respectively, due to pressure gradient. The first term on the RHS is the mass transport due to change in the film thickness along the direction of the lubricant flow and the last term is the squeeze film velocity. Squeeze film effect is the change in film thickness due to the movement of the surfaces towards or away from each other.

Reynolds equation was modified by Patir and Cheng [11] in order to include surface roughness effects. Average Reynolds equation for a two-dimensional flow between two rough surfaces can be expressed as

$$\frac{\partial}{\partial x}\left(\phi_x\frac{h^3}{12\mu}\frac{\partial p}{\partial x}\right) + \frac{\partial}{\partial y}\left(\phi_y\frac{h^3}{12\mu}\frac{\partial p}{\partial y}\right) = \frac{U_1+U_2}{2}\frac{\partial h_T}{\partial x} + \frac{U_1-U_2}{2}\sigma\frac{\partial \phi_s}{\partial x} + \frac{\partial h_T}{\partial t} \tag{2.18}$$

In the modified form, two pressure flow factors, ϕ_x and ϕ_y, and a shear flow factor ϕ_s are incorporated into Reynolds equation. Pressure flow factors compare the average pressure-induced flow on a rough surface to that on a smooth one. Introduction of pressure flow factors to the equation makes it possible to switch from local gap, h_T, to the local distance between the mean line of the two surfaces, h. The relation between local and nominal film thicknesses is shown in Figure 2.9 and given as

$$h_T = h + \delta_1 + \delta_2 \tag{2.19}$$

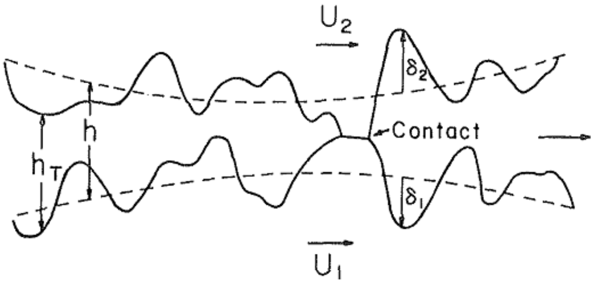

Figure 2.9 : Deviation from nominal film thickness with the effect of surface asperities [11]

.

Shear flow factor represents the additional flow due to sliding in a rough bearing. In the case of piston skirt-cylinder bore interaction, one of the surfaces, cylinder wall, is stationary which brings $U_1 = U$ and $U_2 = 0$. Hence, equation 2.18 takes the following form:

$$\frac{\partial}{\partial x}\left(\phi_x h^3 \frac{\partial p}{\partial x}\right) + \frac{\partial}{\partial y}\left(\phi_y h^3 \frac{\partial p}{\partial y}\right) = 6\mu U\left(\frac{\partial h_T}{\partial x} + \sigma\frac{\partial \phi_s}{\partial x}\right) + 12\mu\frac{\partial h_T}{\partial t} \tag{2.20}$$

2.2.3 Flow factors

A surface asperity profile may have a repeating deviation trend which can be expressed as waves. In addition, a wavy profile usually has random roughness over the wavy mean. The deviations from a smooth surface might then be decomposed into waviness and roughness as shown in Fig. 2.10. When the effect of the asperities to the lubricant flow is investigated, the surface needs to be well defined in terms of waviness and roughness components.

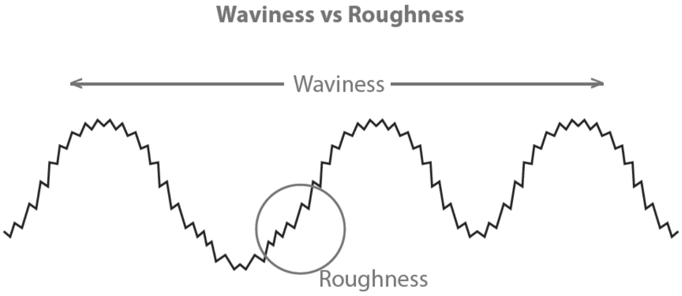

Figure 2.10 : Waviness and roughness components of a surface asperity profile [12]

.

2.2.3.1 Flow factors for a rough surface

Flow factors are strongly dependent on roughness and waviness of both surfaces and directional properties of the asperities. They were first defined as functions of H_σ

and γ, by Patir and Cheng [1] for a surface on which the asperities are represented as surface roughness only.

$$\phi_x = \phi_x(H_\sigma, \gamma) \tag{2.21a}$$

$$\phi_y = \phi_y(H_\sigma, \gamma) \tag{2.21b}$$

$$\phi_s = \phi_s(H_\sigma, \gamma) \tag{2.21c}$$

where $H_\sigma = \dfrac{h}{\sigma}$ and γ is a characteristic of a surface expressing the orientation of the asperities with respect to the flow direction.

Details of surface roughness orientation factor, γ, pressure flow factors, ϕ_x, ϕ_y, and shear flow factor, ϕ_s, are given in Appendix A.

2.2.3.2 Flow factors for a wavy surface

In case of a wavy profile, it was proposed that asperity effects to lubricant flow should be defined taking waviness dominance into account. A formulation was suggested by Zhu et. al ([13]), naming wave height with Ω, such that pressure flow factors are

$$\phi_x = \begin{cases} \left[1 - \left(\dfrac{\sigma}{h}\right)^2\right]^2 & ,\Omega = 0 \\ \left[1 - \left(\dfrac{\Omega}{h}\right)^2\right]^2 & ,\sigma = 0 \\ \dfrac{\left[(h+\Omega)^2 - \sigma^2\right]\left[(h-\Omega)^2 - \sigma^2\right]}{h^4} & \\ \times \left[1 - \dfrac{\sigma^2}{4\Omega}\left(\dfrac{h+\Omega}{(h+\Omega)^2 - \sigma^2} - \dfrac{h-\Omega}{(h-\Omega)^2 - \sigma^2}\right) - \dfrac{3\sigma^2}{8\Omega}L_n\right] & ,else \end{cases} \tag{2.22}$$

$$\phi_y = \begin{cases} \left[1 - \left(\dfrac{\Omega}{h}\right)^2\right]^2 & ,\sigma = 0 \\ \text{equation A.3} & ,\sigma \neq 0 \end{cases} \tag{2.23}$$

where

$$L_n = \frac{1}{\sigma} \ln \frac{(h - \Omega - \sigma)(h + \Omega + \sigma)}{(h - \Omega + \sigma)(h + \Omega - \sigma)} \tag{2.24}$$

In the same manner, shear flow factors are defined as

$$\phi_s = \begin{cases} \dfrac{\sigma}{h} & ,\Omega = 0 \\ \dfrac{\Omega}{h} & ,\sigma = 0 \\ \dfrac{\left[(h+\Omega)^2-\sigma^2\right]\left[(h-\Omega)^2-\sigma^2\right]}{8\Omega^3 h} & \\ \times L_n\left[2\Omega - \dfrac{\sigma^2}{2}\left(\dfrac{h+\Omega}{(h+\Omega)^2-\sigma^2} - \dfrac{h-\Omega}{(h-\Omega)^2-\sigma^2}\right) - \dfrac{3\sigma^2}{4}L_n\right] & ,else \\ +\dfrac{h}{\Omega} + \left(\dfrac{\sigma}{2\Omega}{}^{2}\right)\ln\dfrac{\left[(h+\Omega)^2-\sigma^2\right]}{\left[(h-\Omega)^2-\sigma^2\right]} & \end{cases} \tag{2.25}$$

2.2.3.3 Contact pressure and viscous shear stress for a rough surface

Solid-to-solid contact pressure can be calculated with the asperity contact model of Greenwood and Tripp [25] which was given as

$$p_c = KE'F_{2.5}(H_\sigma) \tag{2.26}$$

for which the details are given in Appendix A.

Viscous shear stress on the rough skirt surface is defined by Patir and Cheng [1] with the following formula:

$$\tau = \frac{\mu|U|}{h}\left[\left(\phi_f - \phi_{fs}\right) + 2V_{r1}\phi_{fs}\right] \tag{2.27}$$

Details of the shear stress factors, ϕ_{fs} and ϕ_f can be found in Appendix A.

2.2.3.4 Contact pressure and viscous shear stress for a wavy surface

In case of wavy skirt surface, shear stress acting on the skirt by lubricant interaction can be defined in terms of shear stress factors, ϕ_f, ϕ_{fs} and ϕ_{fp}. Viscous shear stress can be calculated by

$$\tau = \frac{\mu|U|}{h}\left[\left(\phi_f + \phi_{fs}\right) + \phi_{fp}\frac{h}{2}\frac{\partial p}{\partial x}\right] \tag{2.28}$$

where

$$\phi_f = \begin{cases} \dfrac{h}{2\sigma}\ln\left(\dfrac{h+\sigma}{h-\sigma}\right) & ,\Omega = 0 \\ \dfrac{h}{2\Omega}\ln\left(\dfrac{h+\Omega}{h-\Omega}\right) & ,\sigma = 0 \\ \dfrac{h}{4\Omega\sigma}\big[\quad (h+\Omega+\sigma)\ln(h+\Omega+\sigma) & \\ \qquad -(h-\Omega+\sigma)\ln(h-\Omega+\sigma) & ,else \\ \qquad -(h+\Omega-\sigma)\ln(h+\Omega-\sigma) & \\ \qquad +(h-\Omega-\sigma)\ln(h-\Omega-\sigma)\big] & \end{cases} \tag{2.29}$$

$$\phi_{fs} = \begin{cases} \dfrac{3}{2}\left[\dfrac{h}{\sigma}\ln\left(\dfrac{h+\sigma}{h-\sigma}\right) - 2\right] & ,\Omega = 0 \\ \dfrac{3}{2}\left[\dfrac{h}{\Omega}\ln\left(\dfrac{h+\Omega}{h-\Omega}\right) - 2\right] & ,\sigma = 0 \\ \dfrac{3h}{4\Omega}\left[\ln\dfrac{(h+\Omega)^2-\sigma^2}{(h-\Omega)^2-\sigma^2} - \dfrac{\left[(h+\Omega)^2-\sigma^2\right]\left[(h-\Omega)^2-\sigma^2\right]}{4\Omega h}\right. & ,else \\ \qquad \left.\times L_n\left(\dfrac{h+\Omega}{(h+\Omega)^2-\sigma^2} - \dfrac{h-\Omega}{(h-\Omega)^2-\sigma^2} + \dfrac{L_n}{2}\right)\right] & \end{cases} \tag{2.30}$$

$$\phi_{fp} = \begin{cases} 1-\left(\dfrac{\sigma}{h}\right)^2 & ,\Omega = 0 \\ 1-\left(\dfrac{\Omega}{h}\right)^2 & ,\sigma = 0 \\ \dfrac{\left[(h+\Omega)^2-\sigma^2\right]\left[(h-\Omega)^2-\sigma^2\right]}{4\Omega h^2} & ,else \\ \times\left(\dfrac{h-\Omega}{(h-\Omega)^2-\sigma^2} - \dfrac{h+\Omega}{(h+\Omega)^2-\sigma^2} - \dfrac{L_n}{2}\right) & \end{cases} \tag{2.31}$$

Asperity contact pressure for a wavy surface can be found with the investigation of a single wave indenting into a smooth surface, assuming roughness effect is negligible compared to the waviness. Deformation of a wave peak under the contact load and resulting geometry is shown in Figure 2.11. Zhu et al. [13] give the relation between indentation, δ, and contact load per unit length, P_w, as

$$\delta = \frac{P_w}{E'}\left[0.635\left(\ln\frac{1}{\tan\tilde{\alpha}} - \ln\frac{P_w}{E'}\right) + 1.0556\right] \tag{2.32}$$

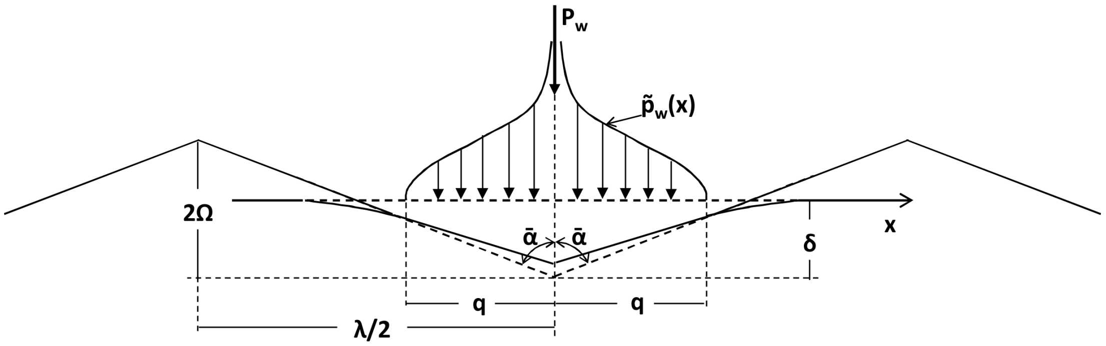

Figure 2.11 : Single wave deforming under contact load [13].

Knowing that $\tan\tilde{\alpha} = \dfrac{\lambda}{4\Omega}$ and mean wavy contact pressure is $p_c = \dfrac{P_w}{\lambda}$, equation 2.32 can be rewritten for the relation between indentation and contact pressure as

$$\delta = \frac{\lambda p_c}{E'}\left[0.635\left(\ln\frac{4\Omega}{\lambda} - \ln\frac{\lambda p_c}{E'}\right) + 1.0556\right] \tag{2.33}$$

3. SOLUTION APPROACH

Secondary motion of a reciprocating piston can be solved once the forces acting on it are known throughout the whole power cycle. Axial parameters as well as the gas force due to in-cylinder pressure are functions of only the crankangle and can be calculated for a specific engine operating condition. However, forces due to the viscous and solid interaction with the cylinder bore depend on the lateral position and its change in time. In addition, piston skirt deforms under thermal and mechanical loads. Thermal deformation can also be determined for constant engine load and speed. However, elastic deformation results from the normal forces acting on the skirt. Therefore, lateral piston motion, skirt lubrication and elastic deformation require an implicit, coupled solution. This section presents models of these subsystems. Later, the models are brought together and a MATLAB code is generated to obtain the solution.

3.1 Assumptions and Simplifications

3.1.1 Skirt deformations

Piston skirt undergoes thermal and elastic deformations. Thermal deformation occurs as a result of heating of the engine. In this study, the solution for piston lateral motion is investigated under constant operating conditions. Therefore, temperature distribution of the engine assembly in a steady thermal state is predicted and final size and shape of the piston skirt is obtained for this temperature change from the initial ambient conditions.

Elastic deformations result from the forces and film pressure acting on the piston. Skirt shape alters during a power cycle. Prediction of this alteration is important, since barrel and oval profile of the piston skirt has significant influence on lubrication which in turn determines friction losses and wear. Therefore, variation of elastic skirt deformation is calculated throughout the whole cycle.

3.1.2 Oil supply

Amount of oil available at the leading edge of lubricant film is an important factor determining the size of the lubricated surface, film pressure and lubrication regime. Oil is carried to the cylinder wall and rings by oil jets and by the crank splashing the oil inside the crankcase. A good prediction considering the quality of these mechanisms is essential for the lubrication regimes.

In this study, partially-flooded inlet condition is applied assuming there is always a fluid film in front of the piston with a constant thickness of h_{max}. Piston surface touches the lubricant at the locations where the local gap is equal to h_{max} and pressure develops in the fluid film. Therefore, inlet location is set by h_{max} value and it varies during the cycle depending on the instantaneous piston orientation. The value of oil supply thickness can be changed to obtain starved or fully-flooded inlets which result in a shift towards boundary and hydrodynamic lubrication regimes, respectively.

3.1.3 Fluid and flow properties

Lubricant is assumed to be an incompressible, Newtonian fluid. Viscosity of the lubricant is taken as independent of pressure and a function of only temperature. Since engine runs at steady conditions, oil temperature is assumed constant and a single viscosity value is used for a specific operating condition.

Dynamic viscosity is calculated using Vogel's equation which defines the temperature dependence of viscosity and is given as

$$\mu = ae^{\frac{b}{T+c}} \tag{3.1}$$

The flow is laminar.

3.1.4 Surface properties

Surface of piston skirt is modeled by a wavy profile whereas cylinder bore surface has only roughness, with asperities approximated by a Gaussian distribution. Macroscale textures generated by coating, honing or laser applications are not taken into account in this study.

3.1.5 Structural and geometrical simplifications

In this model, only skirt lubrication, and forces and moments acting on the piston through skirt section are taken into account. The contribution of rings to piston friction is neglected. The effect of oil ring on skirt lubrication by determining oil supply during piston's movement towards TDC is taken into account by predicting an appropriate thickness value.

Piston skirt deviates slightly form a perfect cylindrical shape. This deviation which is the cause of film formation is modeled as an oval and barrel form for the piston skirt. Other irregularities are neglected and skirt is symmetrical around the piston axis. However, the model is still capable of dealing with any skirt profile.

3.2 Solution of Reynolds Equation for Lubricant Film Pressure Distribution

Lubricant film pressure can be solved using average Reynolds equation (equation 2.18) for rough surfaces. In the case of skirt lubrication, cylinder bore is stationary, therefore for only one moving surface, equation 2.20 is solved making use of a finite differencing scheme. The equation is first normalized using the following non-dimensional parameters:

$$X = \frac{2x}{L} \tag{3.2a}$$

$$Y = \frac{2y}{L} \tag{3.2b}$$

$$H = \frac{h}{c} \tag{3.2c}$$

$$T = t\omega \tag{3.2d}$$

$$U^* = \frac{U}{r\omega} \tag{3.2e}$$

$$P = \bar{p}\frac{c^2}{3\mu r\omega L} \tag{3.2f}$$

$$\sigma^* = \frac{\sigma}{c} \tag{3.2g}$$

$$\phi_c = \frac{\partial \bar{h}_T}{\partial h} \tag{3.2h}$$

where ϕ_c is the contact factor defined by Wu and Zheng [54] in order to approximate the average gap between the surfaces. ϕ_c is given as

$$\phi_c = \frac{1}{2}\left[1 + erf\left(H_\sigma\right)\right] \tag{3.3}$$

where erf is the error function.

Substituting the expressions in equations 3.2, non-dimensional form of average Reynolds equation for two rough surfaces one of which is stationary is obtained as

$$\frac{\partial}{\partial X}\left(\phi_x H^3\frac{\partial P}{\partial X}\right)+\frac{\partial}{\partial Y}\left(\phi_y H^3\frac{\partial P}{\partial Y}\right)=U^*\left(\phi_c\frac{\partial H}{\partial X}+\sigma^*\frac{\partial \phi_s}{\partial X}\right)+\beta^*\phi_c\frac{\partial H}{\partial T} \tag{3.4}$$

where $\beta^* = L/r$ is the squeeze film factor.

ϕ_x, ϕ_y, ϕ_s, H and P are all implicit functions of X and Y. Therefore, they will be differentiated numerically. Substituting the following parameters:

$$C = \phi_x H^3 \tag{3.5a}$$

$$D = \phi_y H^3 \tag{3.5b}$$

and writing equation 3.4 again

$$\frac{\partial C}{\partial X}\frac{\partial P}{\partial X}+C\frac{\partial^2 P}{\partial X^2}+\frac{\partial D}{\partial Y}\frac{\partial P}{\partial Y}+D\frac{\partial^2 P}{\partial Y^2}=U^*\left(\phi_c\frac{\partial H}{\partial X}+\sigma^*\frac{\partial \phi_s}{\partial X}\right)+\beta^*\phi_c\frac{\partial H}{\partial T} \tag{3.6}$$

is obtained. Naming derivatives of C and D as

$$DC = \frac{\partial C}{\partial X} \tag{3.7a}$$

$$DD = \frac{\partial D}{\partial Y} \tag{3.7b}$$

and writing the derivatives explicitly gives the following:

$$DC = H^3\frac{\partial \phi_x}{\partial X}+3H^2\phi_x\frac{\partial H}{\partial X} \tag{3.8a}$$

$$DD = H^3\frac{\partial \phi_y}{\partial Y}+3H^2\phi_y\frac{\partial H}{\partial Y} \tag{3.8b}$$

Finally, non-dimensional average Reynolds equation can be expressed in the most explicit form as

$$DC\frac{\partial P}{\partial X}+C\frac{\partial^2 P}{\partial X^2}+DD\frac{\partial P}{\partial Y}+D\frac{\partial^2 P}{\partial Y^2}=U^*\left(\phi_c\frac{\partial H}{\partial X}+\sigma^*\frac{\partial \phi_s}{\partial X}\right)+\beta^*\phi_c\frac{\partial H}{\partial T} \tag{3.9}$$

At this stage, finite differencing approximations are introduced to equation 3.6. For any given property, Ψ, first and second derivatives in X and Y-directions can be written as given in equations 3.10 and 3.11, using the notations shown in Figure 3.1 where N, S, W and E stand for north, south, west and east neighboring nodes of node P, respectively.

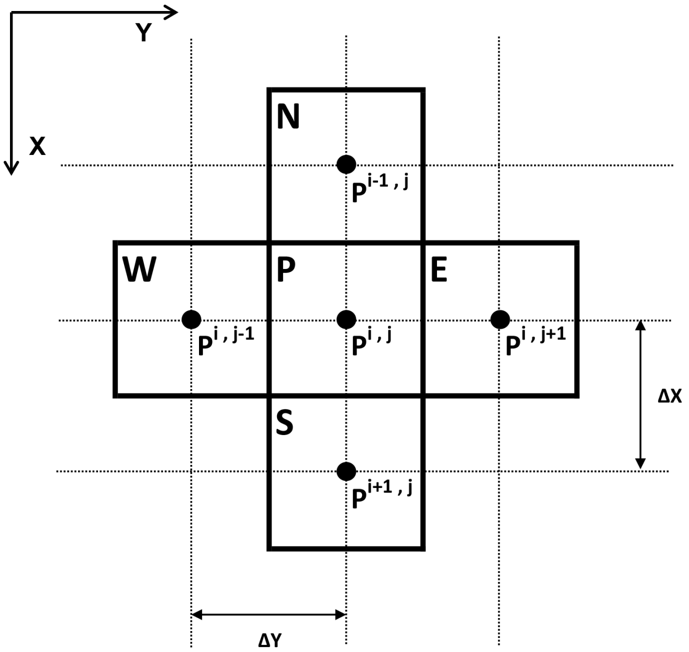

Figure 3.1 : Notation for the nodes

$$\frac{\partial \Psi}{\partial X} = \frac{\Psi^{i+1,j} - \Psi^{i-1,j}}{2\Delta X} \tag{3.10a}$$

$$\frac{\partial \Psi}{\partial Y} = \frac{\Psi^{i,j+1} - \Psi^{i,j-1}}{2\Delta Y} \tag{3.10b}$$

$$\frac{\partial^2 \Psi}{\partial X^2} = \frac{\Psi^{i+1,j} - 2\Psi^{i,j} + \Psi^{i-1,j}}{(\Delta X)^2} \tag{3.11a}$$

$$\frac{\partial^2 \Psi}{\partial Y^2} = \frac{\Psi^{i,j+1} - 2\Psi^{i,j} + \Psi^{i,j-1}}{(\Delta Y)^2} \tag{3.11b}$$

Applying the differencing scheme to the derivatives in equations 3.8 and 3.9,

$$\begin{aligned} DC\frac{P^{i+1,j} - P^{i-1,j}}{2\Delta X} &+ C\frac{P^{i+1,j} - 2P^{i,j} + P^{i-1,j}}{(\Delta X)^2} \\ &+ DD\frac{P^{i,j+1} - P^{i,j-1}}{2\Delta Y} + D\frac{P^{i,j+1} - 2P^{i,j} + P^{i,j-1}}{(\Delta Y)^2} \\ &= U^*\phi_c\frac{H^{i+1,j} - H^{i-1,j}}{2\Delta X} + U^*\sigma^*\frac{\phi_s^{i+1,j} - \phi_s^{i-1,j}}{2\Delta X} + \beta^*\phi_c\frac{\partial H}{\partial T} \end{aligned} \tag{3.12}$$

is obtained where

$$DC = \left(H^{i,j}\right)^3\frac{\phi_x^{i+1,j} - \phi_x^{i-1,j}}{2\Delta X} + 3\left(H^{i,j}\right)^2\phi_x^{i,j}\frac{H^{i+1,j} - H^{i-1,j}}{2\Delta X} \tag{3.13a}$$

$$DD = \left(H^{i,j}\right)^3\frac{\phi_y^{i,j+1} - \phi_y^{i,j-1}}{2\Delta Y} + 3\left(H^{i,j}\right)^2\phi_y^{i,j}\frac{H^{i,j+1} - H^{i,j-1}}{2\Delta Y} \tag{3.13b}$$

The last term in equation 3.12 is the non-dimensional squeeze film velocity. It can be evaluated using the local thickness values from previous time steps with the expression

$$\frac{\partial H}{\partial T}^{(t)} = \frac{H^{i,j^{(t)}} - H^{i,j^{(t-\Delta t)}}}{\Delta T} \tag{3.14}$$

In equations 3.12 and 3.13, ΔX and ΔY depend on mesh size, whereas U^*, σ^* and β^* are functions of geometrical variables, crankangle position and engine speed. They can be calculated from inputs. H, ϕ_c, squeeze film velocity and flow factors can all be calculated once the orientation of the piston is known or predicted. Therefore, equation 3.12 can be solved for the pressure distribution employing an iterative technique. For the simplicity of the remaining calculations, it can be arranged to form the general equation

$$AN^{i,j}P^{i-1,j} + AS^{i,j}P^{i+1,j}AW^{i,j}P^{i,j-1} + AE^{i,j}P^{i,j+1} + AP^{i,j}P^{i,j} = S^{i,j} \tag{3.15}$$

where

$$AN^{i,j} = -\frac{H^{i,j}}{4\left(\Delta X\right)^2}\left[\left(H^{i,j}\right)^2\left(\phi_x^{i+1,j} - 4\phi_x^{i,j} - \phi_x^{i-1,j}\right) + 3\phi_x^{i,j}\left(H^{i+1,j} - H^{i-1,j}\right)\right] \tag{3.16a}$$

$$AS^{i,j} = \frac{H^{i,j}}{4\left(\Delta X\right)^2}\left[\left(H^{i,j}\right)^2\left(\phi_x^{i+1,j} + 4\phi_x^{i,j} - \phi_x^{i-1,j}\right) + 3\phi_x^{i,j}\left(H^{i+1,j} - H^{i-1,j}\right)\right] \tag{3.16b}$$

$$AW^{i,j} = -\frac{H^{i,j}}{4\left(\Delta Y\right)^2}\left[\left(H^{i,j}\right)^2\left(\phi_y^{i,j+1} - 4\phi_y^{i,j} - \phi_y^{i,j-1}\right) + 3\phi_y^{i,j}\left(H^{i,j+1} - H^{i,j-1}\right)\right] \tag{3.16c}$$

$$AE^{i,j} = \frac{H^{i,j}}{4\left(\Delta Y\right)^2}\left[\left(H^{i,j}\right)^2\left(\phi_y^{i,j+1} + 4\phi_y^{i,j} - \phi_y^{i,j-1}\right) + 3\phi_y^{i,j}\left(H^{i,j+1} - H^{i,j-1}\right)\right] \tag{3.16d}$$

$$AP^{i,j} = -2\left(H^{i,j}\right)^3\left(\frac{\phi_x^{i,j}}{\left(\Delta X\right)^2} + \frac{\phi_y^{i,j}}{\left(\Delta Y\right)^2}\right) \tag{3.16e}$$

$$\begin{aligned} S^{i,j} = &\frac{U^*}{\Delta X}\left[\phi_c^{i,j}\left(H^{i+1,j} - H^{i-1,j}\right) + \sigma^*\left(\phi_c^{i+1,j} - \phi_c^{i-1,j}\right)\right] \\ &+ \beta^*\phi_c^{i,j}\frac{H^{i,j^{(t)}} - H^{i,j^{(t-\Delta t)}}}{\Delta T} \end{aligned} \tag{3.16f}$$

In order to solve the discretized general equation (equation 3.12), an (mxn) mesh is generated over the skirt surface. Assuming there is no motion of the piston along the wrist-pin axis, a symmetry plane, which is perpendicular to wrist-pin axis and coincident with the piston axis, can be defined.

Lubricated surface of a conventional ICE piston skirt is not a full cylinder. A meshed skirt is shown in Figure 3.2, with the angle of lubricated region being denoted by α_{lub}. In the figure, one side of a half piston model is given making use of symmetry. Lubricated region is meshed uniformly in order to match the nodes in the pressure solution domain, whereas a non-uniform mesh is generated for the rest of the body to be used in thermal and elastic deformation analysis. Results of deformation for the nodes inside the lubricated region are suitable to be used in pressure solution without the need for transformation which reduces numerical load on the code and avoids errors. The mesh has to be adjusted according to skirt mesh size and angle of lubrication, in case of a change of piston to be analyzed. This is a part of the pre-processing stage of the analysis together with the calculation of thermal deformations and stiffness matrix generation.

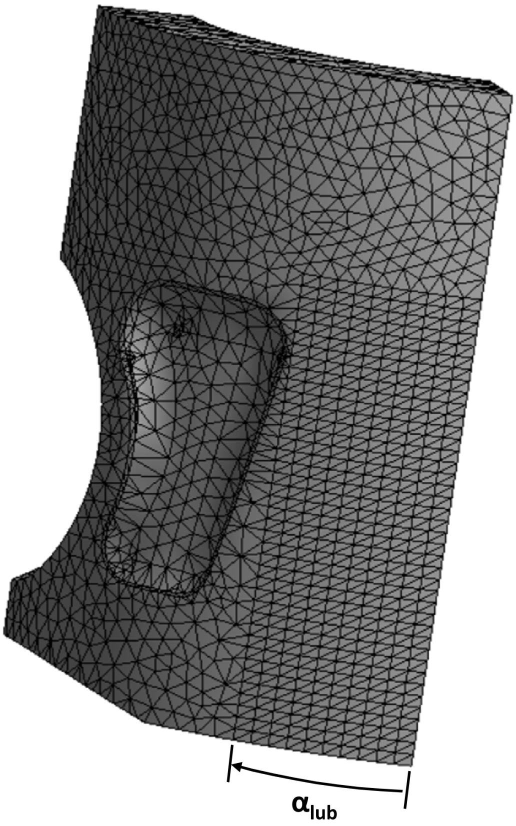

Figure 3.2 : Lubricated surface and mesh for a conventional ICE piston skirt (one side is shown).

Reynolds equation has been written in planar coordinates. Therefore the cylindrical surface of piston skirt is transformed to a planar surface with the following relations:

$$x = x' \tag{3.17a}$$

$$y = R\alpha \tag{3.17b}$$

A general mesh for Reynolds equation solution over a fully-lubricated cylindrical surface is given in Figure 3.3. In the figure, half of the cylinder is shown making use of the symmetry. This general mesh can be used when lubricant film pressure is expected to develop all around the piston. In the case of a modern ICE piston, bounding the mesh only to the lubricated region which is defined by α_{lub} saves significant computational time. Therefore, the mesh can be adopted by simply defining the nodes outside the lubricated region, setting the pressures at these nodes to crankcase pressure and carrying out the iterations only at the nodes within the lubricated region. Such a modified mesh example is shown in Figure 3.4. Nodal coordinates for an (mxn) mesh are denoted with i and j such that:

$$i = 1,2,3,...,m-1,m \tag{3.18a}$$

$$j = 1,2,3,...,n-1,n \tag{3.18b}$$

Pressure values at $x = 0$ and $x = L$ are set to pressure values p_1 and p_2, respectively, for a general solution. At the nodes on the symmetry lines, there is no flow in y-direction, leading to zero pressure gradient. Thus, west and east neighboring nodes have equal pressure values. For an (mxn) domain in the solution of a cylindrical piston, these conditions can be written in non-dimensional form as follows:

$$at \quad X = 0, \qquad P^{1,j} = P_1 \tag{3.19a}$$

$$at \quad X = 2, \qquad P^{m,j} = P_2 \tag{3.19b}$$

$$at \quad Y = 0, \qquad \frac{\partial P}{\partial Y} = 0, \quad thus \quad P^{i,2n-2} = P^{i,2} \tag{3.19c}$$

$$at \quad Y = 2\pi\frac{R}{L}, \qquad \frac{\partial P}{\partial Y} = 0, \quad thus \quad P^{i,n+1} = P^{i,n-1} \tag{3.19d}$$

In the case of conventional ICE piston, the domain is restricted by angle of lubrication, α_{lub}, on both left and right hand side of the mesh. Therefore, in addition to equation 3.19, the following boundary conditions can be applied:

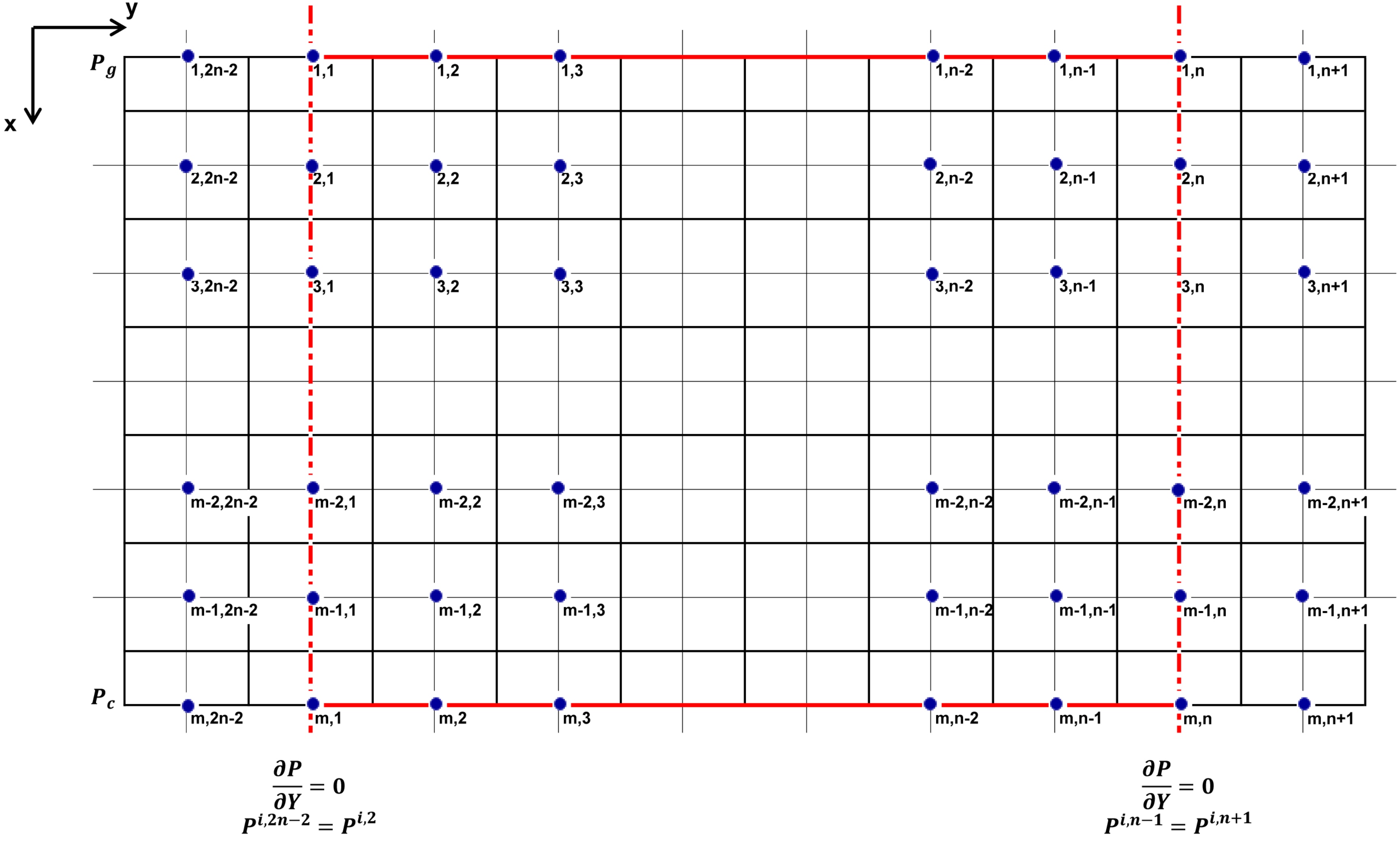

Figure 3.3 : General mesh for half of a fully-lubricated cylindrical surface.

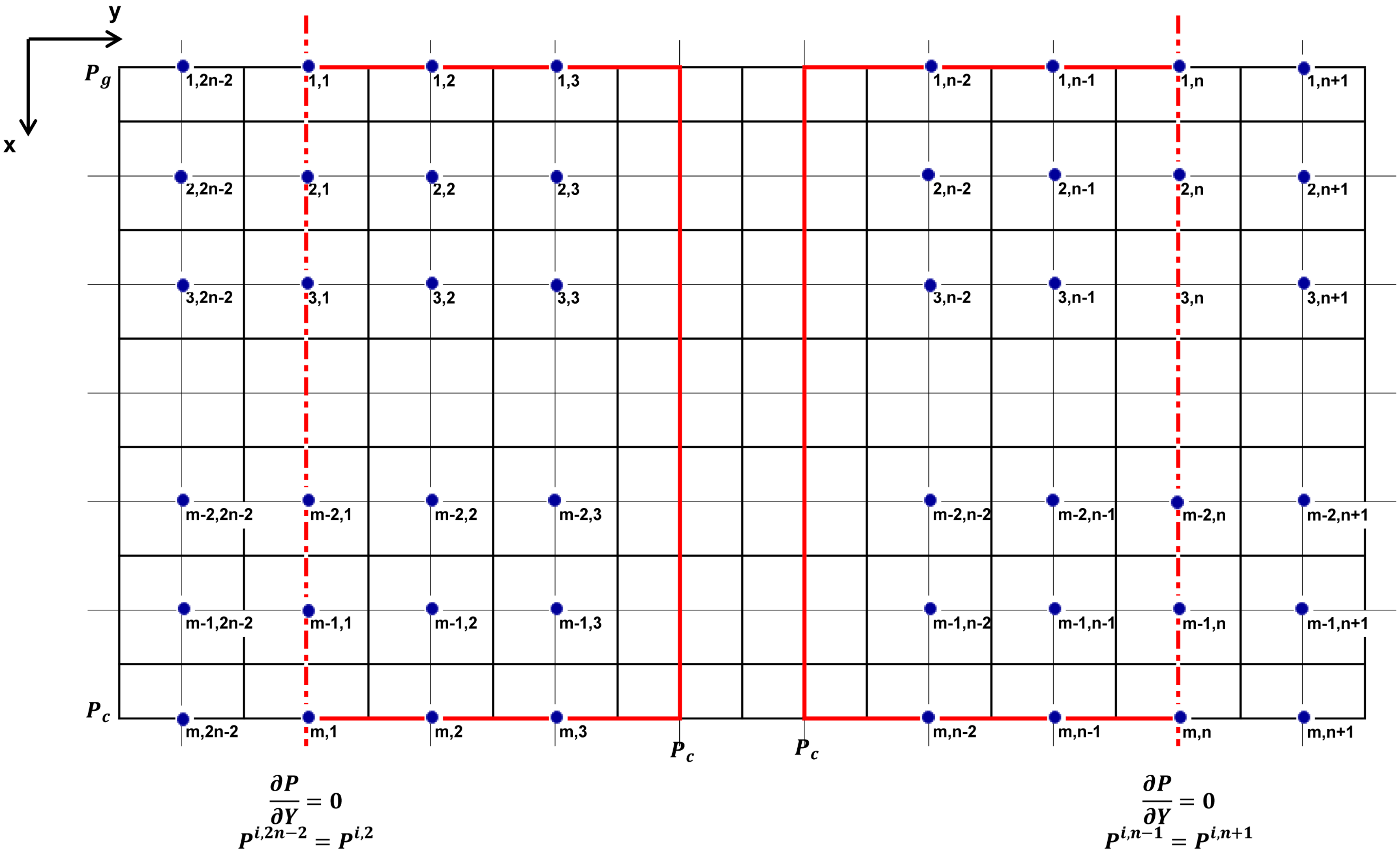

Figure 3.4 : Modified mesh for a conventional ICE piston skirt surface.

$$at \quad Y = 2\alpha_{lub}\frac{R}{L}, \qquad P^{i,n_{lub}} = P_1 = P_2 \tag{3.20a}$$

$$at \quad Y = 2\left(\pi - \alpha_{lub}\right)\frac{R}{L}, \qquad P^{i,n-n_{lub}+1} = P_1 = P_2 \tag{3.20b}$$

where n_{lub} denotes the nodes corresponding to α_{lub}. At all the inner nodes, pressure is forced to have a constant value. $P_1 = P_2$ is given for ICE piston skirt, because pressure at the ring side of skirt is equal to crankcase pressure, P_c. Pressure for inner nodes can be shown as:

$$at \quad 2\alpha_{lub} < Y < 2\left(\pi - \alpha_{lub}\right)\frac{R}{L}, \quad P^{i,n_{unlub}} = P_1 = P_2 = P_c \tag{3.21}$$

where

$$n_{unlub} = n_{lub}+1, n_{lub}+2, ..., n-n_{lub}-1, n-n_{lub} \tag{3.22}$$

Pressure distribution is calculated using Gauss-Seidel iteration. Initially, pressures at all the nodes are set to crankcase pressure. If the skirt is a fully-lubricated cylinder, initial condition can be defined as a linear distribution along X-direction, between $P_{1,j} = P_1$ and $P_{m,j} = P_2$. After new values are found, error is calculated with respect to the previous values at each node. Iterations are carried until local convergence at each node is satisfied. A pseudo-code is given in Figure 3.5.

```
sor = 1;                                                    % relaxation factor
dummy = 1;
while dummy>0
    dummy = 0;
    for j = 1:n
        for i = 2:m-1
            pnew(i,j) = (S(i,j)-AN(i,j)*pold(i-1,j)-AS(i,j)*pold(i+1,j)...
                                  -AW(i,j)*pold(i,j-1)-AE(i,j)*pold(i,j+1))/AP(i,j);
            pnew(i,j) = sor*pnew(i,j)+(1-sor)*pold(i,j);          % relaxation step
            if abs((pnew(i,j)-pold(i,j))/pnew(i,j)) > err          % error check
                dummy = 1;
            end
            pold(i,j) = pnew(i,j);
        end
    end
end
```

Figure 3.5 : Pseudo-code for pressure iteration.

3.3 Calculation of Local Film Thickness

Local film thickness over the skirt surface is mainly a function of piston lateral position and tilt. It can be defined in terms of piston top and bottom eccentricities for a perfectly cylindrical skirt. However, a conventional ICE piston skirt deviates from perfect cylinder in construction and also under the effects of operating conditions. Local gap between the skirt and bore surfaces at each node is calculated by

$$h^{i,j} = c + \left[e_t \left(1 - \frac{x^{i,j}}{L} \right) + e_b \frac{x^{i,j}}{L} \right] \cos\alpha^{i,j} + d_{ba}^{i,j} + d_{ov}^{i,j} + d_{th}^{i,j} + d_{el}^{i,j} \tag{3.23}$$

where $d_{ba}^{i,j}$ and $d_{ov}^{i,j}$ represents the deviation for the barrel and oval forms of skirt, respectively. Barrel form in the axial direction enhances pressure generation in lubricant film especially when the piston is tilted. In addition, an oval form in the circumferential direction can be introduced to maintain a more uniformly-pressurized film. Local gap is also affected by the shape changes in skirt and bore. This change results from non-uniform heating of the skirt and forces acting on it. In equation 3.23, change in local gap due to thermal and elastic deformations are denoted by $d_{th}^{i,j}$ and $d_{el}^{i,j}$, respectively.

Nominal clearance is defined at the apex point at which skirt diameter is the largest. Deviation due to barrel from is zero at this point and has positive values as it moves away in the axial direction. Likewise, oval deviation is measured from the perfectly-cylindrical piston which is smaller than bore as much as nominal clearance in radius. Figure 3.6 shows a schematic representation of barrel and oval profiles.

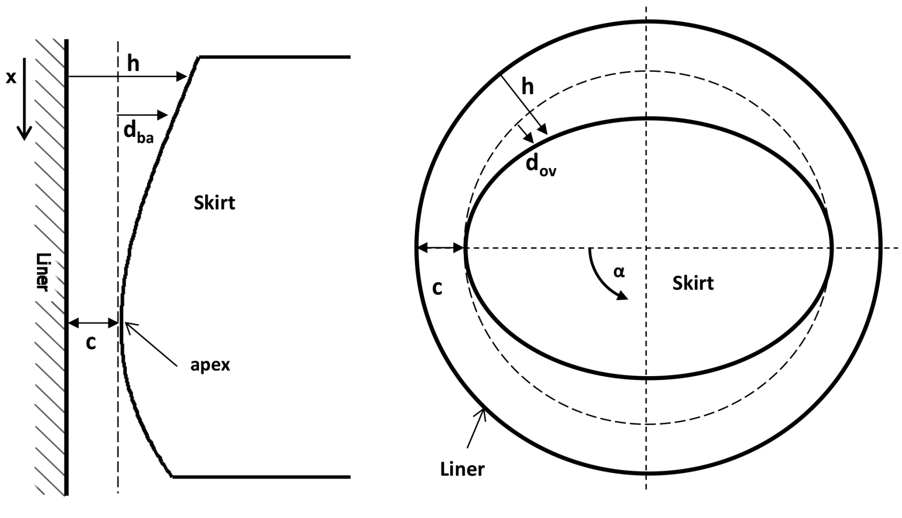

Figure 3.6 : Schematic representation of barrel and oval skirt profiles.

In this study, constant engine operating conditions are analyzed. After the piston reaches to steady-state temperatures for a specific engine load and speed, deviation due to thermal expansion remains unchanged. Therefore, a thermal analysis is run once and final form of skirt is predicted for the hot piston. This data is then used in film thickness calculation. Thermal analysis has to be repeated in order to investigate different operating conditions.

Elastic deformations occur under the forces acting on the piston body. Skirt profile is affected by hydrodynamic lubricant pressure and asperity contact forces. Change in skirt profile also affects lubrication. Therefore these two requires a coupled solution.

In order to calculate elastic deformations under distributed skirt loads, a stiffness matrix is obtained for the piston. A FE structural analysis is carried out in ANSYS software. Domain of interest is restricted to surface nodes in the lubrication region which are shown as a structural mesh in Figure 3.2 reducing the size of stiffness matrix. In every motion iteration, nodal deformations have to be calculated under the nodal forces found from pressure distribution. Therefore, a number of computations including matrix transformations have to be repeated. In order to solve for the deformations

$$\begin{bmatrix} u^{1,1} \\ u^{1,2} \\ \vdots \\ u^{1,n} \\ u^{2,1} \\ \vdots \\ u^{2,n} \\ \vdots \\ u^{m,1} \\ \vdots \\ u^{m,n} \end{bmatrix} = \begin{bmatrix} C^{1,1} & C^{1,2} & \dots & C^{1,mn-1} & C^{1,mn} \\ C^{2,1} & C^{2,2} & \dots & C^{2,mn-1} & C^{2,mn} \\ C^{3,1} & C^{3,2} & \dots & C^{3,mn-1} & C^{3,mn} \\ \vdots & \vdots & & \vdots & \vdots \\ \vdots & \vdots & & \vdots & \vdots \\ \vdots & \vdots & & \vdots & \vdots \\ \vdots & \vdots & & \vdots & \vdots \\ \vdots & \vdots & & \vdots & \vdots \\ \vdots & \vdots & & \vdots & \vdots \\ C^{mn-1,1} & C^{mn-1,2} & \dots & C^{mn-1,mn-1} & C^{mn-1,mn} \\ C^{mn,1} & C^{mn,2} & \dots & C^{mn,mn-1} & C^{mn,mn} \end{bmatrix}^{-1} \begin{bmatrix} F_h^{1,1} \\ F_h^{1,2} \\ \vdots \\ F_h^{1,n} \\ F_h^{2,1} \\ \vdots \\ F_h^{2,n} \\ \vdots \\ F_h^{m,1} \\ \vdots \\ F_h^{m,n} \end{bmatrix} \tag{3.24}$$

is calculated where $u^{i,j}$ is the radial displacement at each node. In this equation, compliance matrix is constant. Force vector on the RHS of the equation has to be formed by transforming nodal normal force matrix with the use of mapping matrices. After displacement vector is calculated, it has to be transformed back to (mxn) nodal displacement matrix, $d_{el}^{i,j}$.

Each time a pressure distribution is required, elastic distortion have to be iterated as well. Therefore this brings the third iteration into the solution code, which can be named as deformation iteration.

3.4 Determination of Solution Domain

In Section 3.2, domain is defined in a region of skirt surface which is geometrically designed for lubrication. However, pressure cannot develop over the entire lubrication region. Oil film on the surfaces is initially at the constant ambient pressure with a thickness determined by oil supply mechanisms. When the local gap at the leading side reduces below the supply oil thickness, pressure starts to develop in the lubricant film. Positive gage pressure is kept until the film rupture or cavitation occurs. In addition to the inlet and outlet boundaries in the direction of flow, the pressure zone may also be bounded in the circumferential direction due to the increase in local gap depending on the ovality of the skirt. These boundaries have to be estimated in order to specify the domain in which Reynolds equation solution is carried out.

Inlet locations can be determined provided that local clearance and supply oil film thickness are known. Oil resting on the bore surface is trapped between the sliding surfaces due to the converging passage at the leading edge. In this study, once the supply oil film thickness, h_{inlet}, is predicted, inlet location is found in the beginning of each pressure distribution solution as the local clearance drops below this value.

Outlet locations are where film rupture occurs satisfying the modified Reynolds film separation condition. Details were given in Section 2.1.2.2 for a one-dimensional flow. Reynolds cavitation proposes no-flow across the boundary. In a two-dimensional solution, Reynolds (Swift-Steiber) boundary conditions are:

$$at \quad x = x_p,\ y = y_p, \quad p = p_2,\ \frac{\partial p}{\partial x} = 0,\ \frac{\partial p}{\partial y} = 0 \tag{3.25}$$

Integrating Reynolds equation and applying the boundary conditions to find the integration constants would complicate the solution in a two-dimensional domain. Instead, in this study, it is preferred to find the cavitation boundary via iteration. The iteration was based on detecting the nodes with pressures below trailing edge pressure and shifting the outlet node against flow direction until negative relative pressures are eliminated. No-flow boundary condition was satisfied when the south (or north) node pressure was found to be equal or higher than the outlet node pressure while piston was moving towards TDC (or BDC). A sketch showing the iteration for cavitation boundary is given in Figure 3.7.

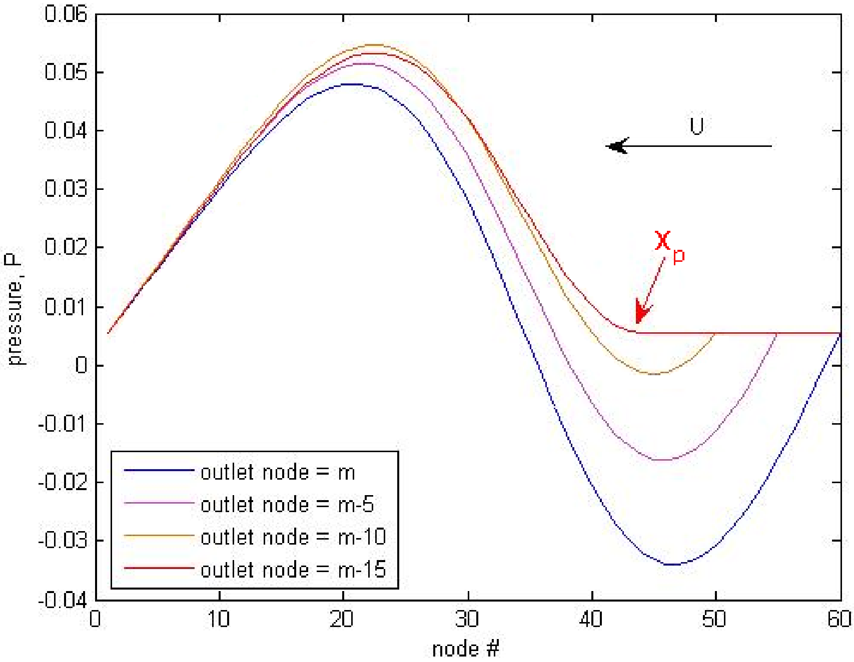

Figure 3.7 : Change in pressure distribution with marching outlet location.

As a result of flow separation after the outlet, the strip-like patterns of lubricant left beyond the cavitation boundary can be neglected since load carrying capacity of steam-like lubricant is limited. This way, mass conservation across the cavitation boundary is also satisfied.

Once the no-flow condition is satisfied in X-direction, it will be satisfied in Y-direction, too. This can only be violated at a point shown in Figure 3.8a. However, expected cavitation boundary behavior is approximately similar to that shown in Figure 3.8b, due to increase in film thickness away from the symmetry line.

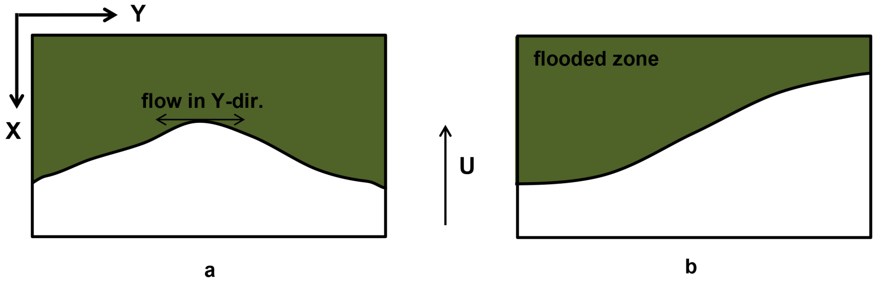

Figure 3.8 : Cavitation boundary characteristic a) violating the assumption of no-flow in Y-direction and b) expected.

3.5 Calculation of Forces and Moments

3.5.1 Lateral pin force

From kinematic analysis of piston and connecting rod assembly, piston axial velocity and acceleration, connecting rod axial and lateral accelerations and connecting rod tilt angle can be written as functions of crank angle as:

$$U = r\omega\left(\sin(\theta) + \frac{r}{2C_{MP}}\sin(2\theta)\right) \tag{3.26}$$

$$A_{Pz} = r\omega^2\left(\cos(\theta) - \frac{r}{C_{MP}}\cos(2\theta)\right) \tag{3.27}$$

$$A_{Bx} = r\omega^2\left(\cos(\theta) - \frac{r}{2C_{BM}}\cos(2\theta)\right) \tag{3.28}$$

$$A_{Bz} = r\omega^2\left(\frac{C_{BM}}{C_{MP}} - 1\right)\sin(\theta) \tag{3.29}$$

$$\beta = \sin^{-1}\left(\frac{r}{C_{MP}}\sin(\theta)\right) \tag{3.30}$$

Gas force is calculated by combustion chamber pressure at any crank angle as:

$$F_g = \pi R^2 p_g \tag{3.31}$$

For any piston position and orientation at any crank angle, tangential force on skirt surface is found after film thickness and pressure distribution is obtained.

$$F_f = -sign(U)2\sum f_f^{i,j} \tag{3.32}$$

where

$$f_f^{i,j} = \left(\tau^{i,j} + \mu_f p_c^{i,j}\right)\Delta A \tag{3.33}$$

is the nodal friction force and 2 is a factor due to the symmetric solution for half of skirt surface. The summation in equation 3.32 can be taken over entire lubrication region since nodes outside Reynolds solution domain have value for friction pressure.

Inserting equations 3.27 to 3.32 into equation 2.11, lateral pin force can obtained.

3.5.2 Normal force

Normal force acting on piston skirt results from hydrodynamic oil pressure and asperity contact pressure in case of solid contact. Total nodal force is then

$$f_h^{i,j} = \left(p^{i,j} + p_c^{i,j}\right) \Delta A \tag{3.34}$$

and normal force can be written as

$$F_h = 2 \sum f_h^{i,j} \cos\left(\alpha^{i,j}\right) \tag{3.35}$$

This summation is also taken over entire lubrication regime. Pressures at the nodes outside the Reynolds solution domain are set to zero gage value.

3.5.3 Moments on piston skirt

Moments created by normal and tangential skirt forces around piston pin is calculated by

$$M_h = 2 \sum \left[f_h^{i,j} \cos\left(\alpha^{i,j}\right) \left(C_P - x^{i,j}\right) \right] \tag{3.36}$$

and

$$M_f = 2 \sum \left[f_f^{i,j} R \cos\left(\alpha^{i,j}\right) \right] \tag{3.37}$$

respectively. Moment due to pin-piston interaction is neglected in this study.

3.6 Solution for Piston Secondary Motion

Secondary motion of piston can now be obtained using equations of motions given in Eqs. 2.15. The coefficients on the right hand side are known from inputs. Force and moment terms on the left hand side are functions of lateral piston position and velocity, but the functional dependence is not known explicitly. Therefore, equations are solved through an iterative procedure.

Eqs. 2.15 involves the data of lateral position, velocity and acceleration of both piston top and bottom resulting in six unknowns whereas the system can be solved for only two of them. However, position, velocity and acceleration can be numerically related to each other with Euler Forward Method expressions using the values from previous time step once any one of them is known.

$$\ddot{e}_t^{(t)} = \frac{\dot{e}_t^{(t)} - \dot{e}_t^{(t-\Delta t)}}{\Delta t} \tag{3.38a}$$

$$\ddot{e}_b^{(t)} = \frac{\dot{e}_b^{(t)} - \dot{e}_b^{(t-\Delta t)}}{\Delta t} \tag{3.38b}$$

$$\dot{e}_t^{(t)} = \frac{e_t^{(t)} - e_t^{(t-\Delta t)}}{\Delta t} \tag{3.39a}$$

$$\dot{e}_b^{(t)} = \frac{e_b^{(t)} - e_b^{(t-\Delta t)}}{\Delta t} \tag{3.39b}$$

With the current form of the equations, accelerations are obtained first and then velocities and positions have to be calculated at each step. Instead, Eqs. 3.38 can be substituted into Eqs. 2.15 and velocities can be obtained directly. This eliminates acceleration to velocity transition at every iteration step reducing computational load on the code. This approach may be applied to velocities writing $\dot{e}_t^{(t)}$ and $\dot{e}_b^{(t)}$ in terms of positions as well. This method is not actually any beneficial for computational load, but in this study motion iterations are found to be more stable when they are carried in lateral position. Therefore, Eqs. 3.39 are substituted into Eqs. 3.38 to obtain

$$\ddot{e}_t^{(t)} = \frac{e_t^{(t)} - e_t^{(t-\Delta t)}}{(\Delta t)^2} - \frac{\dot{e}_t^{(t-\Delta t)}}{\Delta t} \tag{3.40a}$$

$$\ddot{e}_b^{(t)} = \frac{e_b^{(t)} - e_b^{(t-\Delta t)}}{(\Delta t)^2} - \frac{\dot{e}_b^{(t-\Delta t)}}{\Delta t} \tag{3.40b}$$

and Eqs. 2.15 can be written in terms of piston lateral position:

$$\begin{aligned} &F_h + F_{rz} + mg\sin\kappa \\ &\qquad + \frac{m}{\Delta t}\left[\left(1 - \frac{C_{CM}}{L}\right)\left(\dot{e}_t^{(t-\Delta t)} + \frac{e_t^{(t-\Delta t)}}{\Delta t}\right) + \frac{C_{CM}}{L}\left(\dot{e}_b^{(t-\Delta t)} + \frac{e_b^{(t-\Delta t)}}{\Delta t}\right)\right] \\ &\qquad\qquad = \frac{m}{(\Delta t)^2}\left[\left(1 - \frac{C_{CM}}{L}\right)e_t^{(t)} + \frac{C_{CM}}{L}e_b^{(t)}\right] \end{aligned} \tag{3.41a}$$

$$\begin{aligned} &M_h + M_f + mg\sin\kappa(C_P - C_{CM}) - mg\cos\kappa(d_{CM} + d_P) \\ &\qquad + \frac{I_P}{L\Delta t}\left(\dot{e}_t^{(t-\Delta t)} + \frac{e_t^{(t-\Delta t)}}{\Delta t} - \dot{e}_b^{(t-\Delta t)} - \frac{e_b^{(t-\Delta t)}}{\Delta t}\right) \\ &\qquad\qquad = \frac{I_P}{L(\Delta t)^2}\left(e_t^{(t)} - e_b^{(t)}\right) \end{aligned} \tag{3.41b}$$

Another improvement to computation speed can be implemented by normalizing the equations of motion. This not only eliminates switching between dimensional and non-dimensional eccentricities and velocities to calculate local film thickness and squeeze film velocity at each motion iteration step, but also brings further stability to the code. For this purpose, non-dimensional eccentricity and its time derivatives are defined as:

$$\varepsilon = \frac{e}{c} \tag{3.42a}$$

$$\dot{\varepsilon} = \frac{\dot{e}}{c\omega} \tag{3.42b}$$

$$\ddot{\varepsilon} = \frac{\ddot{e}}{c\omega^2} \tag{3.42c}$$

Making use of non-dimensional time given in equation 3.2d equations 3.38 and 3.39 can be rewritten as:

$$\ddot{\varepsilon}_t^{(T)} = \frac{\dot{\varepsilon}_t^{(T)} - \dot{\varepsilon}_t^{(T-\Delta T)}}{\Delta T} \tag{3.43a}$$

$$\ddot{\varepsilon}_b^{(T)} = \frac{\dot{\varepsilon}_b^{(T)} - \dot{\varepsilon}_b^{(T-\Delta T)}}{\Delta T} \tag{3.43b}$$

$$\dot{\varepsilon}_t^{(T)} = \frac{\varepsilon_t^{(T)} - \varepsilon_t^{(T-\Delta T)}}{\Delta T} \tag{3.44a}$$

$$\dot{\varepsilon}_b^{(T)} = \frac{\varepsilon_b^{(T)} - \varepsilon_b^{(T-\Delta T)}}{\Delta T} \tag{3.44b}$$

Applying this normalization, local film thickness given in equation 3.23 takes the following non-dimensional form:

$$H^{i,j} = 1 + \left[\varepsilon_t\left(1 - \frac{X^{i,j}}{2}\right) + \varepsilon_b\frac{X^{i,j}}{2}\right]\cos\alpha^{i,j} + \frac{d_{ba}^{i,j}}{c} + \frac{d_{ov}^{i,j}}{c} + \frac{d_{th}^{i,j}}{c} + \frac{d_{el}^{i,j}}{c} \tag{3.45}$$

In this equation, only the last term representing the local elastic deformation has to be normalized repeatedly at each step. Other deformation terms which are due to barrel and oval profiles and thermal distortion are calculated once in the beginning of the run. These terms does not appear in local squeeze film velocity which can be written as

$$\dot{H}^{i,j} = \left[\dot{\varepsilon}_t\left(1 - \frac{X^{i,j}}{2}\right) + \dot{\varepsilon}_b\frac{X^{i,j}}{2}\right]\cos\alpha^{i,j} \tag{3.46}$$

In order to obtain normalized equations of motion equation 3.40a is divided by $mc\omega^2$ and equation 3.40b is multiplied by $\frac{L}{I_{PC}\omega^2}$. Finally, substituting non-dimensional time and piston top and bottom velocities into equations 3.40 and 3.41 and arranging

$$F_{var}+F_{const}+F_{\varepsilon}^{(T-\Delta T)}=\left(1-\frac{C_{CM}}{L}\right)\varepsilon_t^{(T)}+\frac{C_{CM}}{L}\varepsilon_b^{(T)} \tag{3.47a}$$

$$M_{var}+M_{const}+M_{\varepsilon}^{(T-\Delta T)}=\varepsilon_t^{(T)}-\varepsilon_b^{(T)} \tag{3.47b}$$

are written where subscripts '*var*' and '*const*' stand for values that are variable and constant, respectively, at a time step and

$$F_{var}=\frac{(\Delta T)^2}{mc\omega^2}\left(F_h+F_{rz}\right) \tag{3.48a}$$

$$F_{const}=\frac{(\Delta T)^2}{mc\omega^2}mg\sin\kappa \tag{3.48b}$$

$$\begin{aligned}F_{\varepsilon}^{(T-\Delta T)}=&\left(1-\frac{C_{CM}}{L}\right)\left(\Delta T\dot{\varepsilon}_t^{(T-\Delta T)}+\varepsilon_t^{(T-\Delta T)}\right)\\&+\frac{C_{CM}}{L}\left(\Delta T\dot{\varepsilon}_b^{(T-\Delta T)}+\varepsilon_b^{(T-\Delta T)}\right)\end{aligned} \tag{3.48c}$$

$$M_{var}=\frac{L(\Delta T)^2}{I_{PC}\omega^2}\left(M_h+M_f\right) \tag{3.48d}$$

$$M_{const}=\frac{L(\Delta T)^2}{I_{PC}\omega^2}mg\left[\sin\kappa(C_P-C_{CM})-\cos\kappa(d_{CM}+d_P)\right] \tag{3.48e}$$

$$M_{\varepsilon}^{(T-\Delta T)}=\Delta T\left(\dot{\varepsilon}_t^{(T-\Delta T)}-\dot{\varepsilon}_b^{(T-\Delta T)}\right)+\varepsilon_t^{(T-\Delta T)}-\varepsilon_b^{(T-\Delta T)} \tag{3.48f}$$

are obtained and set of equations to be solved for piston secondary motion becomes

$$\begin{bmatrix}1-\dfrac{C_{CM}}{L} & \dfrac{C_{CM}}{L}\\ 1 & -1\end{bmatrix}\begin{bmatrix}\varepsilon_t^{(T)}\\ \varepsilon_b^{(T)}\end{bmatrix}=\begin{bmatrix}F_{var}+F_{const}+F_{\varepsilon}^{(T-\Delta T)}\\ M_{var}+M_{const}+M_{\varepsilon}^{(T-\Delta T)}\end{bmatrix} \tag{3.49}$$

Two sets of initial conditions are introduced to start the iteration. First set includes the positions and velocities for the initial previous time step, $T=0-\Delta T$, which are used to calculate the velocities for the initial current time step, $T=0$. This set can be represented as:

$$at\quad T=0,\quad \varepsilon_t^{(T-\Delta T)}=0\,,\,\varepsilon_b^{(T-\Delta T)}=0\,,\,\dot{\varepsilon}_t^{(T-\Delta T)}=0\,,\,\dot{\varepsilon}_b^{(T-\Delta T)}=0 \tag{3.50}$$

The second set is the initial guess of eccentricities for the current time step:

$$at\quad T=0,\quad \varepsilon_t^{(T)}=0\,,\,\varepsilon_b^{(T)}=0 \tag{3.51}$$

Figure 3.9 shows the solution procedure for secondary motion of the piston. First iteration is the time iteration. At each time step force and moment balance is checked for a number of trial values for eccentricities. Once the lateral position is defined, squeeze film velocity can be found. Film thickness is calculated with a initial guess for elastic deformation and lubricant pressure distribution is obtained via pressure iteration for the solution of Reynolds equation. Pressure is compared to the previous distribution at $l-1$. If the difference is large, normal force and elastic deformation is calculated again and deformation iteration continues with the new pressure distribution. If the difference is small, the elastic deformation and normal force is taken as the solution and motion iteration continues with the calculation of other forces and moments. Force balance is checked. If not satisfied, new values for eccentricity are estimated to start a new motion iteration step, $k+1$. If force balance is achieved, all the calculated motion and force values are stored and time is advanced. The end of time iteration can either be decided by checking the cyclic convergence for piston motion or the number of power cycles can simply be set in the beginning.

An important stage of the solution procedure is motion iteration. A number of direct methods, which can be used to advance in time without any iteration for force balance, are found in the literature such as explicit Runge-Kutta Methods and also adaptive and implicit versions of the same family. In this study, direct solution methods for piston lateral motion is tried but could not succeed due to the stiffness. The solution is highly stiff under some conditions especially when piston moves from one side to the other where oil film contact has already been lost and piston tries to dive into the lubricant. In addition, nonlinearity of the system also constitutes a major problem especially in the coupled solution of film pressure and elastic deformations. Therefore, it is considered as a safe way of time forwarding without error accumulation to find the piston lateral position which satisfies the force and moment balance, in spite of the increased computational load with the inclusion of one more iteration.

Motion iteration is carried out using a modified version of Broyden's Method [55], which is also called the Good Broyden Method [56]. This method suggests a Jacobean matrix for the systems in which it cannot be obtained explicitly. It is updated at each step depending on the differences between successive values of dependent and independent variables of the system. Originally, new values of independent variables can be estimated by

$$\begin{bmatrix} \varepsilon_t \\ \varepsilon_b \end{bmatrix}^{k+1} = \begin{bmatrix} \varepsilon_t \\ \varepsilon_b \end{bmatrix}^{k} - B^{k^{-1}} F^{k} \tag{3.52}$$

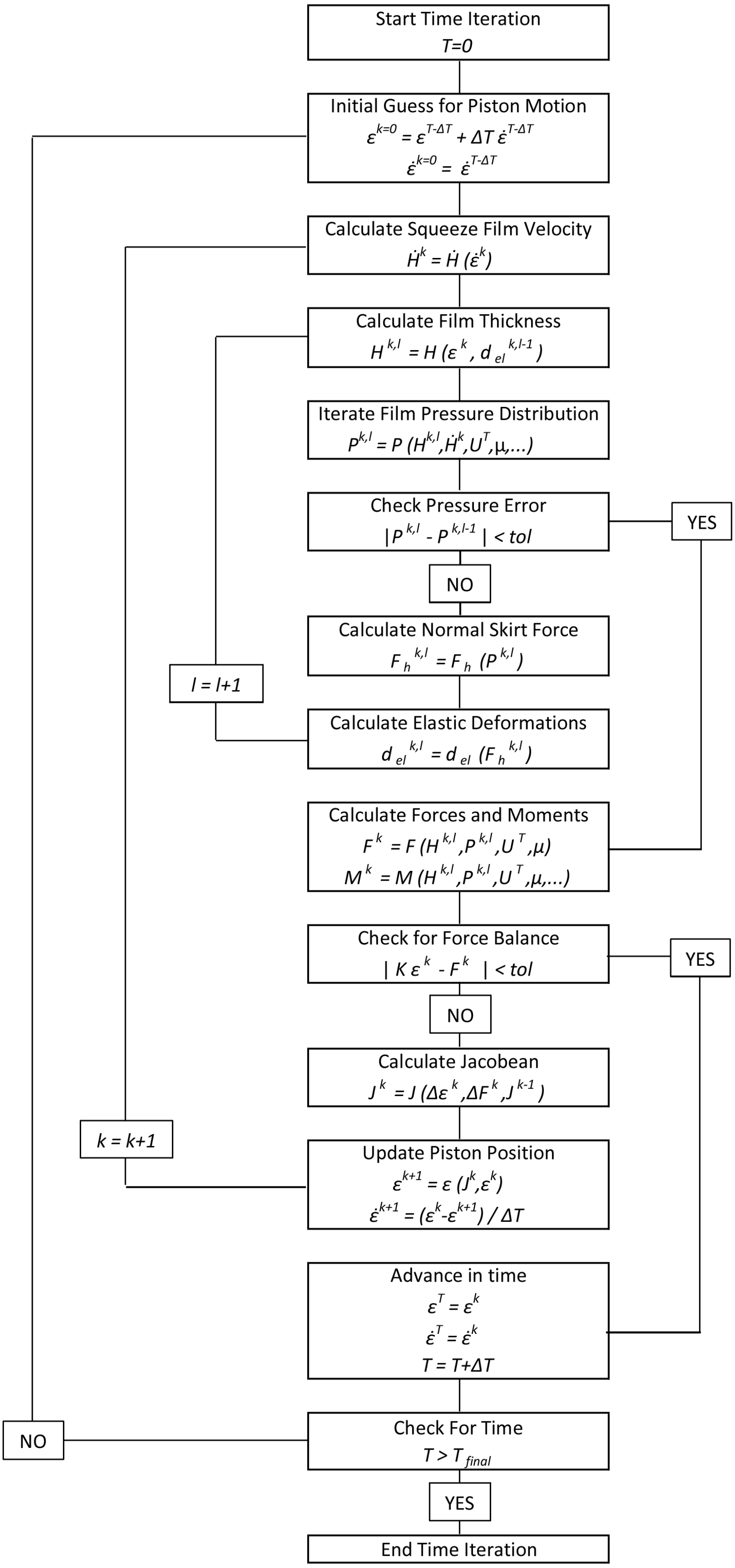

Figure 3.9 : Flow chart.

with the use of Jacobean which is

$$B^k = B^{k-1} + \left(f - B^{k-1}s\right)\frac{s^T}{s^T s} \tag{3.53}$$

where

$$s = \begin{bmatrix}\varepsilon_t \\ \varepsilon_b\end{bmatrix}^k - \begin{bmatrix}\varepsilon_t \\ \varepsilon_b\end{bmatrix}^{k-1} \tag{3.54}$$

$$f = F^k - F^{k-1} \tag{3.55}$$

In the last equation F is the function for force balance which is aimed to be equal to zero and it can be written as

$$F = \begin{bmatrix} F_{var} + F_{const} + F_{\varepsilon}^{(T-\Delta T)} - \left(1 - \frac{C_{CM}}{L}\right)\varepsilon_t^{(T)} - \frac{C_{CM}}{L}\varepsilon_b^{(T)} \\ M_{var} + M_{const} + M_{\varepsilon}^{(T-\Delta T)} - \varepsilon_t^{(T)} + \varepsilon_b^{(T)} \end{bmatrix} \tag{3.56}$$

Instead of updating the Jacobean and using the inverse of it, Broyden's Method also suggests an update to the inverse Jacobean matrix:

$$H^k = H^{k-1} + \left(s - H^{k-1}f\right)\frac{s^T H^{k-1}}{s^T H^{k-1} f} \tag{3.57}$$

In this study, inverse Jacobean is used to estimate the new values of eccentricities to check for force balance:

$$\begin{bmatrix}\varepsilon_t \\ \varepsilon_b\end{bmatrix}^{k+1} = \begin{bmatrix}\varepsilon_t \\ \varepsilon_b\end{bmatrix}^k - H^k F^k \tag{3.58}$$

4. RESULTS AND DISCUSSION

The code generated to solve piston secondary motion and skirt friction was run for a number of different cases to investigate the effect of geometrical and operational parameters on friction loss. A 9 lt., 6-cylinder, turbocharged diesel engine utilizing aluminum pistons was selected. General specifications and input parameters for the base configuration is given in Table 4.1.

Table 4.1 : General input data.

input	nomenclature	value	unit
Engine Parameters			
R	piston radius	57,5	mm
L	piston skirt length	79,3	mm
r	crank radius	72	mm
C_{MP}	connecting rod length	231	mm
C_{BM}	distance to connecting rod mass center from big end	71,66	mm
C_{CM}	distance to piston mass center from skirt top	10,80	mm
C_P	distance to wrist-pin axis from skirt top	37,3	mm
m	piston mass	1,55	kg
I_P	piston moment of inertia	3070	$kg.mm^2$
m_B	connecting rod mass	2,89	kg
I_B	connecting rod moment of inertia	28150	$kg.mm^2$
Surface Parameters			
σ_p	skirt roughness	0,20	μm
σ_b	bore roughness	0,50	μm
γ_p	skirt roughness orientation	1	-
γ_b	bore roughness orientation	1	-
Ω	skirt waviness	5	μm
Operational Parameters			
ω	crank speed	157,08 (1680)	rad/s (rpm)
h_{supp}	supply oil film thickness	20	μm
c	nominal clearance	20	μm
	oil type	SAE 15W-40	-
μ	dynamic viscosity (at 100°C)	11,92	cP
μ_f	friction coefficient	0,1	-

Baseline engine speeds is 1680 rpm. In-cylinder pressures are given in Figure 4.1 for two different engine loads at this speed. At full load, indicated mean effective pressure is 24.94 *bars*, whereas it is 13.25 *bars* at partial load.

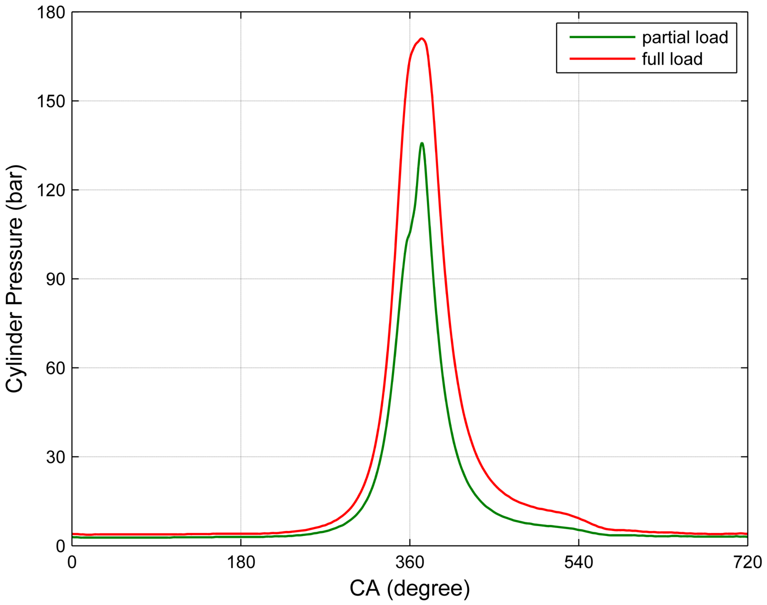

Figure 4.1 : In-cylinder pressure variation for full and partial loads at 1680 rpm.

Change in piston skirt profile due to temperature rise was calculated to be used as an input to the secondary dynamics solution. The steady-state temperature distribution for piston were estimated for full and partial load conditions as given in Figure 4.2. Thermal expansion as a result of heating of piston from room temperature to operating conditions was calculated. Figure 4.3 shows the change in skirt profile due to thermal expansion of piston. Partial load conditions were selected for investigation of focus parameters in this study.

4.1 Focus Parameters

In this study, a numerical code was generated that would be used to predict the piston skirt friction. This code can be run with a variety of input parameters that are expected to affect the secondary dynamics of piston, skirt lubrication and, therefore, frictional losses due to skirt-cylinder bore interaction. Some of these parameters are selected to be presented in this thesis, such that their effects tend to be more sensitive to the changes.

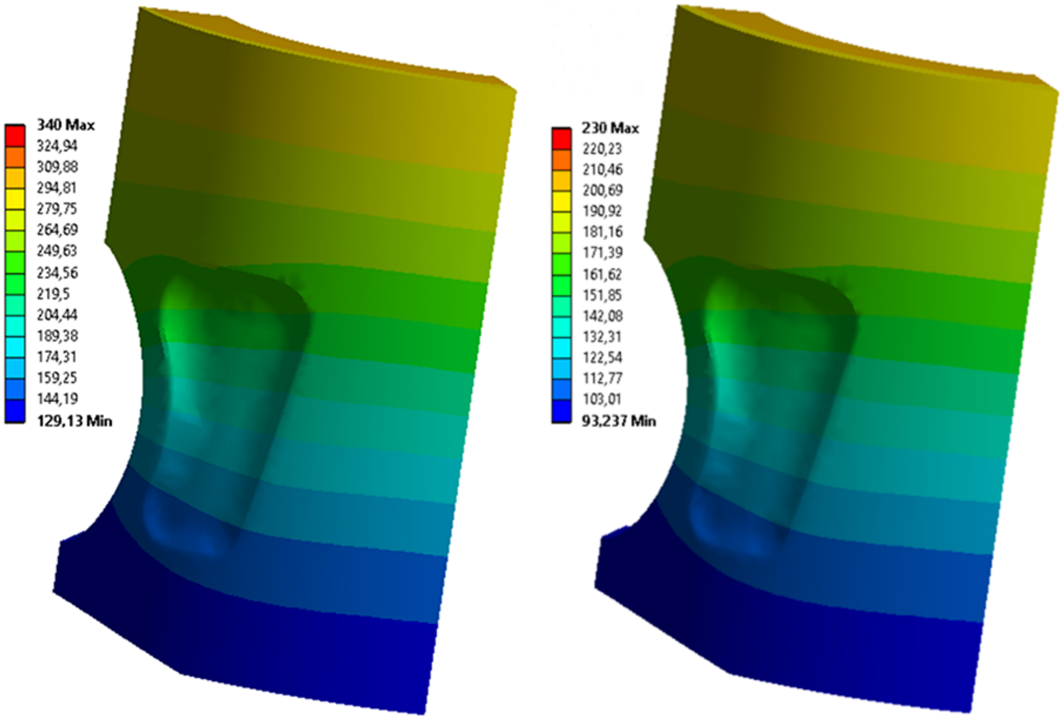

Figure 4.2 : Piston temperature distribution (°C) for full and partial loads at 1680 rpm.

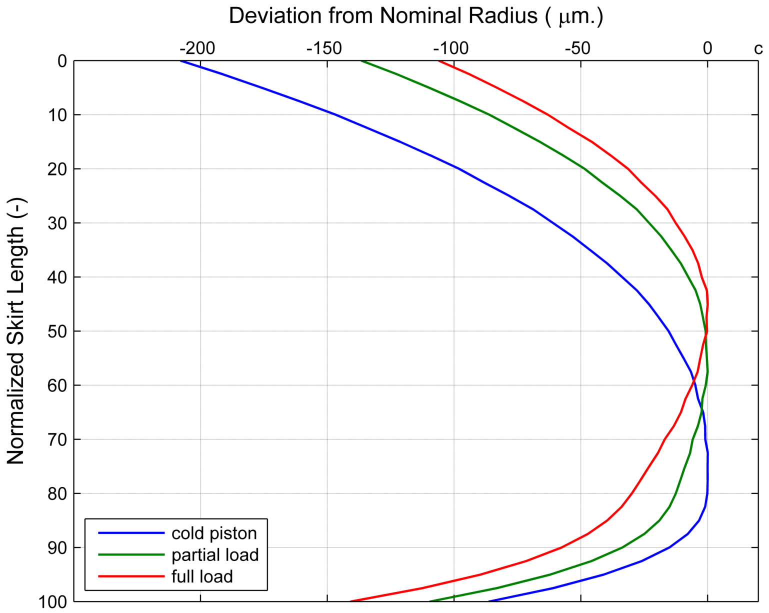

Figure 4.3 : Change in skirt profile due to thermal deformation for full and partial loads at 1680 rpm.

First of all, skirt profile was focused on. It can be decomposed into barrel and oval shapes. For the barrel shape, the location of the apex is also worth investigating since piston is expected to have a tilting motion which is strongly dependent on the positioning of lubricant pressure area and its effective center.

Barrel shape of the skirt significantly changes with respect to the cold profile when the engine heats up to operating temperatures. Therefore, operating conditions should first be specified in order to investigate effects of skirt profile on secondary dynamics. This study is carried out with a skirt of a partially loaded engine running at 1680 rpm. Original estimated hot profile, shown in Figure 4.3, was modeled with a 4th order polynomial in order to be able to make modifications. First set of profiles was created by changing radius of curvature above and below the apex point keeping topmost and bottommost deviation constant. The resulting profiles can be named as reduced and increased barrel shapes as shown in Figure 4.4.

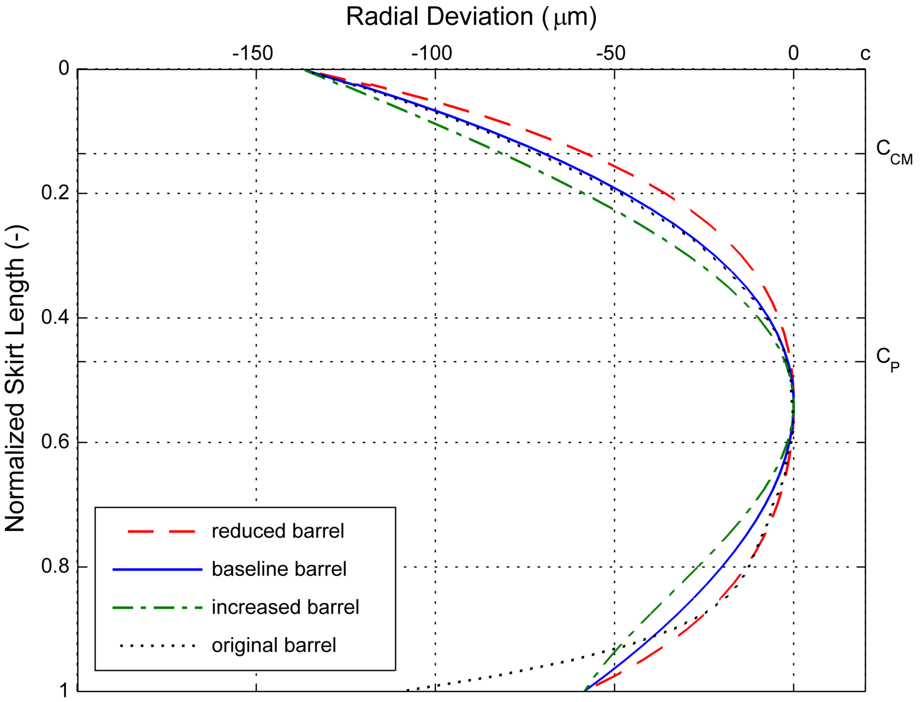

Figure 4.4 : Modified barrel shape of skirt.

Second set of skirt profiles was generated by changing the apex location. Radial deviation curve was simply shifted up and down keeping the curvature constant for the entire skirt length. Figure 4.5 shows the obtained profiles.

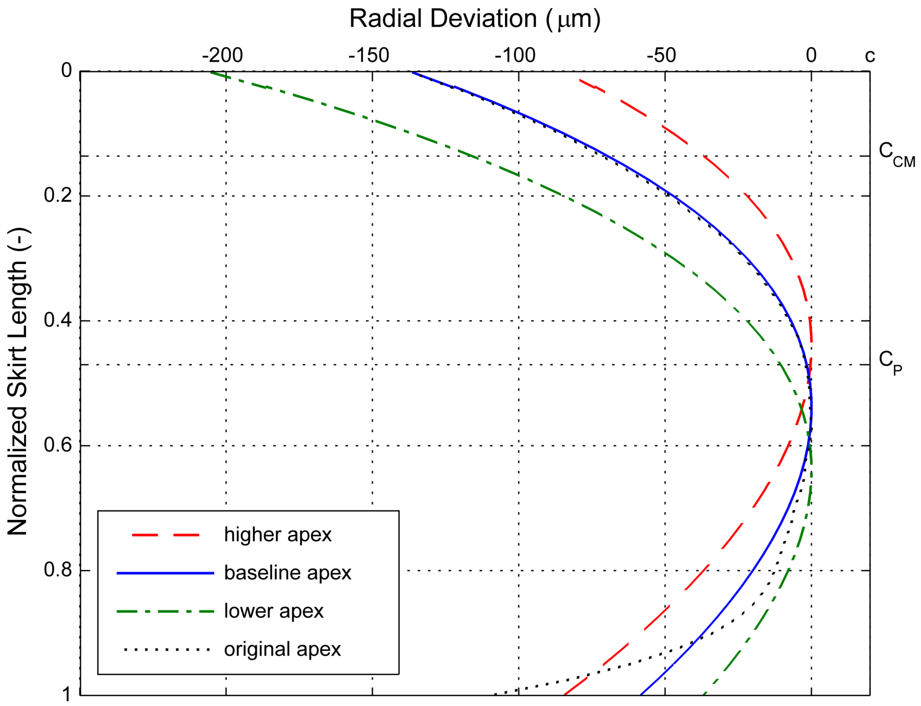

Figure 4.5 : Modified apex location of skirt.

Effect of skirt ovality was investigated with a third set obtained by modifying radial deviation in the circumferential direction. Increased and reduced oval profiles are given in Figure 4.6.

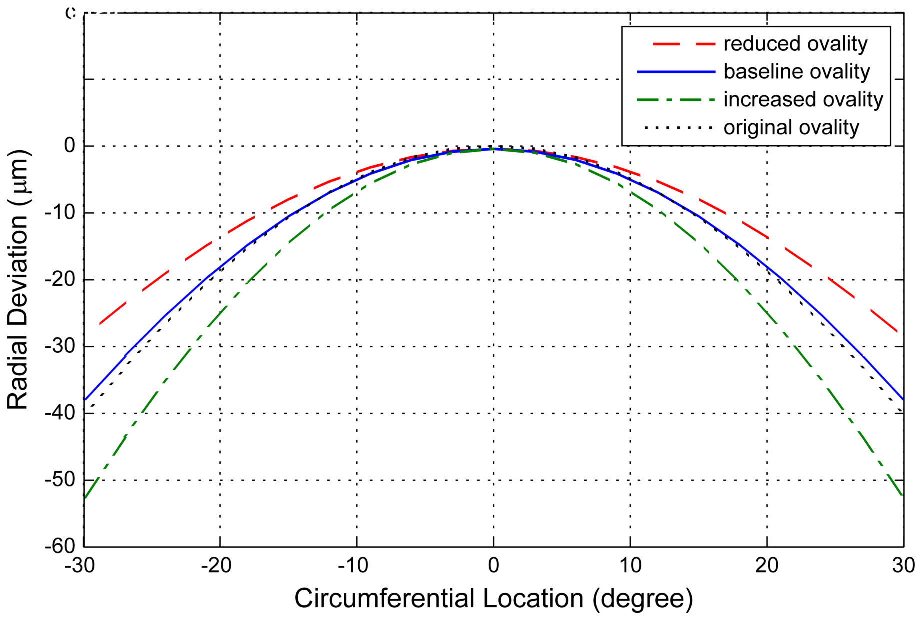

Figure 4.6 : Modified oval profile of skirt.

Another parameter which has direct effects on hydrodynamic lubrication is oil viscosity. It is known that high viscosity leads to higher film thicknesses minimizing solid-to-solid contact but increasing shear. Therefore, it is an optimization problem for the developer. Although it is generally an easy solution to try different viscosity grade oils, piston skirt is not the only component that uses the oil in the crankcase, so at the same time it actually requires a complementary design approach together with crank bearings, valves, turbocharger assembly, etc. Keeping this in mind, in this study, viscosity variations will still be dealt with different grade oils just to be able to make a comparison. Baseline engine uses SAE15W-40 oil. SAE10W-20, SAE10W-30 and SAE10W-50 oils for which the dynamic viscosities at an operating temperature of 100°Care given in Table 4.2 will be tested.

Table 4.2 : Dynamic viscosity values at 100°C for the oils analyzed.

SAE Oil Grade	Dynamic Viscosity [cP]
10W-50	15.41
15W-40 (baseline)	11.92
10W-30	9.63
10W-20	5.55

While these parameters are investigated, a number of case changes were tried to recommend more efficient pistons under the specified running conditions.

4.2 Partially-Flooded Inlet Results

The amount of oil resting on the cylinder bore as the piston approaches is important for the lubrication characteristics. However, it is difficult to predict this amount at the leading edge. Crank splashing and oil jet mechanisms that transport the oil from crankcase to the cylinder walls determines the inlet condition when the piston travels downwards. In this case, a high amount of oil on the cylinder wall can be expected. On the other hand, when the piston moves towards the TDC, oil in front of the piston is generally output of the oil ring. Therefore, ring tension and geometry can be said to play a key role for lubrication during compression and exhaust strokes. These parameters need to be inveIn order to prevent thisstigated for a more realistic skirt lubrication analysis. In this study, supply oil was taken as constant for the entire stroke to keep the model rather simple.

Oil resting on the cylinder wall is pushed forward in front of the skirt surface as the piston moves. In addition to this, due to surface tension, a higher thickness compared to freely resting oil can be assumed at the inlet of the effective lubrication length. In previous studies, this value had been assumed to vary up to 100 μm starting from 0 to simulate dry or no lubrication conditions [6, 16, 19].

The first trials with the developed model was carried out with a supply oil thickness of 20 μm in this study. In this section, these results will be presented and this case will be considered as partially-lubricated condition.

4.2.1 Effect of barrel shape

It was seen that lateral displacement of wrist-pin axis increases very slightly as the barrel shape gets more distinct, whereas tilting motion increases significantly while the trend remains the same (Figure 4.7). The increase in tilt motion is more during downstrokes which shows the effective center of application of pressure force moves away from the wrist-pin axis location when the profile has an increased barrel form. Minimum film thickness is slightly lower most of the cycle for the increased barrel case (Figure 4.8) as it penetrates more into the lubricant film due to lower radius of curvature. During the second half of expansion stroke, minimum film thicknesses are quite the same as major thrust side rests on wave peaks. Low radius of curvature also gives way to smaller lubricated areas and higher elastic deformation due to more concentrated pressures (Figure 4.9).

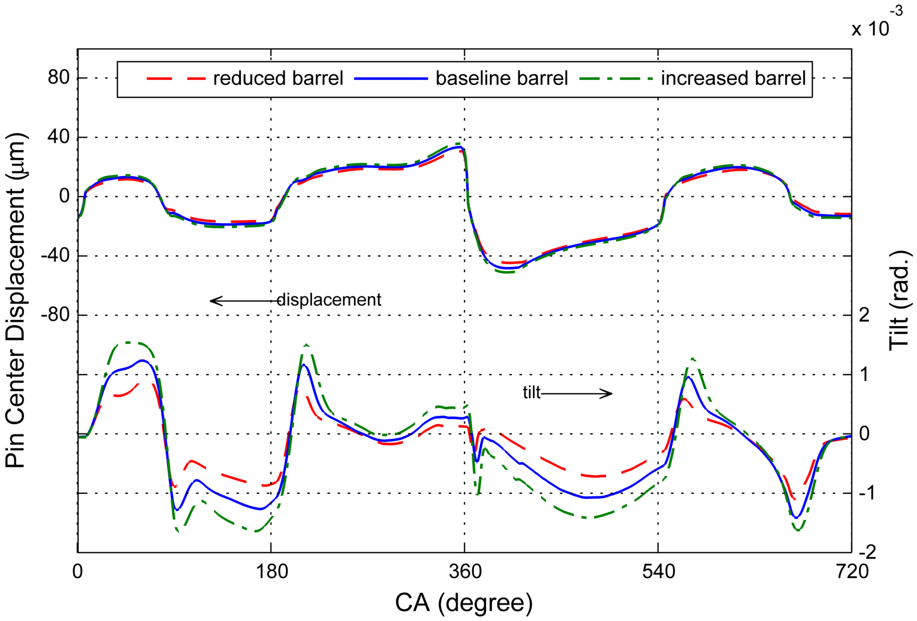

Figure 4.7 : Pin center displacement and tilt for the change in barrel form (partially-flooded inlet).

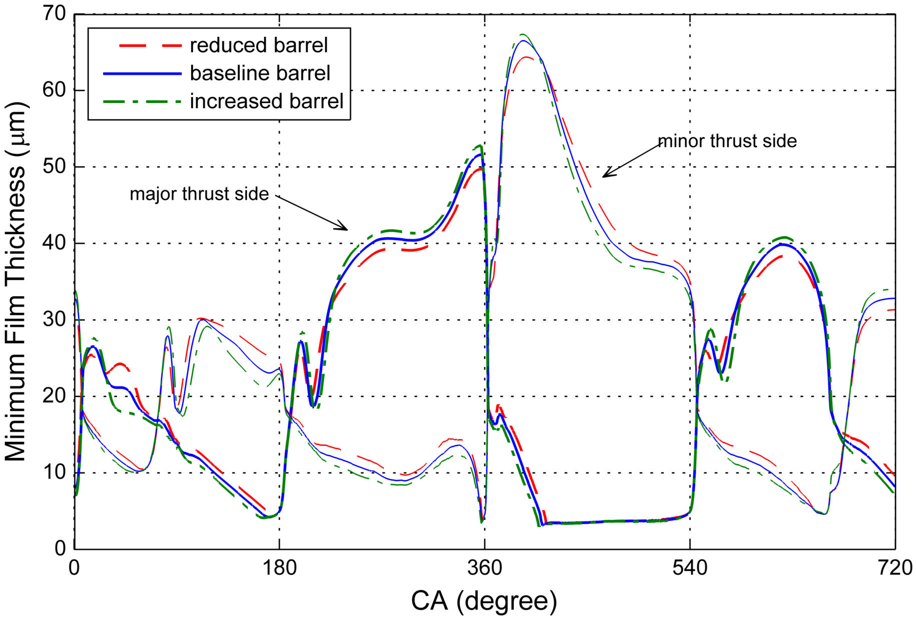

Figure 4.8 : Minimum film thickness variation for the change in barrel form (partially-flooded inlet).

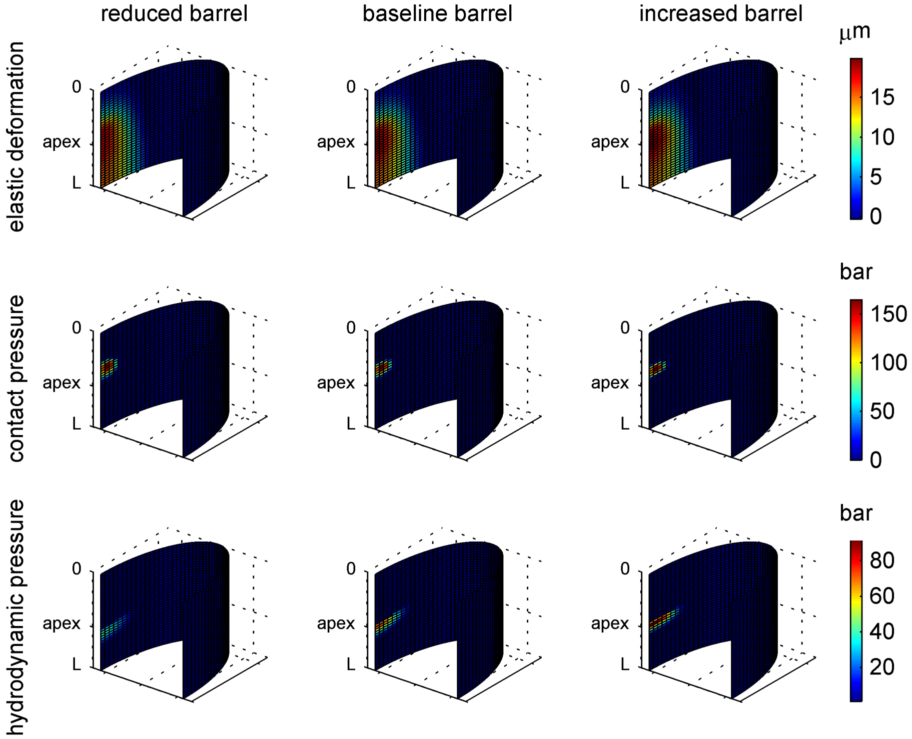

Figure 4.9 : Elastic deformation, contact and hydrodynamic pressures at 90°CA after FTDC for the change in barrel form (partially-flooded inlet).

Lateral and friction forces acting on piston skirt is shown in Figures 4.10 and 4.11. Boundary friction force was found to be significantly high in the second half of expansion stroke. Once solid contact occurs, it seems there is not much difference between the barrel shapes. Reduced barrel undergoes slightly higher contact friction. On the other hand, hydrodynamic friction is significantly higher since lubricated zone is larger.

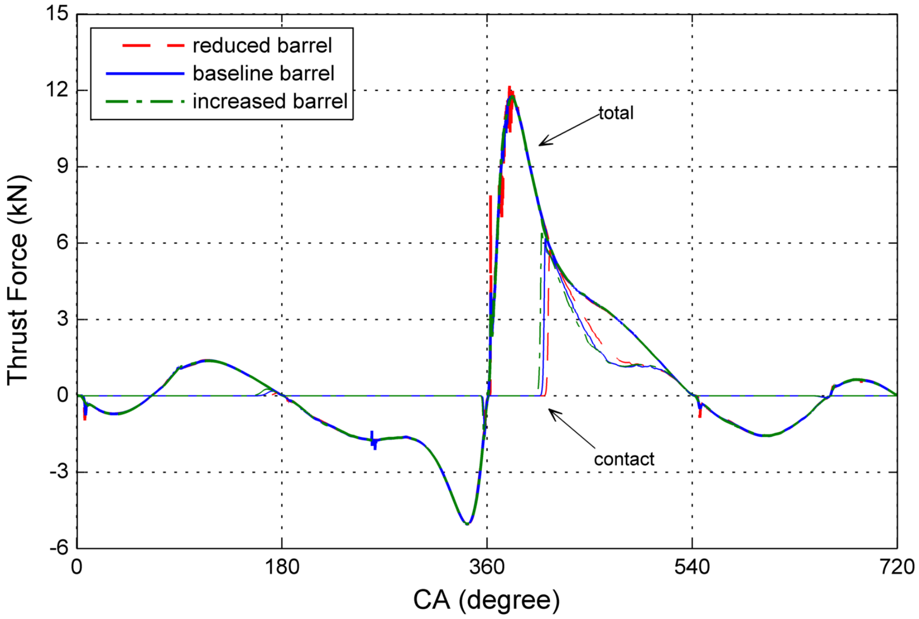

Figure 4.10 : Thrust force components for the change in barrel form (partially-flooded inlet).

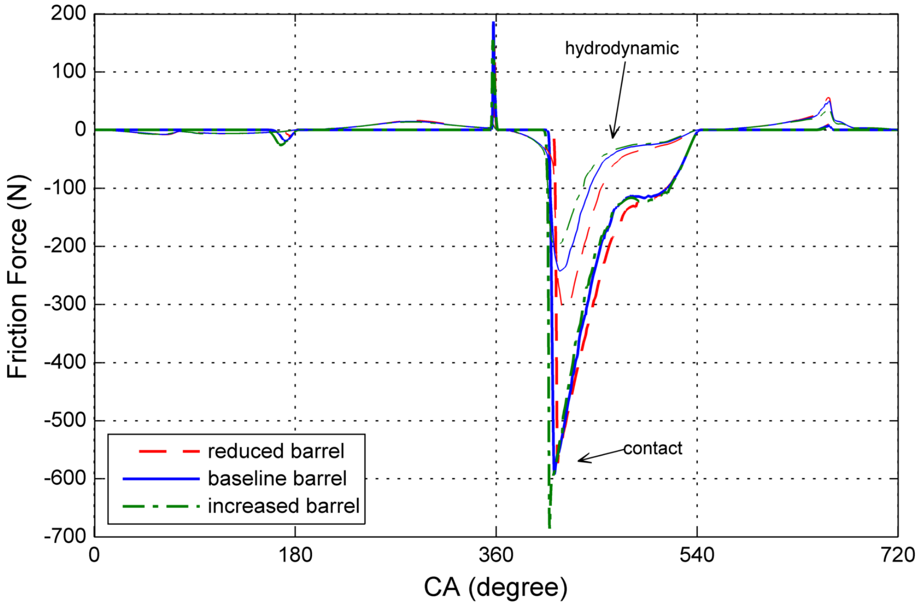

Figure 4.11 : Friction force for the change in barrel form (partially-flooded inlet).

It was seen that boundary friction loss is higher for increased barrel form (Table 4.3). On the other hand a reduction in viscous friction was observed which is slightly more effective in total loss when the radius of curvature is lower.

Table 4.3 : Indicated and friction mean effective pressures and ratios of friction power loss to indicated power for the change in barrel form under partial load (partially-flooded inlet).

imep = 13.25 bar	viscous fmep	boundary fmep	total fmep	% power loss
reduced barrel form	0.130	0.196	0.325	2.46 %
baseline barrel form	0.105	0.197	0.302	2.28 %
increased barrel form	0.091	0.205	0.296	2.23 %

4.2.2 Effect of apex location

Apex of the baseline barrel profile is slightly lower than wrist-pin location (Figure 4.5). When the apex is moved towards piston bottom, it gets further away from pin axis. On the other hand, in the case of higher apex, it is located over the pin. Change in the position of barrel apex point with respect to wrist-pin axis, which is the axis piston rotates about, also changes the secondary motion of piston. Lower apex results in an exaggerated movement when compared to baseline case (Figure 4.12). For the higher

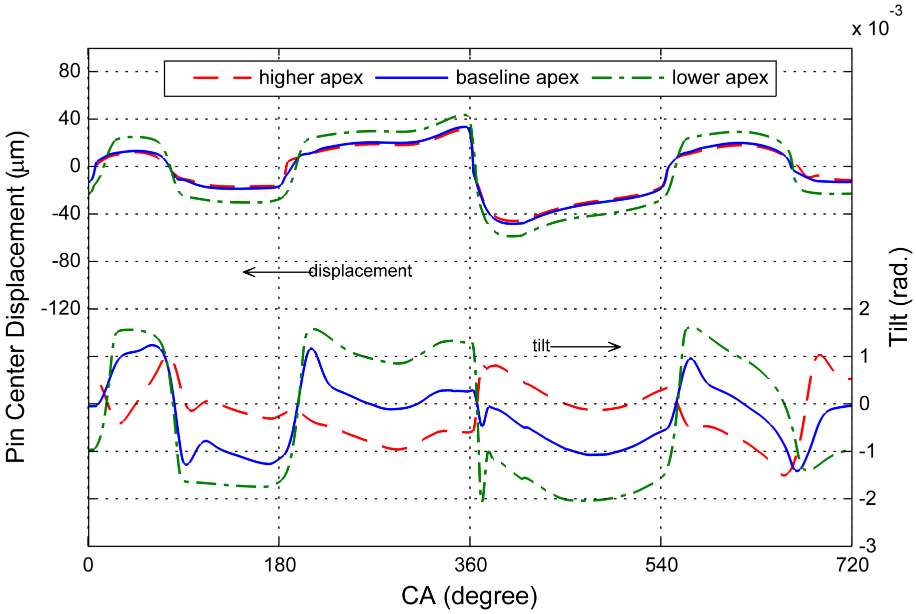

Figure 4.12 : Pin center displacement and tilt for the change in apex location (partially-flooded inlet).

apex location, lateral translation remains unchanged. However, piston tilts in opposite directions especially in compression and expansion strokes.

Minimum film thickness variation is also given in Figure 4.13. It is interesting that for the lower apex location case, film thicknesses at the minor thrust side were quite low when the piston is moving on the major thrust side during late intake and expansion strokes and this is considered as the effect of the excessive tilt angles. The values are below the supply oil thickness which leads to hydrodynamic pressure development and extra viscous friction on the minor side. However, friction acting on the minor thrust side is approximately 5% of that on the major thrust side.

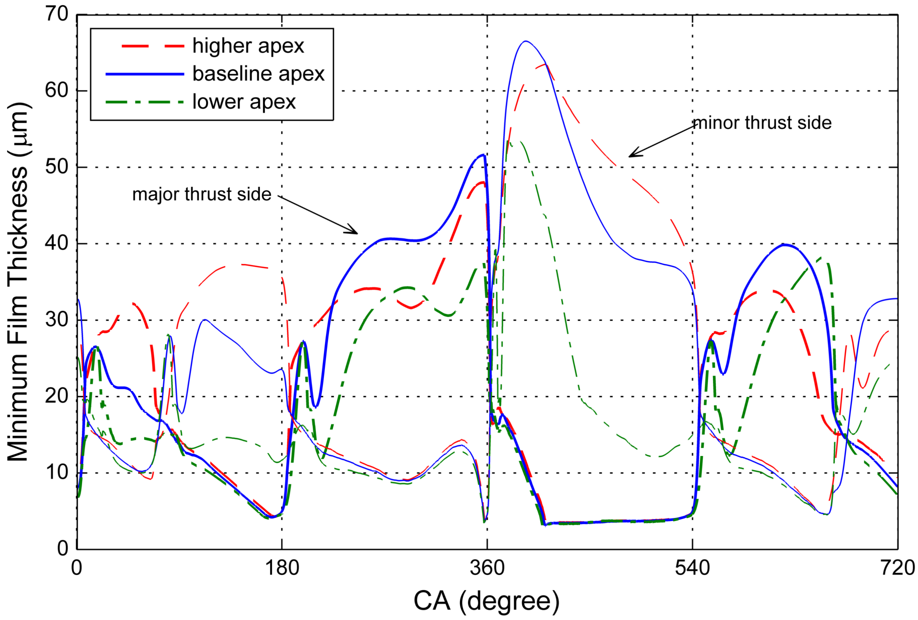

Figure 4.13 : Minimum film thickness variation for the change in apex location (partially-flooded inlet).

Figure 4.14 shows that pressures and elastic deformations on the skirt surface are concentrated at almost the same area. This is also interesting that even though the apex location is quite different, tilting motion adjusts the piston around wrist-pin axis to maintain the moment balance.

Figure 4.15 shows that dominant boundary contact was observed in the second half of expansion stroke. Lower hydrodynamic friction was found with a lower apex location. Approximately the same boundary friction was observed for baseline and higher apex profiles (Figure 4.16). Boundary friction was not affected by the change in the location of the apex as shown in Table 4.4. However, it was found that a lower apex leads to slightly less power loss due to decreased viscous friction.

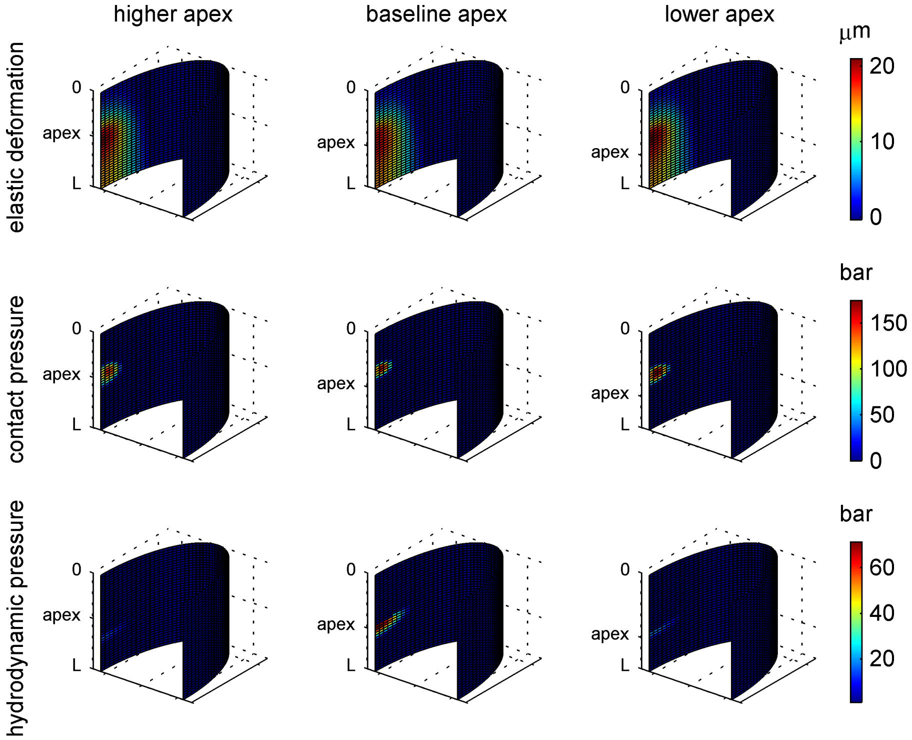

Figure 4.14 : Elastic deformation, contact and hydrodynamic pressures at 90°CA after FTDC for the change in apex location (partially-flooded inlet).

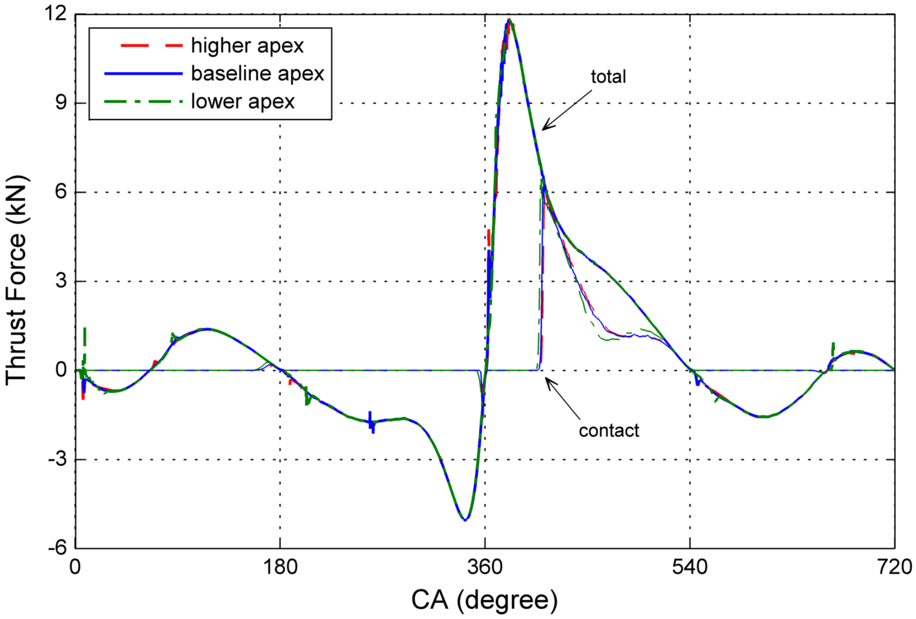

Figure 4.15 : Thrust force components for the change in apex location (partially-flooded inlet).

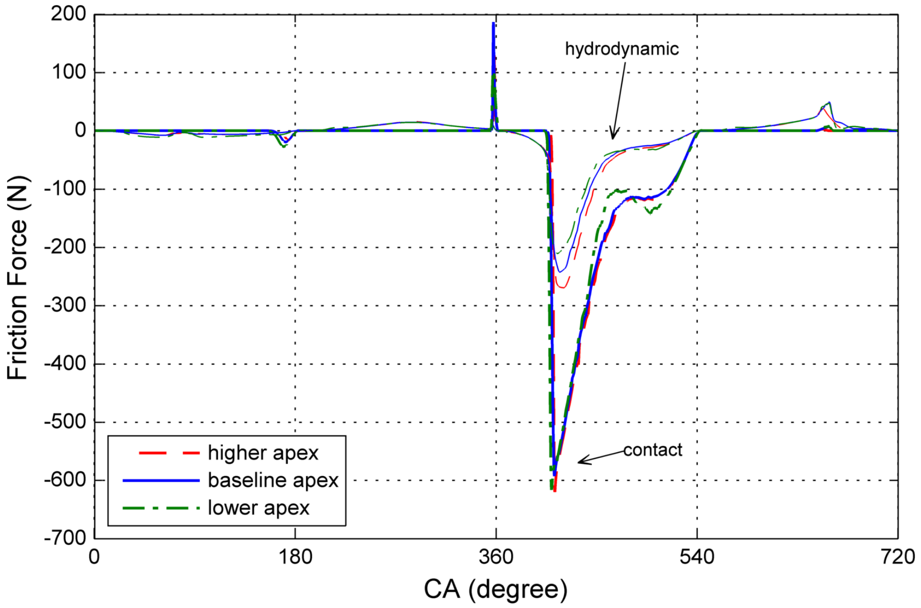

Figure 4.16 : Friction force for the change in apex location (partially-flooded inlet).

Table 4.4 : Indicated and friction mean effective pressures and ratios of friction power loss to indicated power for the change in apex location under partial load (partially-flooded inlet).

imep = 13.25 bar	viscous fmep	boundary fmep	total fmep	% power loss
higher apex location	0.115	0.196	0.311	2.35 %
baseline apex location	0.105	0.197	0.302	2.28 %
lower apex location	0.101	0.197	0.298	2.25 %

4.2.3 Effect of oval form

It can be seen in Figure 4.17 that lateral displacement and tilt were almost the same for three different ovality cases except for the slight shift during expansion stroke.

Minimum film thickness remained quite unchanged as well (Figure 4.18) when the side that the piston is resting on is considered. Differences are seen at the minor thrust side especially in the expansion stroke. This difference is mostly due to the degree of elastic deformation on the major thrust side. When ovality increases, higher local pressures develop in a smaller area on the piston skirt, as shown in Figure 4.19.

Despite similar secondary motion, lubrication characteristics showed a significant difference. In the second half of expansion stroke, starting from 400°CA, more of the lateral force was carried by surface asperities when the radius of curvature decreased (Figure 4.20). As a result, boundary friction was observed to decrease for the reduced

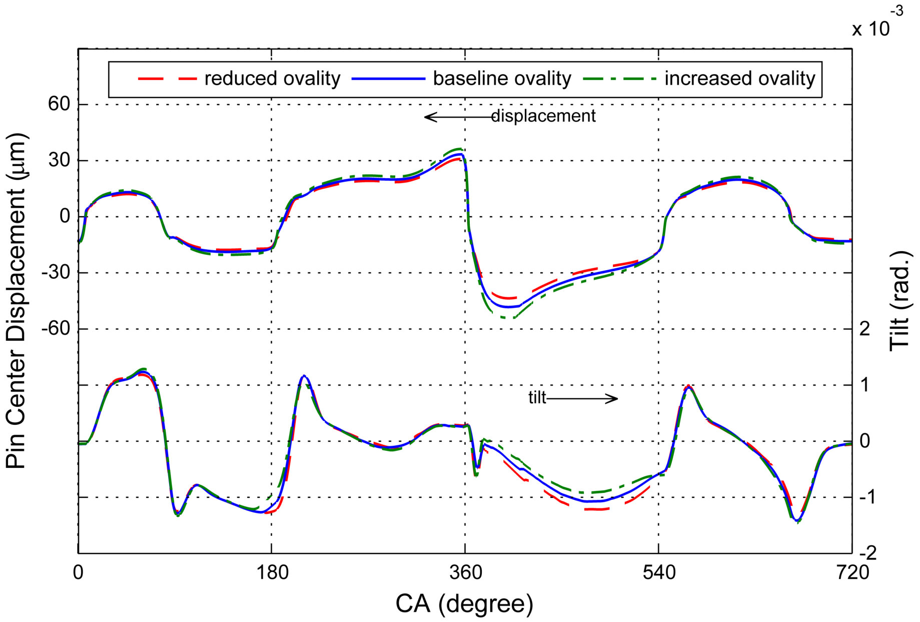

Figure 4.17 : Pin center displacement and tilt for the change in oval form (partially-flooded inlet).

oval form in the expansion stroke (Figure 4.21). A slight decrease in viscous friction was also observed giving way to a significantly lower power loss (Table 4.5). It can be said that oval form highly affects frictional loss arising from piston skirt in the case of partial lubrication and under specified partial load conditions.

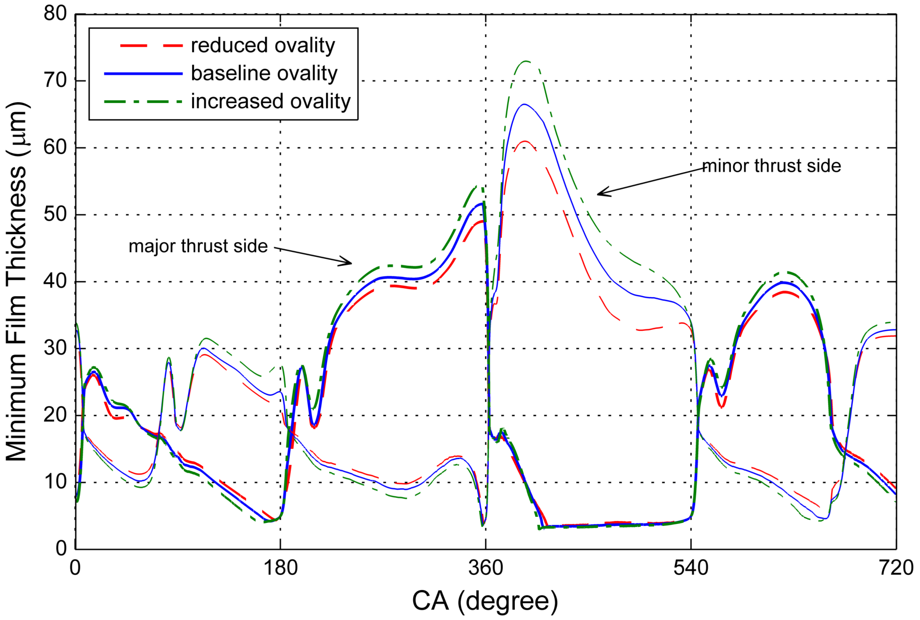

Figure 4.18 : Minimum film thickness variation for the change in oval form (partially-flooded inlet).

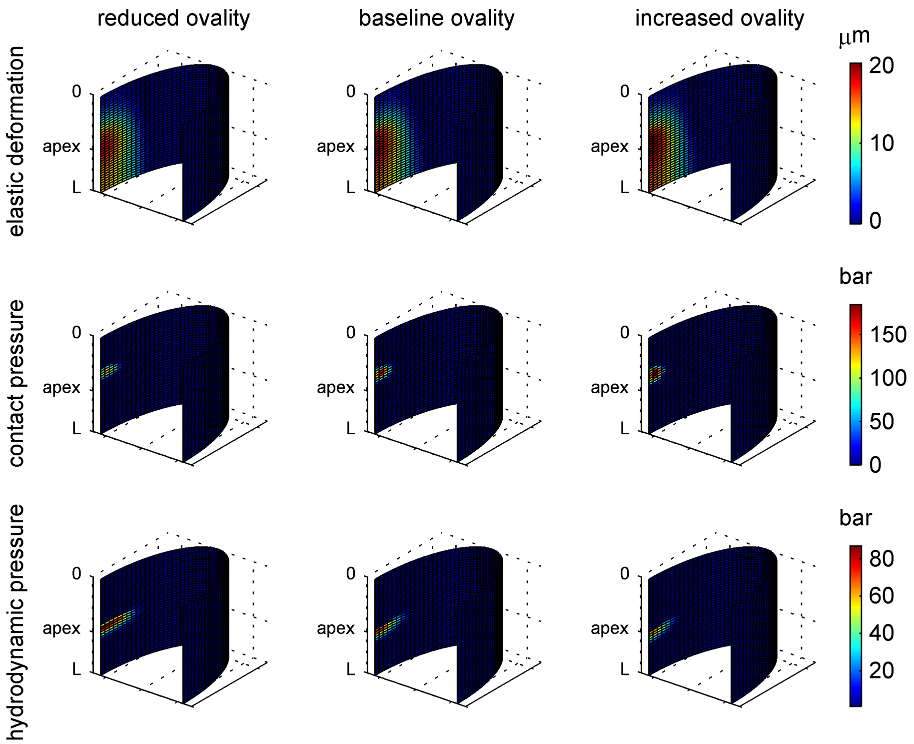

Figure 4.19 : Elastic deformation, contact and hydrodynamic pressures at 90°CA after FTDC for the change in oval form (partially-flooded inlet).

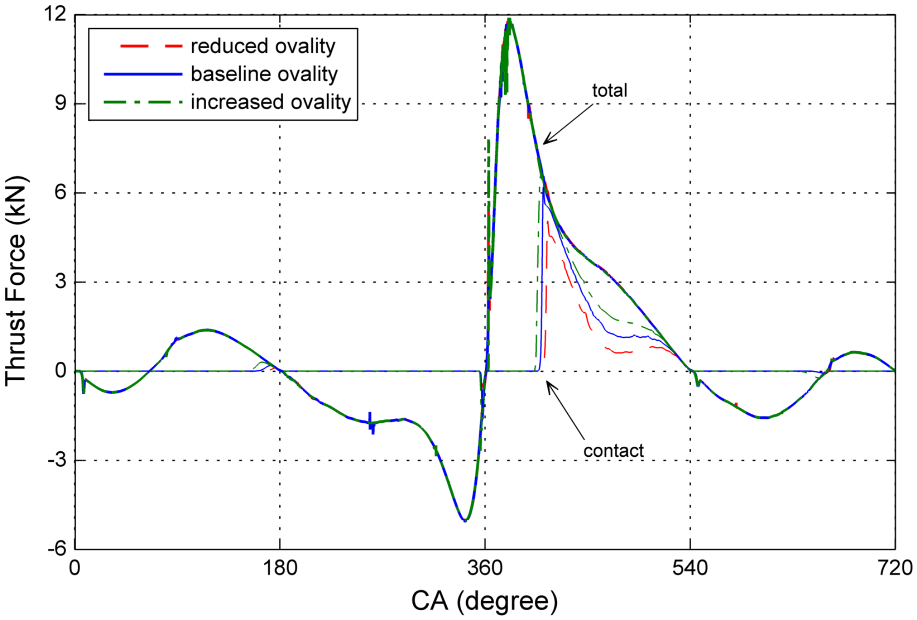

Figure 4.20 : Thrust force components for the change in oval form (partially-flooded inlet).

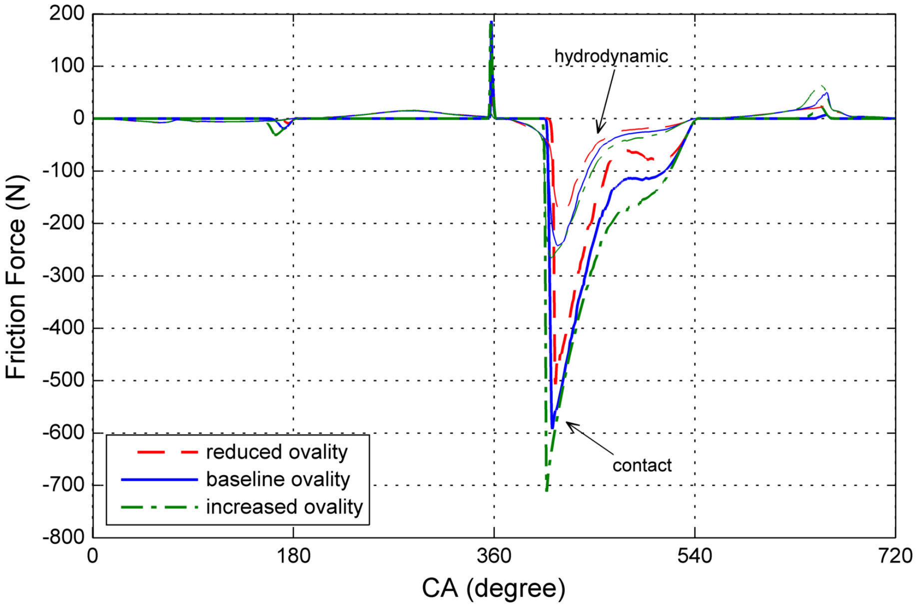

Figure 4.21 : Friction force for the change in oval form (partially-flooded inlet).

Table 4.5 : Indicated and friction mean effective pressures and ratios of friction power loss to indicated power for the change in oval form under partial load (partially-flooded inlet).

imep = 13.25 bar	viscous fmep	boundary fmep	total fmep	% power loss
reduced oval form	0.083	0.140	0.222	1.68 %
baseline oval form	0.105	0.197	0.302	2.28 %
increased oval form	0.125	0.246	0.371	2.80 %

4.2.4 Effect of viscosity

Three different oil grades other than the baseline SAE15W-40 oil were used to investigate the effect of oil viscosity. Viscosity values of these oils are given in Table 4.2 at 100°C operating temperature.

Piston motion showed slight changes with changing lubricant viscosity (Figure 4.22). At the expansion stroke, tilt was found to lessen as the viscosity reduces. However, minimum film thicknesses were less for low viscosity when only hydrodynamic lubrication was observed (Figure 4.23). As soon as solid contact starts minimum film thicknesses were the same.

When hydrodynamic thrust was insufficient to cushion the piston skirt at the expansion stroke, solid contact was more dominant for lower viscosities (Figure 4.24). This was expected since thicker oil tends to carry more pressure.

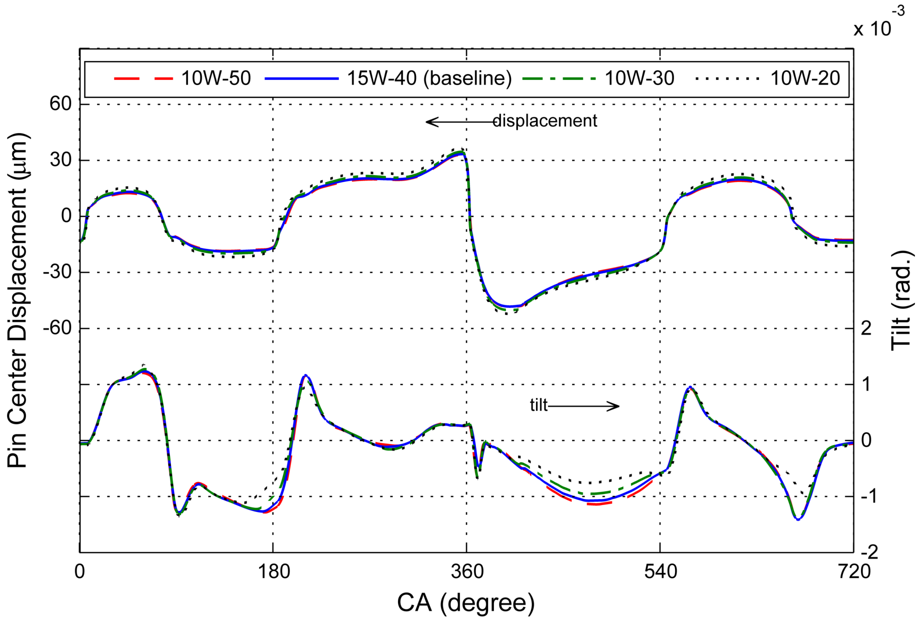

Figure 4.22 : Pin center displacement and tilt for the change in lubricant viscosity (partially-flooded inlet).

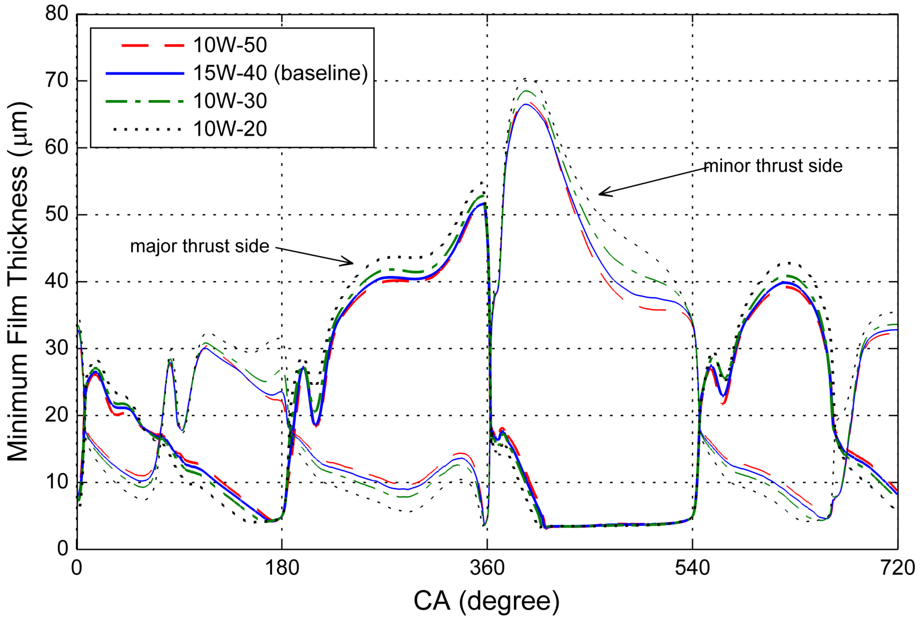

Figure 4.23 : Minimum film thickness variation for the change in lubricant viscosity (partially-flooded inlet).

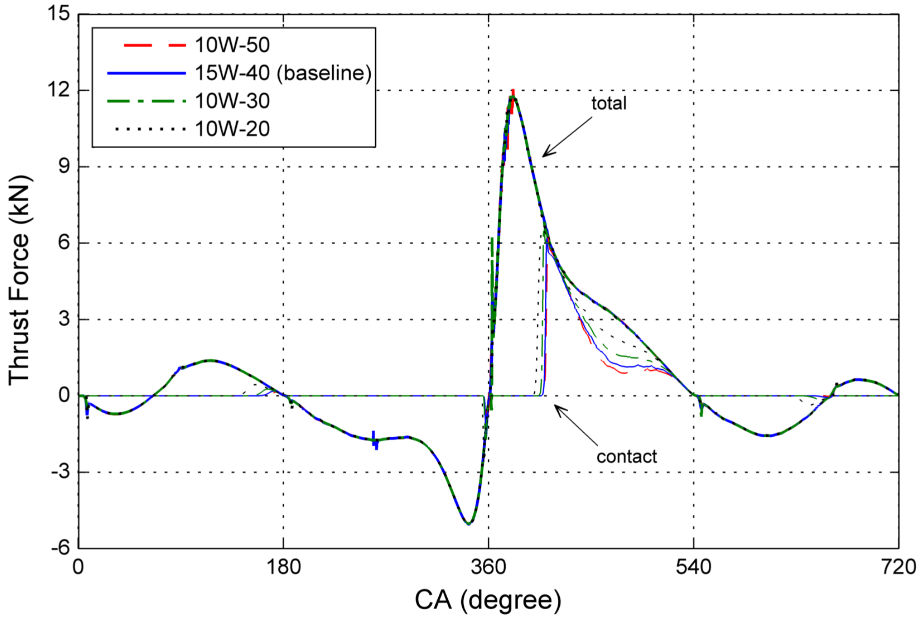

Figure 4.24 : Thrust force components for the change in lubricant viscosity (partially-flooded inlet).

The effect of viscosity was best seen in friction force acting on the skirt. Higher viscosity oil caused more hydrodynamic lubrication, but less solid contact (Figure 4.25). This result can be seen better in Figure 4.26 and Table 4.6. SAE10W-50 oil experienced lower viscous and higher boundary friction, however approximately the same power loss in total compared to baseline SAE15W-40. When SAE10W-30 and SAE10W-20 oils which have lower viscosities are used, total power loss was observed to increase.

Table 4.6 : Indicated and friction mean effective pressures and ratios of friction power loss to indicated power for the change in lubricant viscosity under partial load (partially-flooded inlet).

imep = 13.25 bar	viscous fmep	boundary fmep	total fmep	% power loss
10W-50	0.118	0.183	0.301	2.28 %
15W-40 (baseline)	0.105	0.197	0.302	2.28 %
10W-30	0.103	0.229	0.332	2.51 %
10W-20	0.082	0.276	0.359	2.71 %

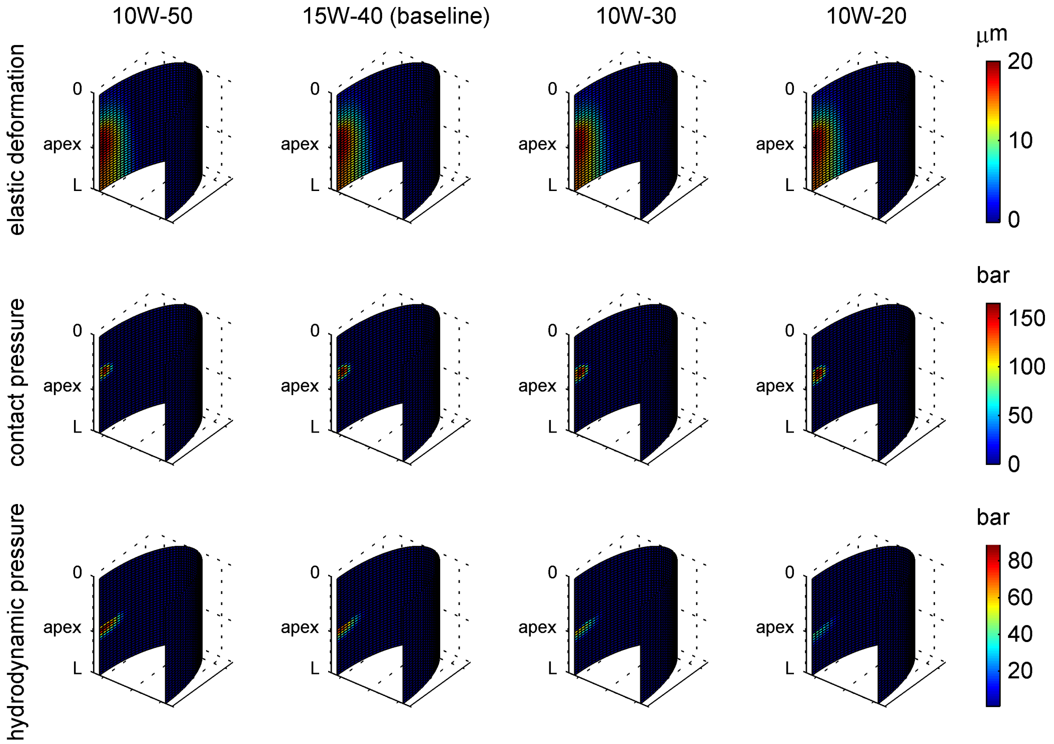

Figure 4.25 : Elastic deformation, contact and hydrodynamic pressures at 90°CA after FTDC for the change in lubricant viscosity (partially-flooded inlet).

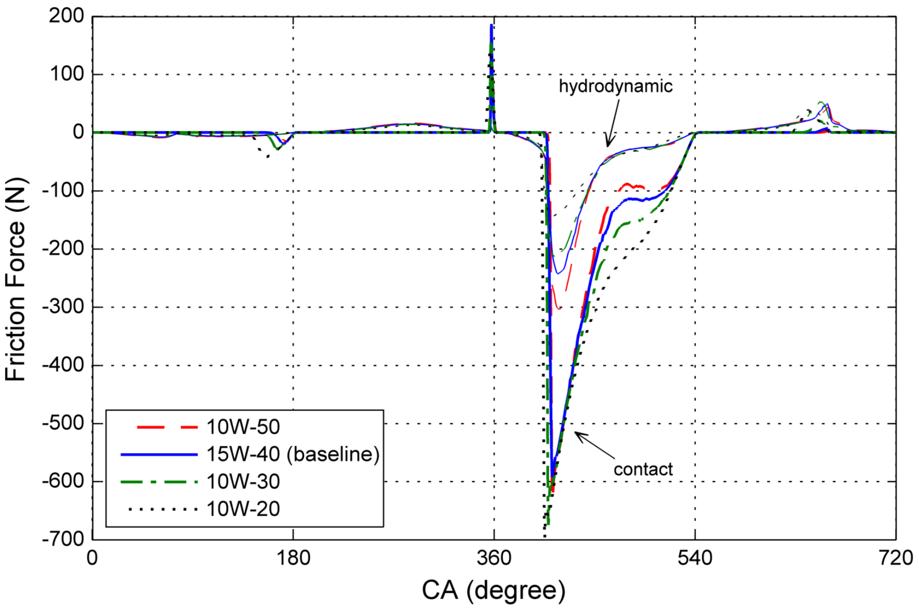

Figure 4.26 : Friction force for the change in lubricant viscosity (partially-flooded inlet).

4.2.5 Partially-flooded inlet overview

When the oil available in front of the skirt was 20 μm which is four times the wave height of the surface, solid contact was found to be effective in skirt-liner interaction.

This was quite dominant in the second half of expansion stroke, after the skirt moves from the minor thrust side to the major. At about 400°CA, film thickness reduced to surface waviness height as a result of increased combustion chamber pressure and high lateral velocity.

Baseline engine was calculated to lose 2.28% of its indicated power to friction of piston skirt. As a result of case studies by modifying the focus parameters one at a time this power loss percentage was found to vary from 1.68% to 2.80%. Both of these values of minimum and maximum power loss was observed for the change in oval form of the skirt and effects of barrel form and lubricant viscosity were rather less. Therefore, it can be concluded that under partial load, at a medium engine speed, a significant benefit can be achieved by reducing the ovality of piston for the partially-flooded lubrication conditions.

The results obtained by comparing four different parameters were applied simultaneously in a case to find out the combined effect. A profile with increased barrel and reduced oval forms having the apex location lower than the baseline skirt was tested. Type of oil was not changed since low viscosities were found to have higher loss and high viscosity offered negligible benefit.

Figure 4.27 shows that suggested skirt was subjected to a more aggressive lateral motion. Minimum film thickness was generally decreased for the entire cycle when

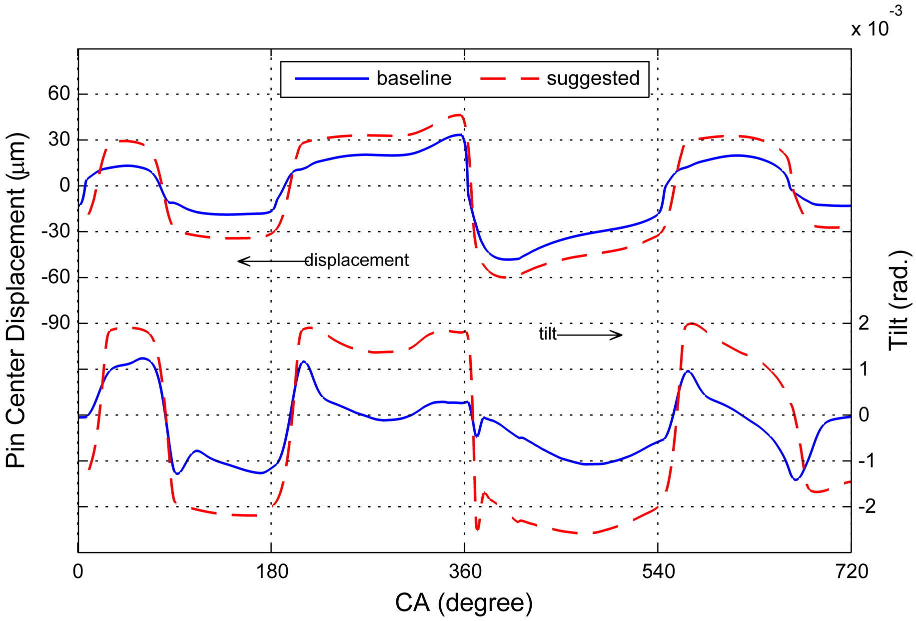

Figure 4.27 : Pin center displacement and tilt for the combined effect of barrel and oval forms and apex location (partially-flooded inlet).

the skirt profile changed (Figure 4.28). However, contact forces reduced due to higher elastic deformation as seen in Figure 4.29.

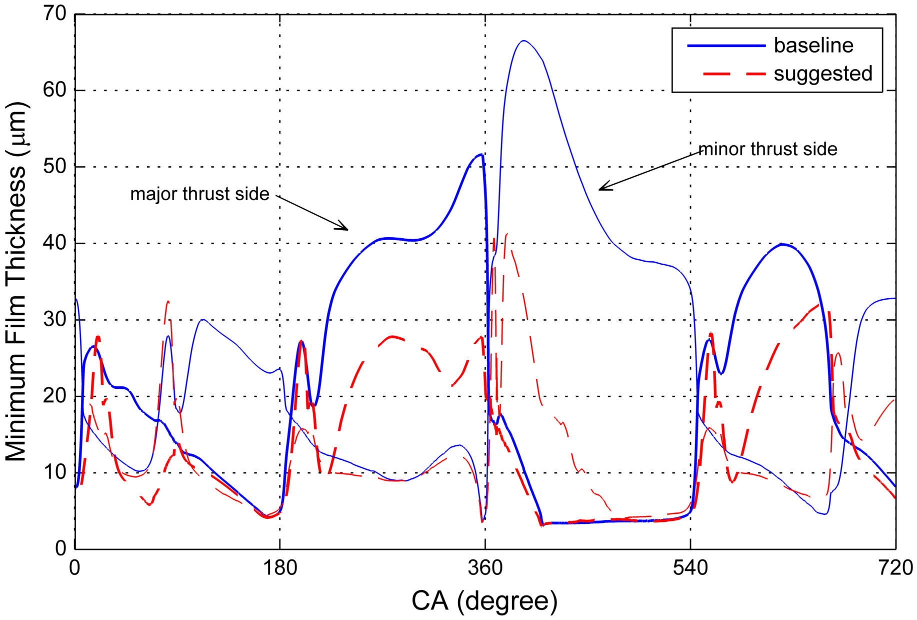

Figure 4.28 : Minimum film thickness variation for the combined effect of barrel and oval forms and apex location (partially-flooded inlet).

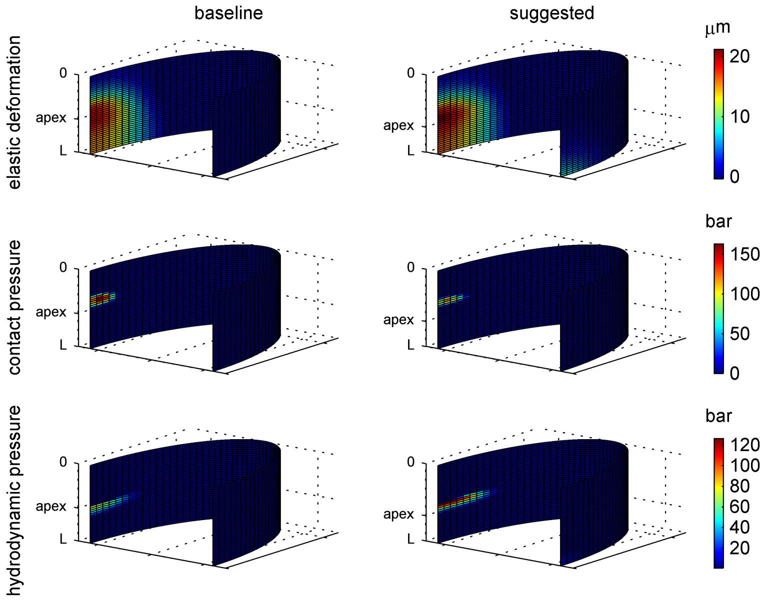

Figure 4.29 : Elastic deformation, contact and hydrodynamic pressures at 90°CA after FTDC for the combined effect of barrel and oval forms and apex location (partially-flooded inlet).

Figure 4.30 shows that contribution of solid contact to total thrust force was lower. As a result, lower contact friction was observed in the expansion stroke (Figure 4.31). Despite a slight increase in hydrodynamic friction at the late intake stroke, both viscous and boundary friction power loss decreased for the suggested skirt profile (Table 4.7).

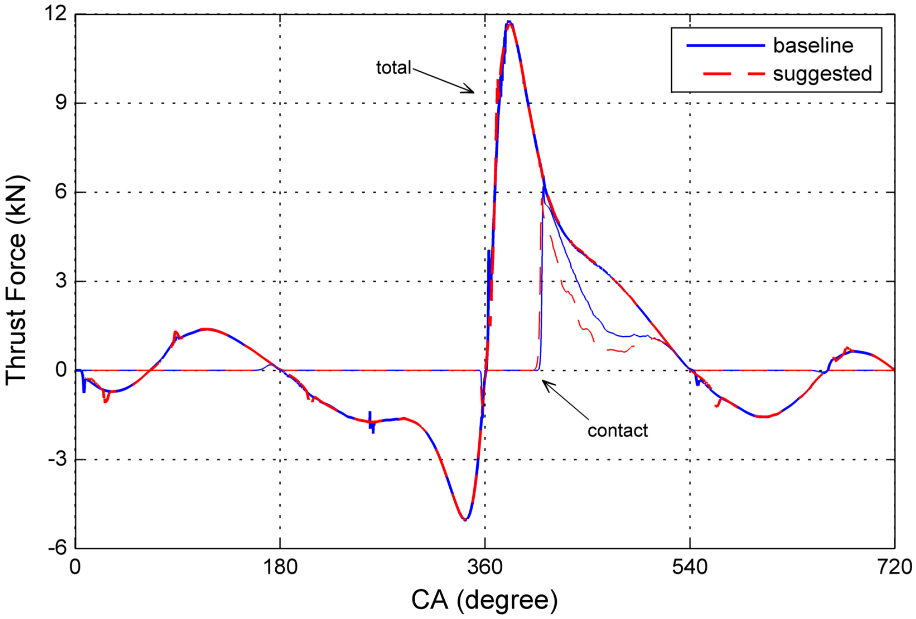

Figure 4.30 : Thrust force components for the combined effect of barrel and oval forms and apex location (partially-flooded inlet).

This decrease to 1.82%, however, was over the value for the reduced oval form case where only 1.68% of the indicated power was lost to skirt friction. Therefore, it can be concluded that effects of changes in skirt profile parameters is not linear for the partially-inlet condition under the given engine operation. A reduction in oval form alone can be more beneficial in terms of frictional power loss.

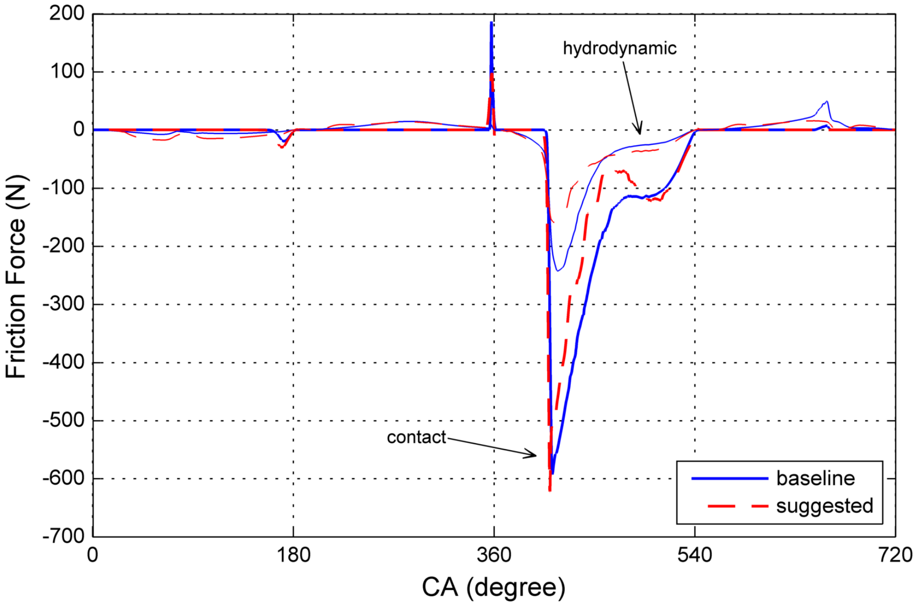

Figure 4.31 : Friction force for the combined effect of barrel and oval forms and apex location (partially-flooded inlet).

Table 4.7 : Indicated and friction mean effective pressures and ratios of friction power loss to indicated power for the combined effect of barrel and oval forms and apex location under partial load (partially-flooded inlet).

imep = 13.25 bar	viscous fmep	boundary fmep	total fmep	% power loss
baseline case	0.105	0.197	0.302	2.28 %
suggested case	0.091	0.151	0.241	1.82 %

4.3 Fully-Flooded Inlet Results

In the previous section, a number of cases were investigated in terms of frictional power loss arising from piston movement when solid contact was dominant especially in the expansion stroke. It was observed that skirt rested on wavy peaks during half of the stroke causing significant dry lubrication which can be considered as an unwanted operating condition. In order to prevent this, the amount of supply oil can be increased. It was expected to enhance hydrodynamic lubrication and therefore the same cases were analyzed with 40 μm oil thickness available on the liner surface at the leading edge of skirt.

4.3.1 Effect of barrel shape

It was found that effect of barrel form on piston motion was similar to those when the inlet was partially-flooded whereas the change in pin center displacement was more significant. Tilt slightly increased at the expansion stroke and changed direction at the compression stroke for the higher inlet oil supply. For the fully-flooded case, lateral displacement and tilt increased for the entire cycle when skirt was changed to a more aggressive barrel form (Figure 4.32).

Figure 4.33 shows that reduced barrel form had higher film thicknesses, instantaneously, on the side on which the skirt is resting whereas thickness was lower on the opposite side.

Contact forces were found to decrease, as expected, when compared to partially-flooded inlet condition. Comparison of barrel forms showed that reduced barrel form experienced less boundary thrust (Figure 4.34) whereas for lower supply

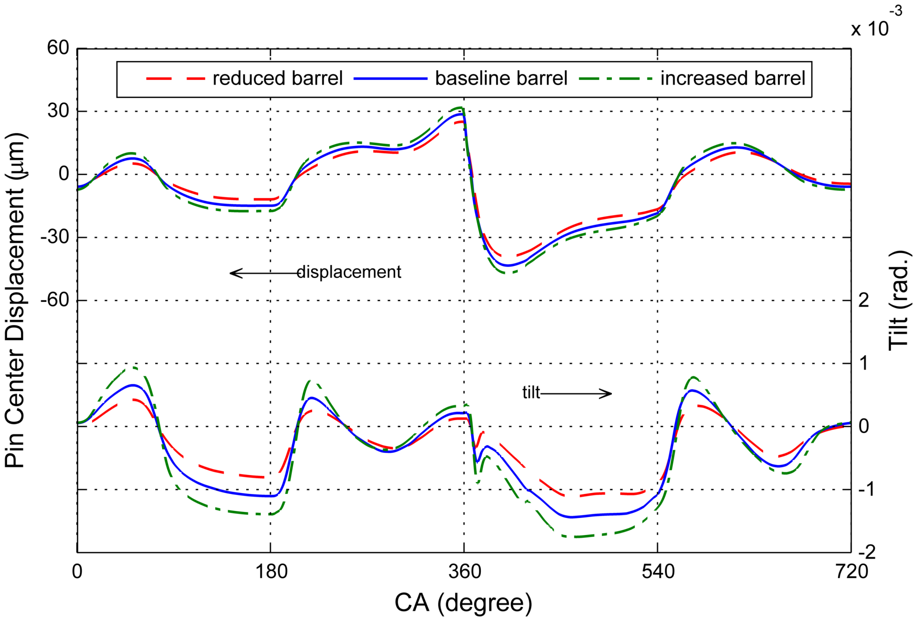

Figure 4.32 : Pin center displacement and tilt for the change in barrel form (fully-flooded inlet).

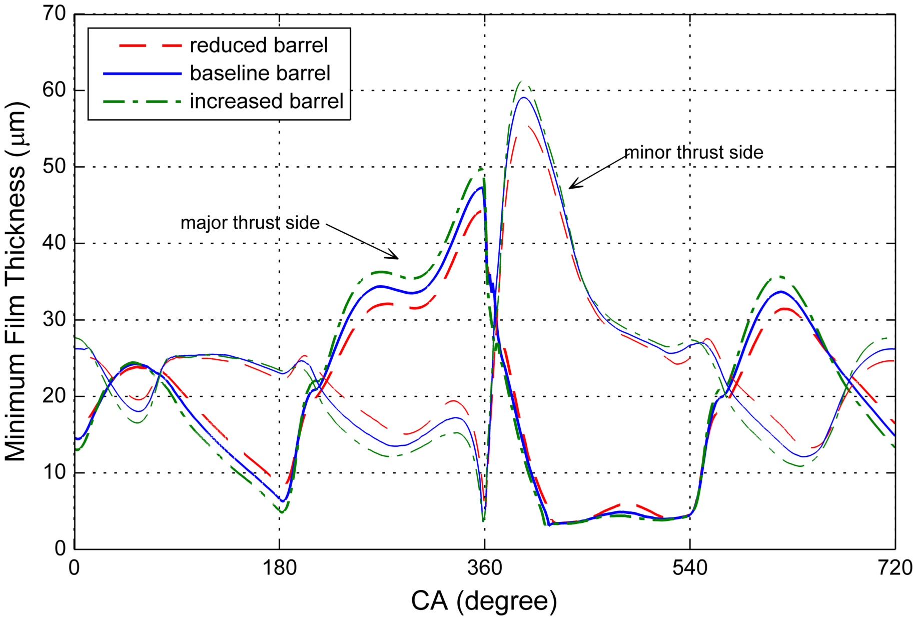

Figure 4.33 : Minimum film thickness variation for the change in barrel form (fully-flooded inlet).

oil thickness it was quite close for all skirt shapes. This can also be seen in Figure 4.35 for the selected crankangle of 90°after the firing TDC.

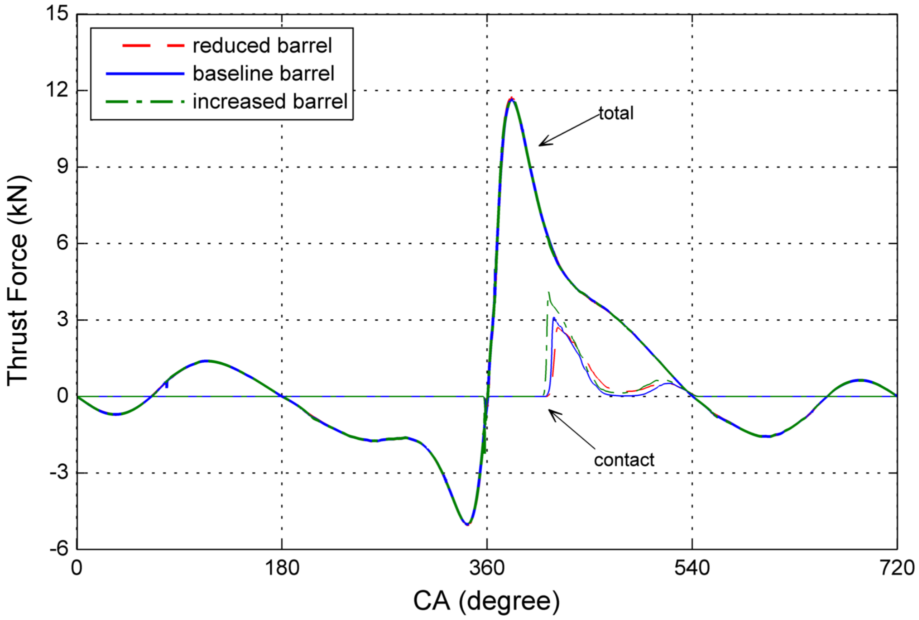

Figure 4.34 : Thrust force components for the change in barrel form (fully-flooded inlet).

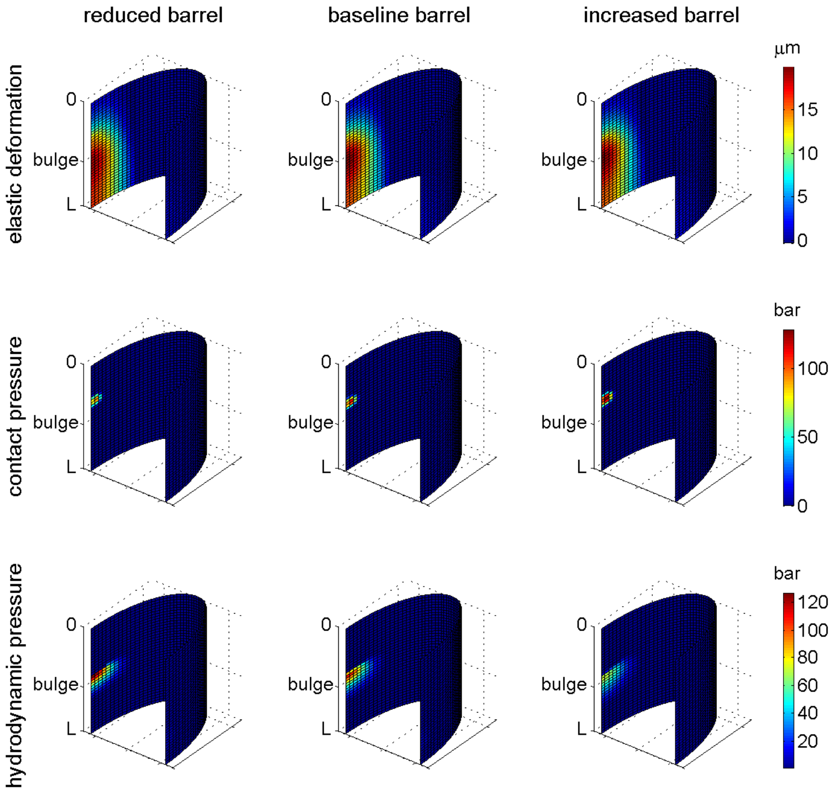

Figure 4.35 : Elastic deformation, contact and hydrodynamic pressures at 90°CA after FTDC for the change in barrel form (fully-flooded inlet).

Figure 4.36 shows that hydrodynamic friction force increased slightly when barrel form got closer to a perfect cylindrical shape whereas significant reduction in boundary friction was observed especially in the late expansion stroke. Table 4.8 reveals that viscous friction losses are approximately the same, however total frictional loss decreased with the effect of boundary friction as barrel aggressiveness reduces. This table also makes it possible to compare the effect of supply oil thickness, such that with a fully-flooded inlet, skirt friction can be reduced more than 50% for the baseline engine.

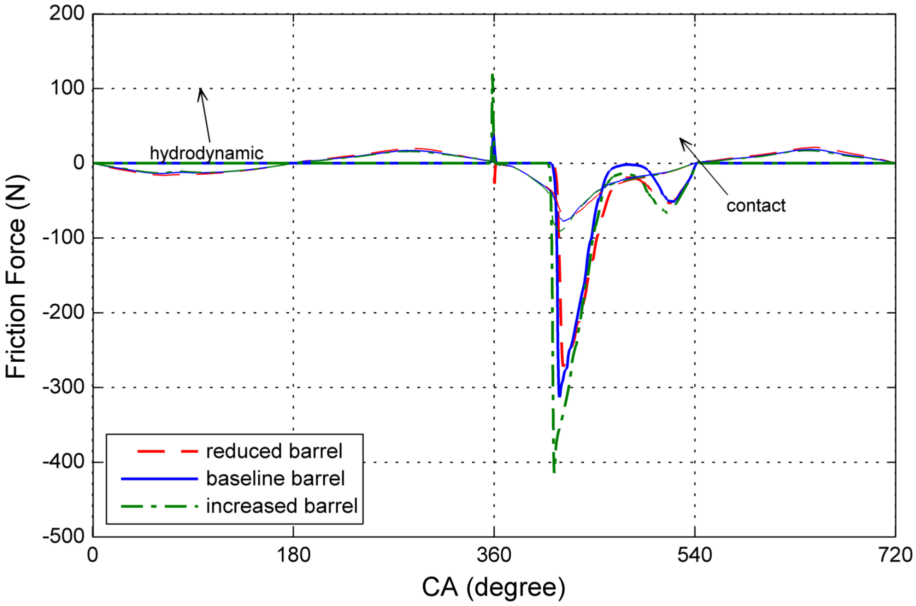

Figure 4.36 : Friction force for the change in barrel form (fully-flooded inlet).

Table 4.8 : Indicated and friction mean effective pressures and ratios of friction power loss to indicated power for the change in barrel form under partial load (fully-flooded inlet).

imep = 13.25 bar	viscous fmep	boundary fmep	total fmep	% power loss
reduced barrel form	0.071	0.049	0.120	0.91 %
baseline barrel form	0.069	0.074	0.143	1.08 %
increased barrel form	0.069	0.097	0.166	1.25 %

4.3.2 Effect of apex location

Piston skirt which has a lower apex was found to make a more aggressive tilting motion, as in the case of partially-flooded inlet and the change in lateral motion was more significant (Figure 4.37). Higher apex location can be said to result in a more stable angular motion staying closer to cylinder axis especially at the expansion stroke.

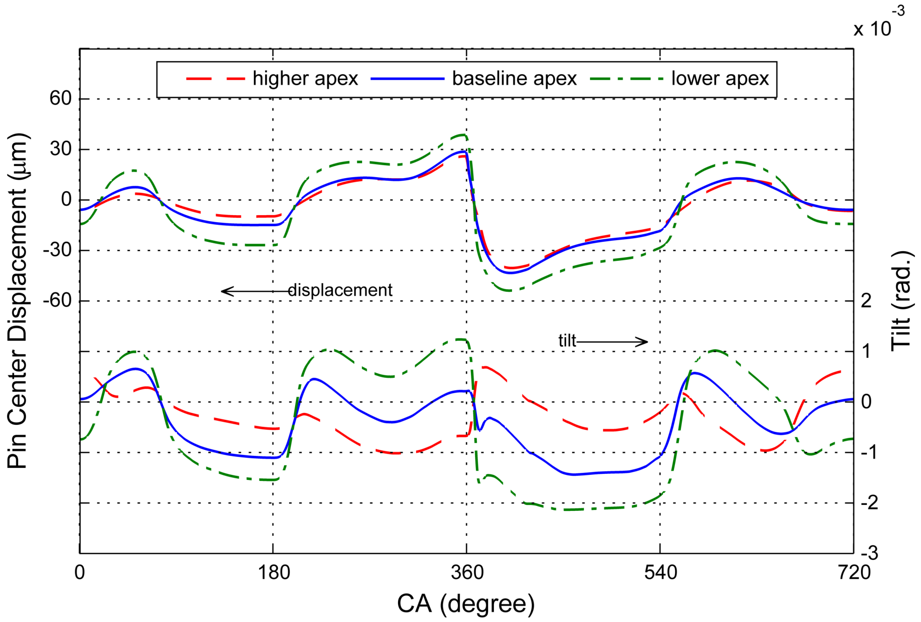

Figure 4.37 : Pin center displacement and tilt for the change in apex location (fully-flooded inlet).

Although lateral displacement and tilting motion looked simple, combined effect of these two, together with elastic deformations, gave a complicated minimum film thickness variation. Figure 4.38 shows that lower apex location leads to lower minimum film thickness values generally. Furthermore, profile with the lower apex

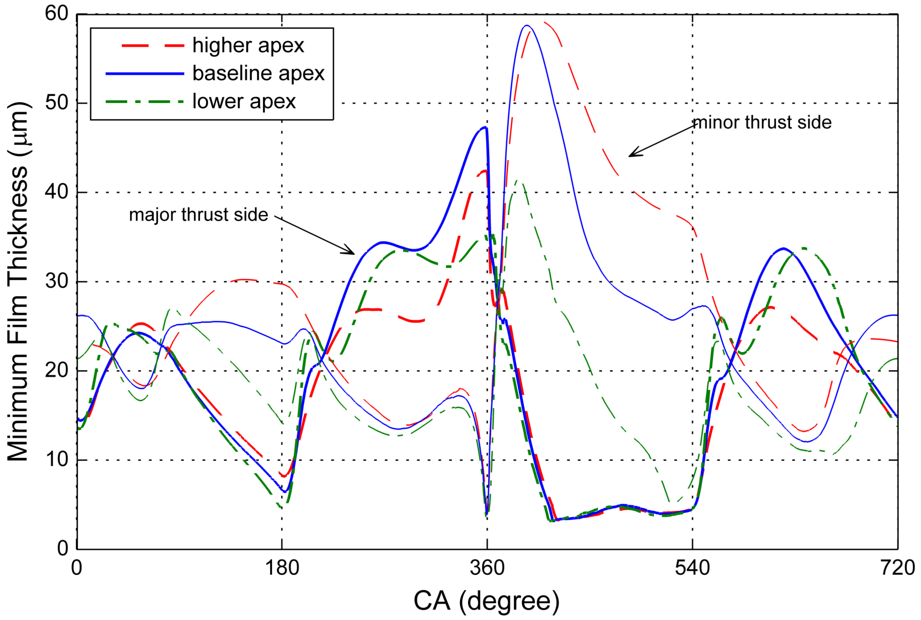

Figure 4.38 : Minimum film thickness variation for the change in apex location (fully-flooded inlet).

location always stayed under 40 μm on both sides, meaning that both sides of skirt was in contact with oil for the entire cycle. This is important because when the piston tends to move to one side and opposed by the cylinder wall, it is expected that force that has to be generated on this side increases due to additional pressure created by lubricant interaction on the other side. Piston is pushed with an extra force adding up to the one acted by the wrist-pin. This can be considered as a result of excess tilting motion. Although this is the case, higher apex generated more contact thrust in the expansion stroke as seen in Figures 4.39 and 4.40. Both hydrodynamic and contact friction were found to be less for lower apex location until the middle of the expansion stroke as seen in Figure 4.41. Only at the end of expansion, they were seen to rise which can be considered as the effect of boundary contact at the minor thrust side when the film thickness reduces to critical values close to surface waviness height. This increase towards the end of the stroke occurs in relatively low piston velocities. Therefore, overall boundary friction loss was found to be less for the lower apex whereas the viscous friction loss remained almost the same for three skirt profiles (Table 4.9).

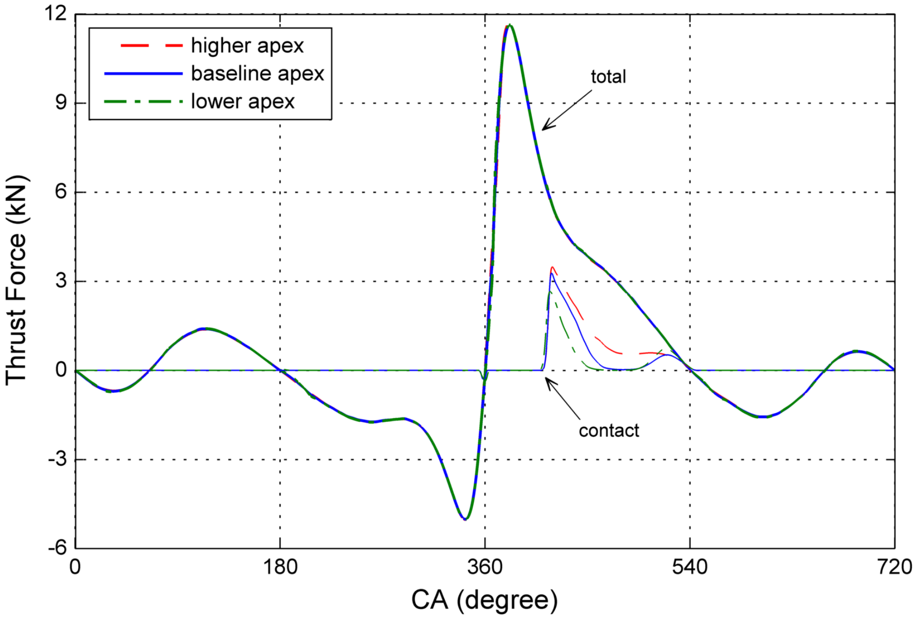

Figure 4.39 : Thrust force components for the change in apex location (fully-flooded inlet).

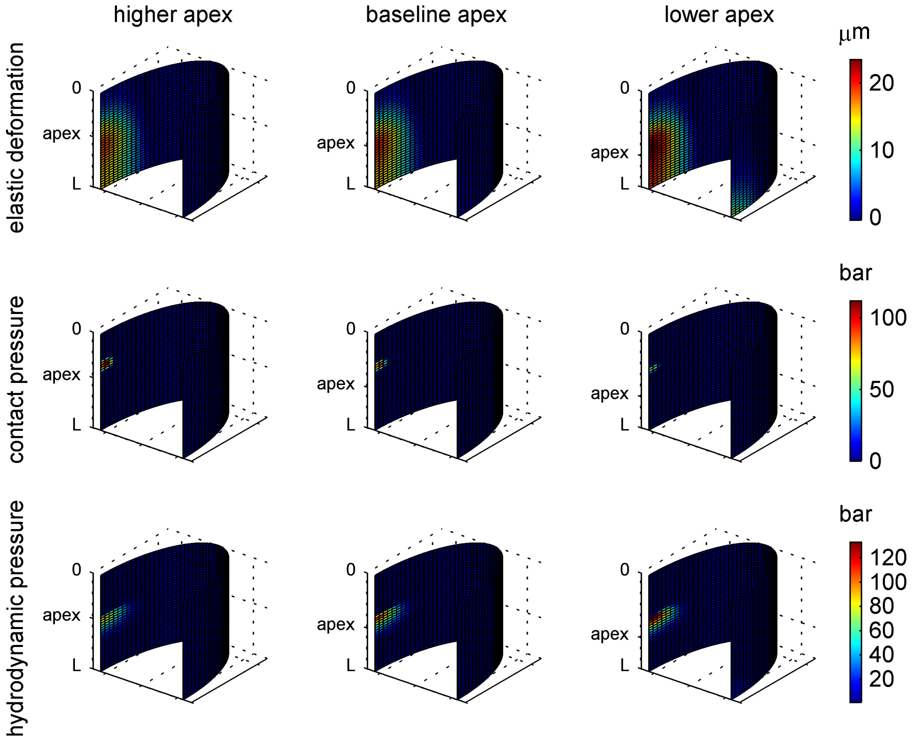

Figure 4.40 : Elastic deformation, contact and hydrodynamic pressures at 90°CA after FTDC for the change in apex location (fully-flooded inlet).

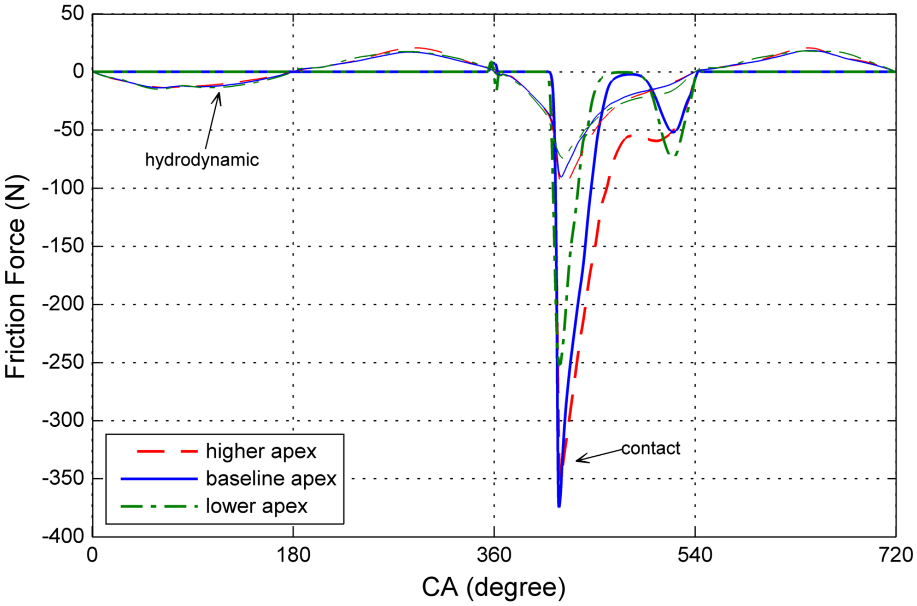

Figure 4.41 : Friction force for the change in apex location (fully-flooded inlet).

Table 4.9 : Indicated and friction mean effective pressures and ratios of friction power loss to indicated power for the change in apex location under partial load (fully-flooded inlet).

imep = 13.25 bar	viscous fmep	boundary fmep	total fmep	% power loss
higher apex location	0.077	0.107	0.184	1.39 %
baseline apex location	0.069	0.074	0.143	1.08 %
lower apex location	0.074	0.048	0.122	0.92 %

4.3.3 Effect of oval form

Figure 4.42 shows that lateral displacement and tilt were slightly affected by the change in oval form. Higher lateral and lower tilting motion were found to be significant for the increased ovality at the expansion stroke.

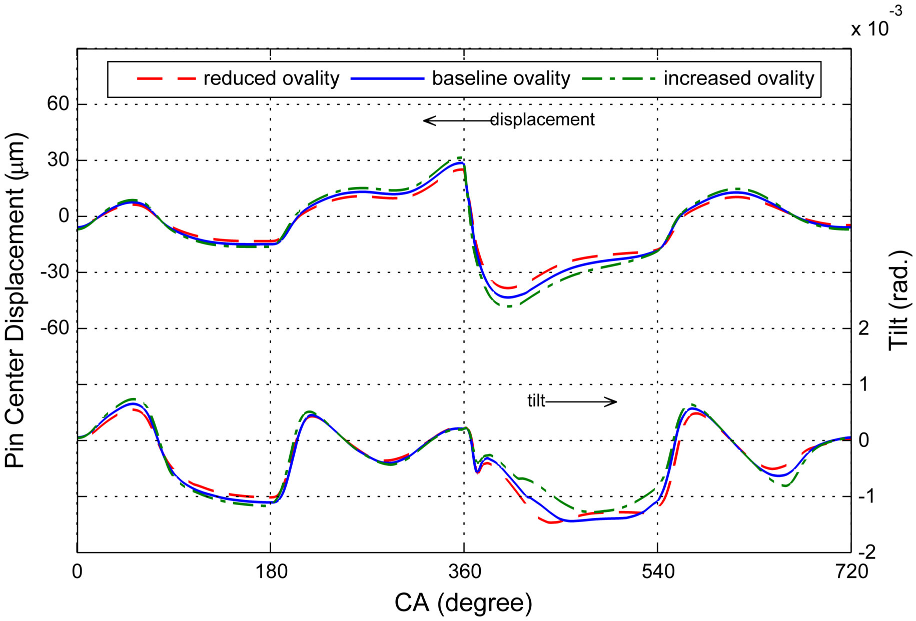

Figure 4.42 : Pin center displacement and tilt for the change in oval form (fully-flooded inlet).

Minimum film thickness were generally higher for reduced oval profile on the side that the piston is resting on (Figure 4.43). Significant increase was observed in the second half of the expansion stroke where wavy contact seemed to have ceased for some period. This could also be observed for thrust force composition in Figure 4.44 and contact pressures at 90°CA after FTDC in Figure 4.45. When the skirt is distorted more in terms of an oval shape, both contact and hydrodynamic components of friction force increased in the critical period at the expansion stroke (4.46). As a result higher power loss was found in terms of both viscous and boundary components (Table 4.10).

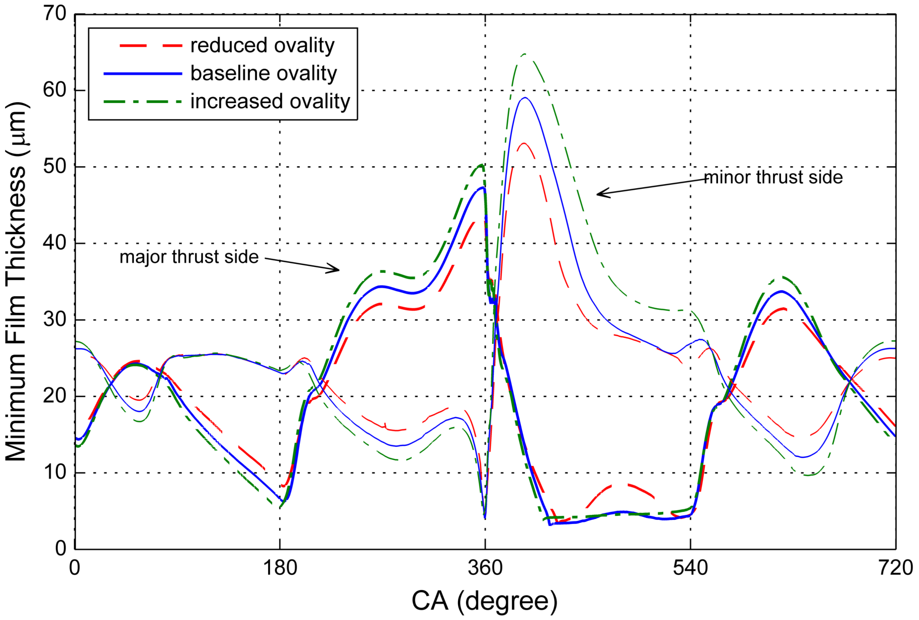

Figure 4.43 : Minimum film thickness variation for the change in oval form (fully-flooded inlet).

Although viscous friction loss was higher for reduced oval profile, it was found that significant reduction in boundary friction resulted in a considerable improvement in total loss.

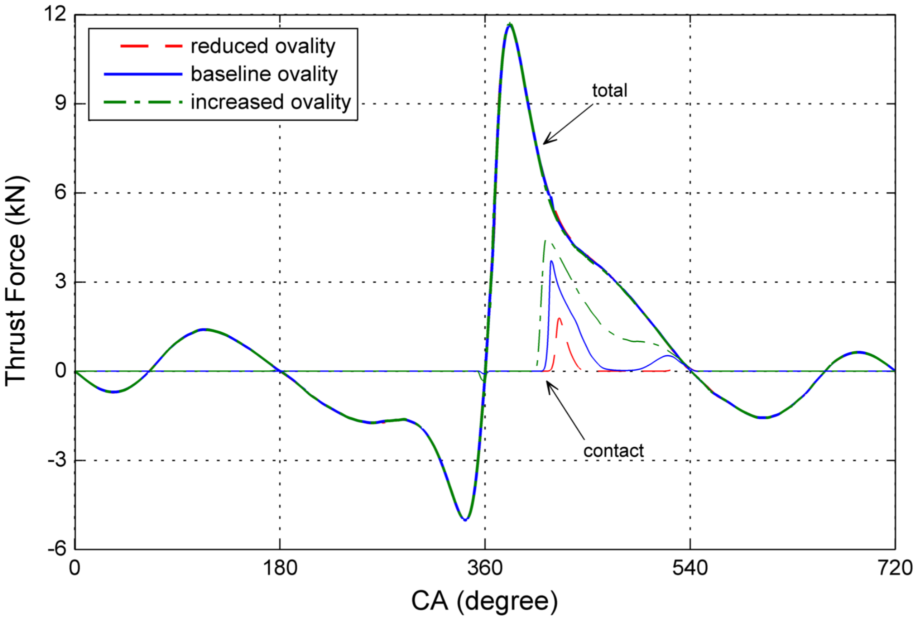

Figure 4.44 : Thrust force components for the change in oval form (fully-flooded inlet).

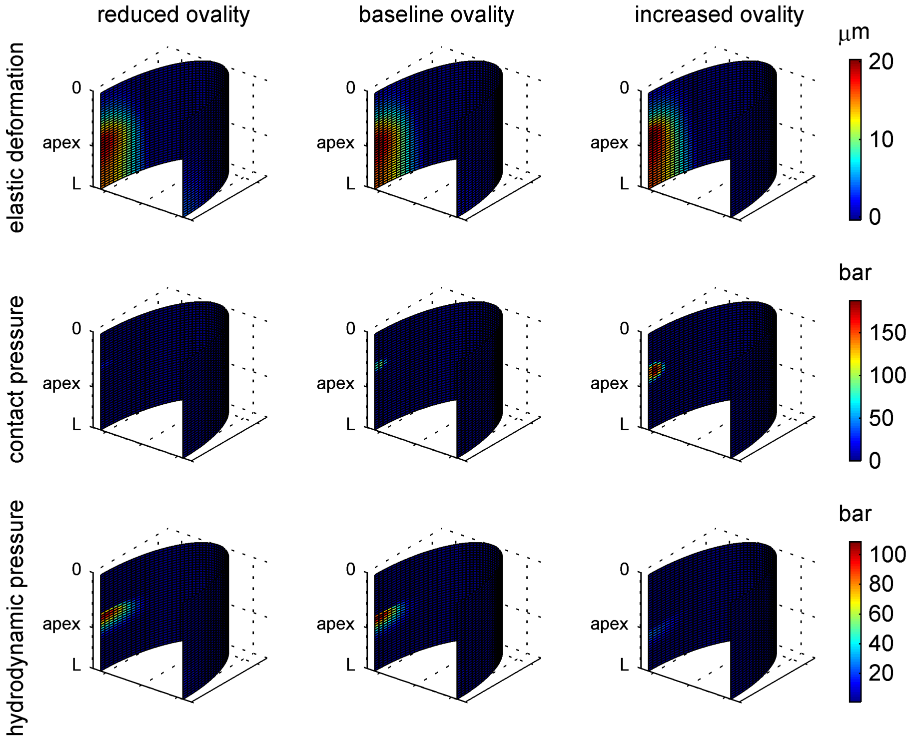

Figure 4.45 : Elastic deformation, contact and hydrodynamic pressures at 90°CA after FTDC for the change in oval form (fully-flooded inlet).

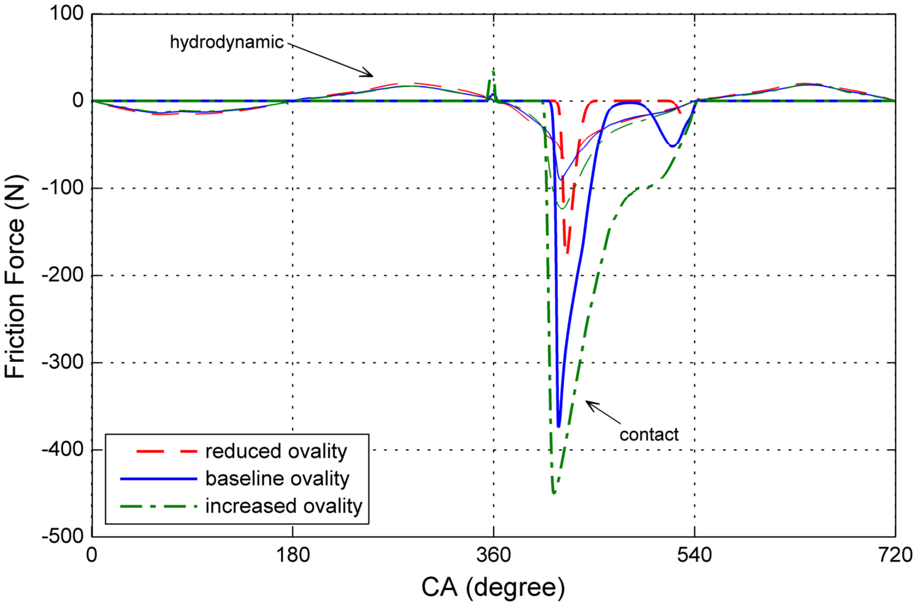

Figure 4.46 : Friction force for the change in oval form (fully-flooded inlet).

Table 4.10 : Indicated and friction mean effective pressures and ratios of friction power loss to indicated power for the change in oval form under partial load (fully-flooded inlet).

imep = 13.25 bar	viscous fmep	boundary fmep	total fmep	% power loss
reduced oval form	0.073	0.019	0.091	0.69 %
baseline oval form	0.069	0.074	0.143	1.08 %
increased oval form	0.083	0.173	0.256	1.93 %

4.3.4 Effect of viscosity

Effect of viscosity on piston motion can be said to be limited. Lateral displacement increased slightly as the viscosity decreased (Figure 4.47) and minimum film thickness was also lower (Figure 4.48). One significant difference was observed for the most viscous SAE10W-50 oil. Only this type of oil seemed to perform at higher oil film thickness, especially in the second half of the expansion stroke.

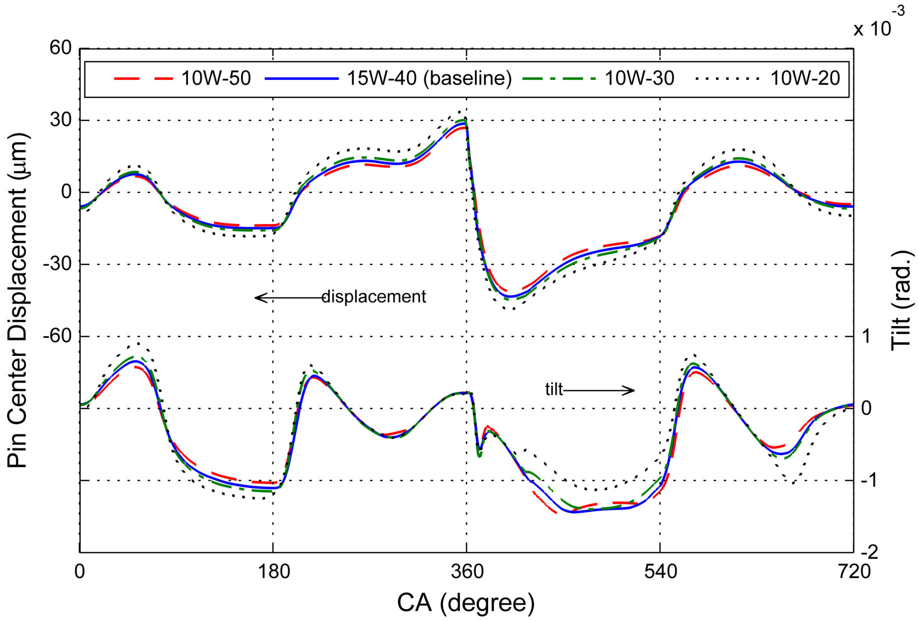

Figure 4.47 : Mass center displacement and tilt for the change in lubricant viscosity (fully-flooded inlet).

As a result of higher film thickness, SAE10W-50 oil could prevent solid contact over a longer period in the expansion stroke than baseline SAE15W-40 (Figure 4.49). This can be seen in Figure 4.50, as well, for the selected crankangle where the boundary contact is very small for the thicker oil. In spite of slightly higher hydrodynamic friction in intake, compression and exhaust strokes, SAE10W-50 performed significantly lower boundary friction in the expansion stroke as seen in

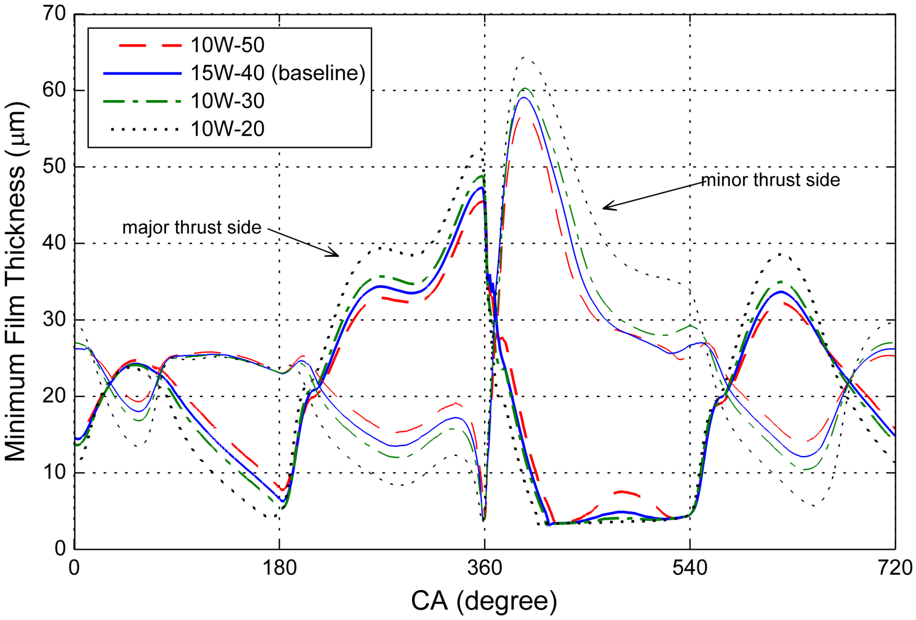

Figure 4.48 : Minimum film thickness variation for the change in lubricant viscosity (fully-flooded inlet).

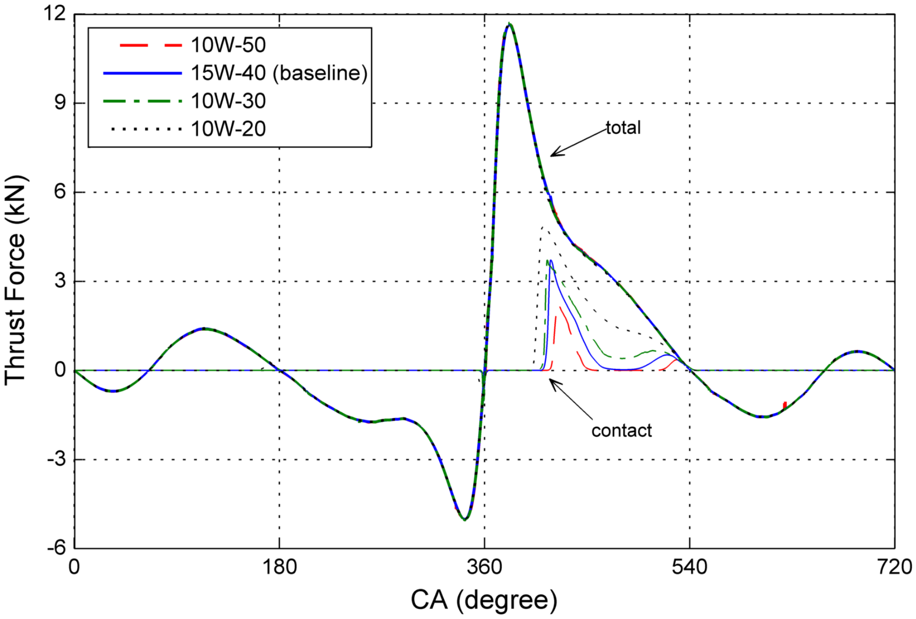

Figure 4.49 : Thrust force components for the change in lubricant viscosity (fully-flooded inlet).

Figure 4.51. For a comparatively small increase in viscous friction loss, high viscosity lubricant was observed to lead to a significant reduction in boundary friction loss as seen in Table 4.11. Opposed to the partially-flooded inlet condition, SAE10W-50 was observed to be beneficial when power loss due to skirt friction alone was considered for the investigated engine operating conditions.

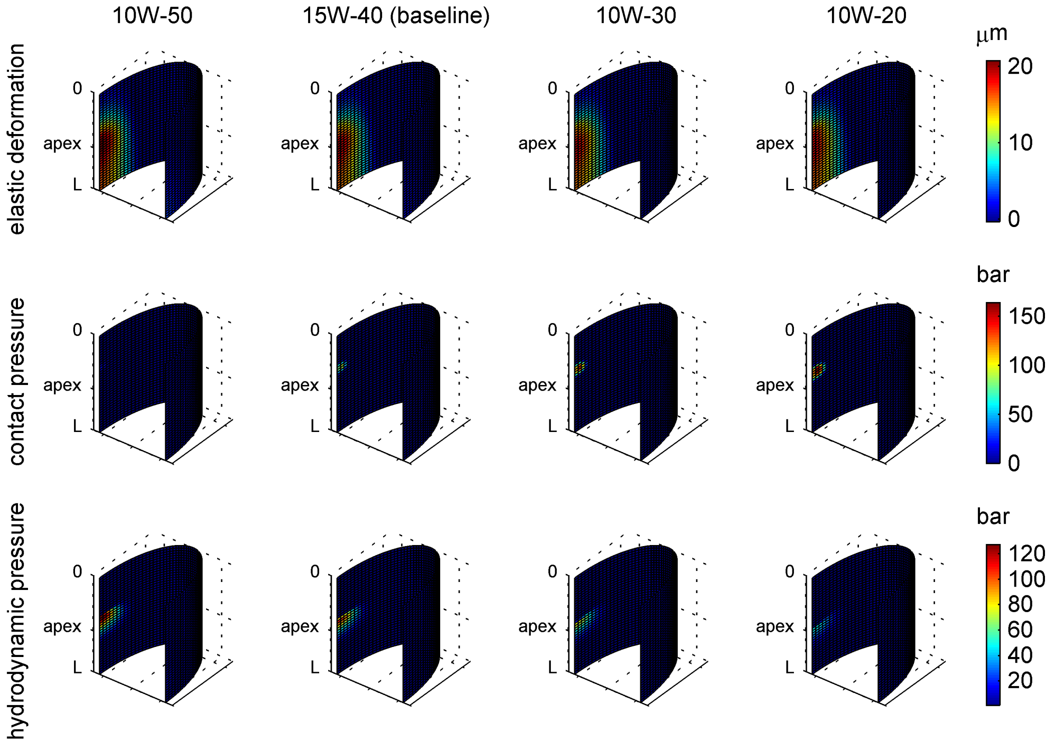

Figure 4.50 : Elastic deformation, contact and hydrodynamic pressures at 90°CA after FTDC for the change in lubricant viscosity (fully-flooded inlet).

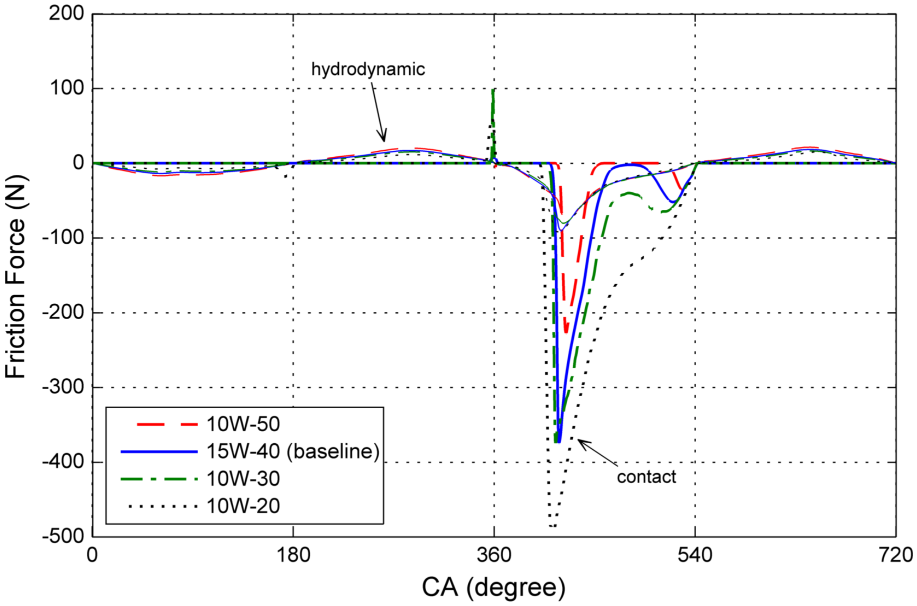

Figure 4.51 : Friction force for the change in lubricant viscosity (fully-flooded inlet).

Table 4.11 : Indicated and friction mean effective pressures and ratios of friction power loss to indicated power for the change in lubricant viscosity under partial load (fully-flooded inlet).

imep = 13.25 bar	viscous fmep	boundary fmep	total fmep	% power loss
10W-50	0.075	0.032	0.107	0.80 %
15W-40 (baseline)	0.069	0.074	0.143	1.08 %
10W-30	0.064	0.110	0.174	1.32 %
10W-20	0.058	0.199	0.257	1.94 %

4.3.5 Fully-flooded inlet overview

For the fully-flooded inlet condition, it was assumed that 40 μm oil was resting on the cylinder wall for the entire cycle. First of all, increasing the oil supply to the leading edge of skirt resulted in a reduction in frictional power loss from 2.28% to 1.08% for the baseline engine.

Among the four parameters, the effect of barrel form on friction was observed to have changed. A softer barrel generated slightly higher viscous, but significantly lower boundary friction in this case. Similar results were obtained when the barrel apex point was moved towards the bottom of the skirt and also when the ovality was reduced.

Effect of viscosity was dominant in fully-flooded inlet case. Thicker oil caused less contact friction decreasing the total loss.

A combination of these four parameters was used to generate a case for trial. The suggested case had a skirt with reduced oval and barrel forms having a lower apex and was run with more viscous SAE10W-50 oil.

Lateral displacement of piston for the suggested case was found to be less for most of the power cycle as seen in Figure 4.52. Tilt angle increased in the compression and expansion strokes. However it can be said that a less aggressive angular motion was observed. Figure 4.53 shows that, for the suggested profile and viscosity, skirt had higher film thicknesses on its side where it is instantaneously resting on for the entire cycle. The figure also indicates that the thickness was rarely close to 5 μm which was the height of surface waviness, giving signs of very little boundary contact.

This can be seen clearly in Figure 4.54 which shows that no contact occurred even in the expansion stroke. Figure 4.55 also shows that at the selected crankangle no solid

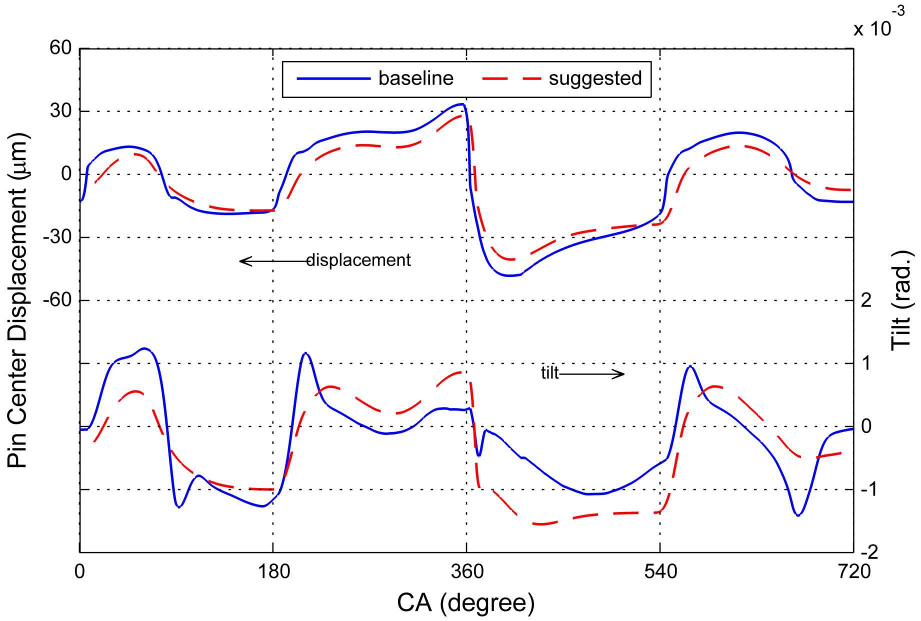

Figure 4.52 : Mass center displacement and tilt for the combined effect of barrel and oval forms, apex location and viscosity (fully-flooded inlet).

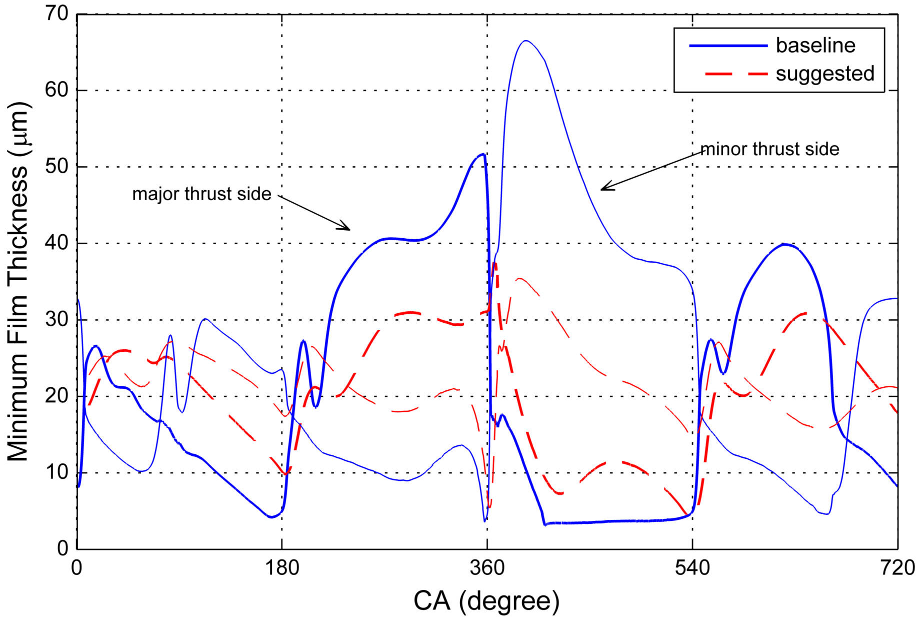

Figure 4.53 : Minimum film thickness variation for the combined effect of barrel and oval forms, apex location and viscosity (fully-flooded inlet).

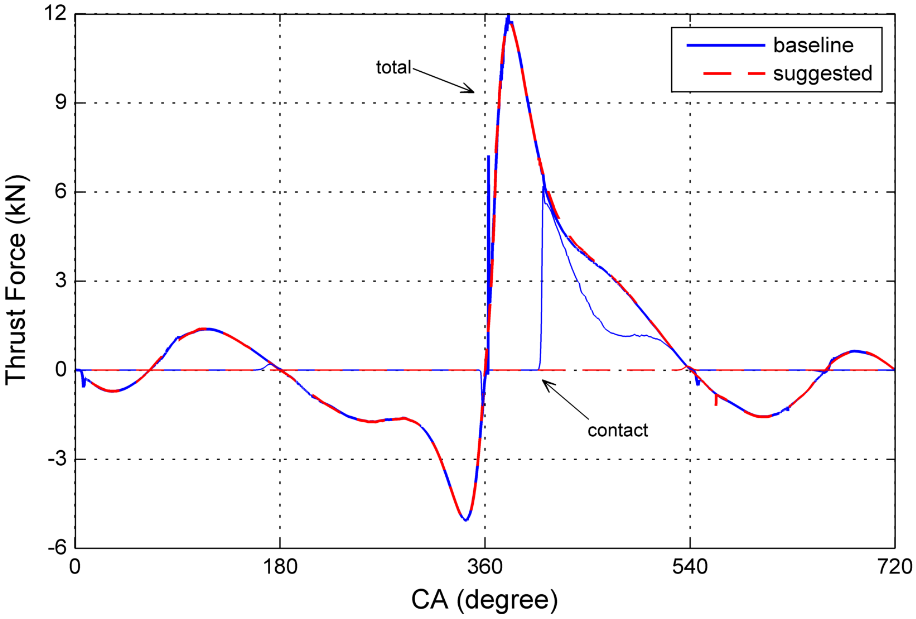

Figure 4.54 : Thrust force components for the combined effect of barrel and oval forms, apex location and viscosity (fully-flooded inlet).

contact occurred and lubricant pressures were lower. Therefore, boundary friction seemed to be prevented (Figure 4.56) with the modifications on skirt profile and viscosity. As a result of this, boundary frictional power loss were found to be negligibly small as given in Table 4.12. In addition, a decrease in viscous friction loss led to a reduced total loss of 0.67% of the indicated power under the investigated engine operating conditions.

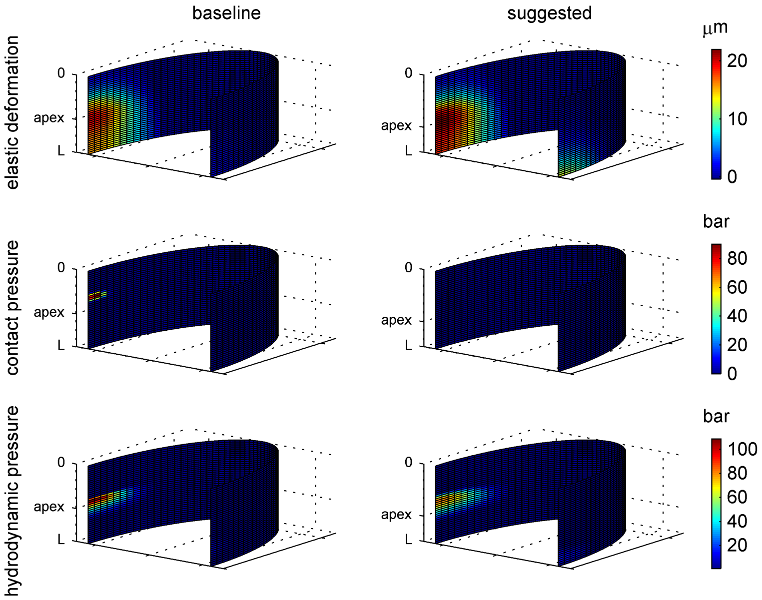

Figure 4.55 : Elastic deformation, contact and hydrodynamic pressures at 90°CA after FTDC for the combined effect of barrel and oval forms, apex location and viscosity (fully-flooded inlet).

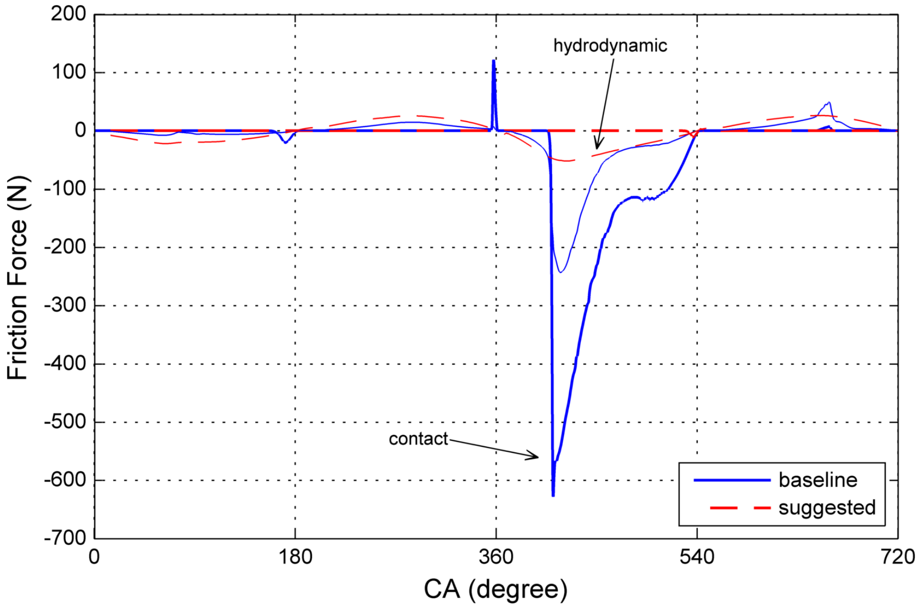

Figure 4.56 : Friction force for the combined effect of barrel and oval forms, apex location and viscosity (fully-flooded inlet).

Table 4.12 : Indicated and friction mean effective pressures and ratios of friction power loss to indicated power for the combined effect of barrel and oval forms, apex location and viscosity under partial load (fully-flooded inlet).

imep = 13.25 bar	viscous fmep	boundary fmep	total fmep	% power loss
baseline case	0.105	0.197	0.143	1.08 %
suggested case	0.089	0.0000258	0.089	0.67 %

5. CONCLUSIONS AND RECOMMENDATIONS

In this study, a mathematical model was constructed and a MATLAB code was written to investigate secondary motion of an ICE reciprocating piston and the friction caused by skirt-liner interaction. The model was capable of dealing with mixed lubrication. Reynolds Equation was solved to calculate hydrodynamic fluid pressure. It was modified with flow factors in order to account for the effects of surface asperities on two-dimensional flow of the lubricant between skirt and liner surfaces. The solution was obtained by finite differencing method. An asperity contact model for the interaction of two rough surfaces was incorporated into the model to add the contribution of solid contact to hydrodynamic load on piston skirt and to viscous friction. Fluid film rupture locations were also found through iteration assuming flow separation occurs at the outlet.

Following the lubrication solution, local pressures and tangential forces acting on the piston were found, elastic deformation of skirt under the effect of distributed normal force was solved and orientation of the piston with respect to the cylinder axis was calculated for each time step. The code was run for at least 6 power cycles to make sure that cyclic convergence has been reached.

Before the code was run, a stiffness matrix to be used in elastic deformation calculation was prepared through a finite element analysis by means of ANSYS software.

Calculations were run for a steady-state operation of a 6 cylinder, heavy-duty diesel engine. Therefore, for the selected running condition, a thermal analysis was made, also using ANSYS, to determine the change in skirt profile after its temperature rises to the steady-state operating values.

A tool was obtained to investigate the effects of several design parameters on piston secondary motion and friction acting on the skirt.

Case studies were carried out for partial load at a crank speed of 1680 rpm where four selected parameters were changed in order to compare the resulting skirt friction.

Partially-flooded case analyses were run first for low supply oil thickness. Later, it was increased to simulate fully-flooded inlet.

5.1 Conclusion

Partially-flooded inlet analysis were carried out with a 20 μm oil at the leading edge. For this condition:

- Barrel shape had a slight effect on skirt friction. A more aggressive barrel form resulted in a 2.2% reduction in power loss.
- When the apex location was moved down by 10% of total skirt length, angular motion of the skirt increased significantly. However, its effect on skirt friction was only 1.3% reduction.
- Very small change in piston lateral motion and minimum film thickness was observed for the change in oval form. However, skirt with a lower oval deviation was found to achieve 26.3% reduction in power loss.
- Lower viscosity oils increased skirt friction due to more solid contact especially in expansion stroke. More viscous SAE10W-50 oil could achieve a reduction in boundary friction together with a rise in viscous effects. In the overall, negligible change in total power loss was observed in comparison with baseline SAE15W-40 oil.
- In order to minimize power loss, more efficient results for individual parameters were combined. Viscosity effect was neglected, so a new profile with reduced oval and increased barrel form having a lower apex location was suggested. Although a 20.2% lower power loss was achieved, it was seen that the change in oval form alone would be more beneficial when compared to the suggested profile.
- In conclusion, under the specified engine running conditions with a partially-flooded inlet, this engine's piston could run more efficiently if the ovality of the skirt is lessened.

The same individual cases were also tested for a higher oil supply thickness. Fully-flooded inlet condition were assumed to be valid with 40 μm oil available on the liner surface. As a result:

- For the baseline configuration, frictional power loss resulting from skirt-liner interaction was found to decrease 52.6% when the amount of oil resting on the liner were increased.
- Barrel shape had a moderate effect on lateral motion. A reduced barrel form resulted in less solid contact at the expansion stroke and therefore, in a 15.7% reduction in power loss was observed to be achieved.
- The change in apex location was more effective than it was for partially-flooded inlet. 14.8% reduction was observed for 10% lower apex location despite the extra low film thicknesses on the minor thrust side through the end of expansion stroke.
- Change in piston lateral motion was rather limited as a result of the change in oval form. However, a considerable power loss reduction of 36.1% was achieved with ovality by preventing solid contact significantly in the mid-stroke during expansion.
- On the contrary to partially-flooded inlet, higher viscosity oil were found to decrease the power loss by 25.9% by reducing boundary friction especially in the middle of the expansion stroke.
- The test run for combined effect of parameters resulted to be a highly beneficial condition where approximately no solid contact was observed. Friction mean effective pressure was found to decrease by 38.0% compared to baseline skirt and lubricant viscosity. Therefore, the suggested profile, together with SAE10W-50 oil can be offered for a more efficient piston under the specified engine running conditions with a fully-flooded inlet.

5.2 Recommendations and Future Work

The aim of this study was to obtain a numerical tool to analyze the effects of different engine design parameters on the frictional performance of ICE piston skirt. The current model can calculate the lateral trajectory of the piston and resulting frictional behavior of the skirt for an entire power cycle.

The model is limited to skirt friction only. In order to investigate the frictional loss of power cylinder, rings and connecting rod bearings should also be taken into account. The outcome of this study has the potential to be a suitable platform to be developed with additions of modules for ring and bearing contributions.

There are many studies on ring dynamics which is capable of modeling lubrication and calculating friction loss ([8, 35, 36, 38, 39]). These studies generally assume that piston axis is always parallel to the cylinder axis. Integration of a ring lubrication solver to the current model can also make it possible to investigate the effect of tilt on ring performance due to the change in effective ring profile. In addition, friction force acting on the piston rings adds up to the axial load on the piston. The two models should be coupled for a more comprehensive tool.

The current piston secondary dynamics code can also be improved with the integration of alternative cavitation and surface asperity models as well as it can be a tool for testing new models for use in the friction prediction of ICE piston assembly.

REFERENCES

[1] **Patir, N. and Cheng, H.S.** (1979). Application of average flow model to lubrication between rough sliding surfaces, *Journal of Lubrication Technology - Transactions of The ASME*, *101*(2), 220–230.

[2] **Priest, M. and Taylor, C.M.** (2000). Automobile engine tribology, *Wear*, *241*, 193–203.

[3] **Holmberg, K.**, **Andersson, P. and Erdemir, A.** (2012). Global energy consumption due to friction in passenger cars, *Tribology International*, *47*, 221–234.

[4] **Shin, S.**, **Cusenza, A. and Shi, F.** (2004). Offset crankshaft effects on SI engine combustion and friction performance, *SAE Technical Paper*, *2004-01-0606*.

[5] **Yang, J.**, **Yang, W.**, **Yu, X. and Wang, C.** (2001). Design of internal combustion engine piston based on skirt lubrication analysis, *SAE Technical Paper*, *2001-01-2486*.

[6] **Teraguchi, S.**, **Suzuki, W.**, **Takiguchi, M. and Sato, D.** (2001). Effects of Lubricating Oil Supply on Reductions of Piston Slap Vibration and Piston Friction, *SAE Technical Paper*, *2001-01-0566*.

[7] **Sato, O.**, **Takiguchi, M.**, **Aihara, T.**, **Seki, Y.**, **Fujimura, K. and Tateishi, Y.** (2004). Improvement of piston lubrication in a Diesel engine by means of cylinder surface roughness, *SAE Technical Paper*, *2004-01-0604*.

[8] **Yu, B.**, **Sawicki, J.T. and Dunaevsky, V.** (1999). Analytical solution of piston ring pack lubrication for truck air brake compressor, *SAE Technical Paper*, *1999-01-3769*.

[9] **Priest, M.**, **Dowson, D. and Taylor, C.M.** (2000). Theoretical modelling of cavitation in piston ring lubrication, *Journal of Mechanical Engineering Science*, *214*, 435–447.

[10] **Gulwadi, S. and Shrimpling, G.** (2003). Analytical solution of piston ring pack lubrication for truck air brake compressor, *SAE Technical Paper*, *2003-01-0245*.

[11] **Patir, N. and Cheng, H.S.** (1978). An average flow model for determining effects of three-dimensional roughness on partial hydrodynamic lubrication, *Journal of Lubrication Technology - Transactions of The ASME*, *100*, 12–17.

[12] **Liao, Y.**, **Stephenson, D. and Ni, J.** (2010). A multifeature approach to tool wear estimation using 3D workpiece surface texture parameters, *ASME. J. Manuf. Sci. Eng.*, *132*(6).

[13] **Zhu, D.**, **Cheng, H.**, **Arai, T. and Hamai, K.** (1992). A numerical analysis for piston skirts in mixed lubrication — Part I: Basic modeling, *ASME. J. Tribol.*, *114*(3), 553–562.

[14] **Tsujiuchi, N.**, **Koizumi, T.**, **Hamada, K.**, **Okamura, M. and Tsukijima, H.** (2004). Optimization of profile for reduction of piston slap excitation, *SAE Technical Paper*, *2004-32-0022.*

[15] **Gerges, S.**, **De Luca, J. and Lalor, N.** (2002). The influence of cylinder lubrication on piston slap, *Journal of Sound and Vibration*, *257*(3), 527–557.

[16] **Mansouri, S.H. and Wong, V.W.** (2004). Effects of piston design parameters on piston secondary motion and skirt-liner friction, *SAE Technical Paper*, *2004-01-2911.*

[17] **Icoz, T. and Dursunkaya, Z.** (2005). Experimental investigation of oil accumulation in second land of internal combustion engines, *Journal of Engineering for Gas Turbines and Power*, *127*, 206–211.

[18] **Yilmaz, E.**, **Tian, T.**, **Wong, V.W. and Heywood, J.** (2004). The contribution of Different oil consumption sources to total oil consumption in a spark ignition engine, *SAE Technical Paper*, *2004-01-2909.*

[19] **Duyar, M.**, **D., B. and Perchanok, M.** (2005). A comprehensive piston skirt lubrication model using a mass conserving EHL algorithm, *SAE Technical Paper*, *2005-01-1640.*

[20] **Rogowski, A.** (1961). Method of Measuring the Instantaneous Friction of Piston Rings in a Firing Engine, *SAE Technical Paper*, *610263.*

[21] **Bishop, I.** (1964). Effect of Design Variables on Friction and Economy, *SAE Technical Paper*, *640807.*

[22] **Patton, K.**, **Nitschke, R. and Heywood, J.** (1989). Development and Evaluation of a Friction Model for Spark-Ignition Engines, *SAE Technical Paper*, *890836.*

[23] **Kovach, J.**, **Tsakiris, E. and Wong, L.** (1982). Engine friction reduction for improved fuel economy, *SAE Technical Paper*, *820085.*

[24] **Hamai, K.**, **Masuda, T.**, **Goto, T. and Kai, S.** (1991). Development of a friction prediction model for high performance engines, *Lubrication Engineering*, *47*(7), 567–573.

[25] **Greenwood, J. and Tripp, J.** (1970). The contact of two nominally flat rough surfaces, *Proceedings of the Institution of Mechanical Engineers*, *185*(1), 625–633.

[26] **Zhu, D.**, **Hu, Y.**, **Cheng, H.**, **Arai, T. and Hamai, K.** (1993). A numerical analysis for piston skirts in mixed lubrication — Part II: Deformation considerations, *ASME. J. Tribol.*, *115*(1), 125–133.

[27] **Keribar, R. and Dursunkaya, Z.** (1992). A comprehensive model of piston skirt lubrication, *SAE Technical Paper*, *920483*.

[28] **Dursunkaya, Z. and Keribar, R.** (1992). Simulation of secondary dynamics of articulated and conventional piston assemblies, *SAE Technical Paper*, *920484*.

[29] **Dursunkaya, Z.**, **Keribar, R. and Ganapathy, V.** (1994). A model of piston secondary motion and elastohydrodynamic skirt lubrication, *ASME Journal of Tribology*, *116*, 777–785.

[30] **Wong, V.W.**, **Tian, T.**, **Lang, H.**, **Ryan, J.P.**, **Sekiya, Y.**, **Kobayashi, Y. and Aoyama, S.** (1994). A numerical model of piston secondary motion and piston slap in partially flooded elastohydrodynamic skirt lubrication, *SAE Technical Paper*, *940696*.

[31] **Kimura, T.**, **Takahashi, K. and S., S.** (1999). Development of a piston secondary motion analysis program with elastically deformable piston skirt, *SAE Technical Paper*, *1999-01-3303*.

[32] **Etsion, I. and Gommed, K.** (1995). Improved design with non-cylindrical profiles of gas-lubricated ringless piston, *ASME Journal of Tribology*, *117*, 143–147.

[33] **Prata, A.T.**, **Fernandes, J.R.S. and Fagotti, F.** (2000). Dynamic analysis of piston secondary motion for small reciprocating compressors, *Transactions of The ASME*, *122*, 752–760.

[34] **Scholz, B. and Bargende, M.** (2001). A hydrodynamic contact algorithm, *SAE Technical Paper*, *2001-01-3596*.

[35] **Chung, Y.**, **Schock, H.J. and Brombolich, L.J.** (1993). Fire ring wear analysis for a piston engine, *SAE Technical Paper*, *930797*.

[36] **Yun, J.E.**, **Chung, Y.**, **Chun, S.M. and Lee, K.Y.** (1995). An application of simplified average Reynolds equation for mixed lubrication analysis of piston ring assembly in an internal combustion engine, *SAE Technical Paper*, *952562*.

[37] **Stanley, R.**, **Taraza, D.**, **Henein, N. and Bryzik, W.** (1999). Analytical solution of piston ring pack lubrication for truck air brake compressor, *SAE Technical Paper*, *1999-01-0974*.

[38] **Zhang, Y.**, **Chen, G. and Li, B.** (1999). Two-dimensional numerical analysis of piston ring lubrication of an internal combustion engine, *SAE Technical Paper*, *1999-01-1222*.

[39] **Akalin, O. and Newaz, G.M.** (2001). Piston ring-cylinder bore friction modeling in mixed lubrication regime: Part I-Analytical results, *ASME Journal of Tribology*, *123*, 211–218.

[40] **Akalin, O. and Newaz, G.M.** (2001). Piston ring-cylinder bore friction modeling in mixed lubrication regime: Part II-Correlation with bench test data, *ASME Journal of Tribology*, *123*, 219–223.

[41] **Akalin, O. and Newaz, G.M.** (1998). A new experimental technique for friction simulation in automotive piston ring and cylinder liners, *SAE Technical Paper*, *981407*.

[42] **Dellis, P. and Arcoumanis, C.** (2004). Cavitation development in the lubricant film of a reciprocating piston–ring assembly, *Journal of Engineering Tribology*, *218*, 157–171.

[43] **Ma, M.T.**, **Sherrington, I. and Smith, E.H.** (1996). Implementation of an algorithm to model the starved lubrication of a piston ring in distorted bores: Prediction of oil flow and onset of gas blow-by, *Journal of Engineering Tribology*, *210*, 29–44.

[44] **Reynolds, O.** (1886). On the theory of lubrication and its application to Mr. Beauchamp Tower's experiments, including an experimental determination of the viscosity of olive oil, *Philosophical Transactions of the Royal Society of London*, *177*, 157–234.

[45] **Swift, H.W.** (1932). The stability of lubricating films in journal bearings, *Minutes of the Proceedings*, *233*, 267–288.

[46] **Stieber, W.** (1933). *Das Schwimmlager: Hydrodynamische Theorie des Gleitlagers*, VDI-Verlag GMbH.

[47] **Dowson, D.**, **Economou, P.N.**, **Ruddy, B.L.**, **Strachan, P.J. and Baker, A.J.S.** (1979). Piston ring lubrication - Part II; Theoretical analysis of a single ring and a complete ring pack, *Energy Conservation Through Fluid Film Lubrication Technology: Frontiers in Research and Design*, 23–52.

[48] **Dowson, D. and Taylor, C.** (1979). Cavitaion in bearings, *Annual Review of Fluid Mechanics*, *11*, 35–66.

[49] **Coyne, J.C. and Elrod, H.G.** (1970). Conditions for the rupture of a lubricating film. – Part I: Theoretical model, *Journal of Lubrication Technology*, *92*, 451–456.

[50] **Coyne, J.C. and Elrod, H.G.** (1970). Conditions for the rupture of a lubricating film. – Part II: New boundary conditions for Reynolds equation, *Journal of Lubrication Technology*, *93*, 156–167.

[51] **Wakuri, Y.**, **Soejima, M. and Taniguchi, T.** (1978). Oil film behavior of piston rings (Correction of effective pressure region of oil film), *Bulletin of the JSME-Japan Society of Mechanical Engineers*, *21*(152), 295–302.

[52] **Richardson, D. and Borman, G.** (1992). Theoretical and experimental investigations of oil films for application to piston ring lubrication, *SAE Technical Paper*, *922341*.

[53] **Taylor, R.**, **Brown, M.**, **Thompson, D. and J.C., B.** (1994). The influence of lubricant rheology on friction in the piston ring-pack, *SAE Technical Paper*, *941981*.

[54] **Wu, C. and Zheng, L.** (1989). An average Reynolds equation for partial film lubrication with a contact factor, *ASME Journal of Tribology*, *111*(1), 188–191.

[55] **Broyden, C.G.** (1965). A class of methods for solving nonlinear simultaneous equations, *Mathematics of Computation*, *19*(92), 577–593.

[56] **Broyden, C.G.** (2000). On the discovery of the “Good Broyden” method, *Mathematical Programming*, *87*(2), 209–213.

[57] **Hu, Y.**, **Cheng, H.S.**, **Arai, T.**, **Kobayashi, Y. and Aoyama, S.** (1994). Numerical simulation of piston ring in mixed lubrication – A nonaxisymmetrical analysis, *ASME Journal of Tribology*, *116*(1), 470–478.

APPENDICES

APPENDIX A : Flow Factors for a Rough Surface
APPENDIX B : Piston Trajectories

APPENDIX A

Flow Factors for a Rough Surface

Patir and Cheng [11] suggests flow factors to be used in the average Reynolds equation to model the effect of surface roughness on the flow of the fluid between two sliding surfaces equation 2.21.

Surface roughness orientation factor is defined as:

$$\gamma = \frac{\lambda_{0.5x}}{\lambda_{0.5y}} \tag{A.1}$$

where $\lambda_{0.5x}$ and $\lambda_{0.5y}$ are the lengths at which auto-correlation of a profile reduces to 50% of its initial value in the longitudinal, x- and transversal, y-directions, respectively. Schematics of surfaces with different orientation factor values are given in Figure A.1. These three surfaces might have equal surface roughness values but their resistance or contribution to the flow differs significantly.

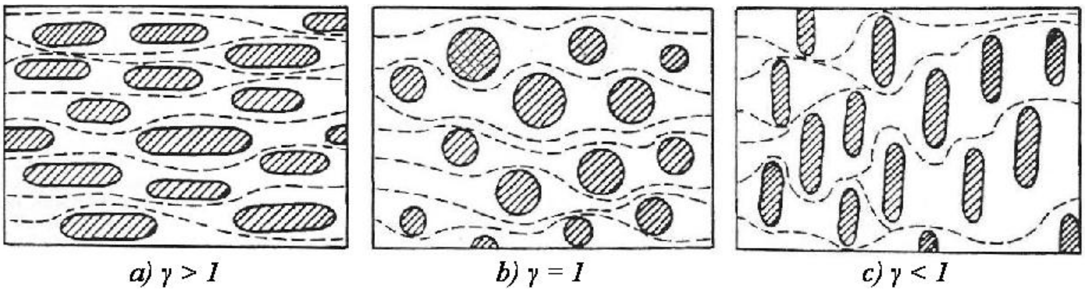

Figure A.1 : Typical contact areas for a) longitudinally oriented, b)isotropic and c) transversely oriented surfaces [11]

Variation of pressure flow factor with film thickness ratio is shown in Figure A.2 for different roughness orientations. It can be calculated with equation A.2 using the coefficients given in Table A.1.

Table A.1 : Coefficients of equation A.2 for pressure flow factor [1].

γ	C	r	Range
1/9	1.480	0.42	$H_\sigma > 1$
1/6	1.380	0.42	$H_\sigma > 1$
1/3	1.180	0.42	$H_\sigma > 0.75$
1	0.900	0.56	$H_\sigma > 0.5$
3	0.225	1.50	$H_\sigma > 0.5$
6	0.520	1.50	$H_\sigma > 0.5$
9	0.870	1.50	$H_\sigma > 0.5$

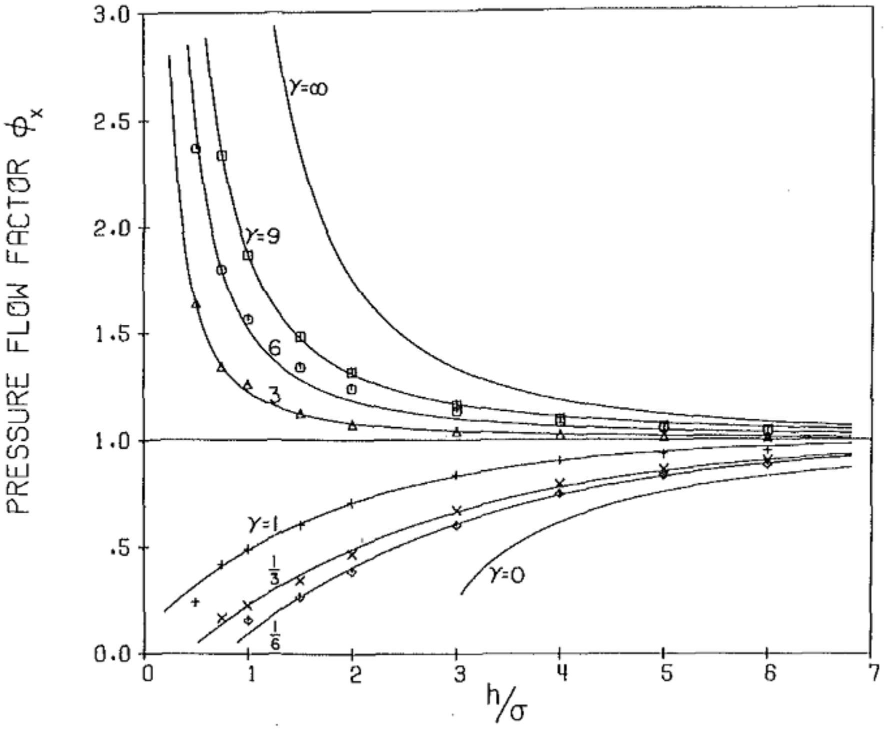

Figure A.2 : Pressure flow factor [1]

$$\phi_x = \begin{cases} 1 - Ce^{-rH_\sigma} & \gamma \leq 1 \\ 1 + CH_\sigma{}^{-r} & \gamma > 1 \end{cases} \tag{A.2}$$

The expression is written for x-direction. Pressure flow factor in y-direction can also be calculated with the same expression such that:

$$\phi_y(H_\sigma, \gamma) = \phi_x(H_\sigma, \frac{1}{\gamma}) \tag{A.3}$$

Shear flow factor can be calculated by:

$$\phi_s = V_{r1}\Phi_s(H_\sigma, \gamma_1) - V_{r2}\Phi_s(H_\sigma, \gamma_2) \tag{A.4}$$

where

$$V_{r1} = \left(\frac{\sigma_1}{\sigma}\right)^2 \tag{A.5a}$$

$$V_{r2} = \left(\frac{\sigma_2}{\sigma}\right)^2 = 1 - V_{r1} \tag{A.5b}$$

and Φ_s is a parameter which is also called shear flow factor. However, one should keep in mind that Φ_s is associated with a single surface, while ϕ_s is for the combination of two surfaces brought together. Φ_s is shown in Figure A.3 and it can be calculated using equation A.6 whose coefficients are given in Table A.2.

$$\Phi_s = \begin{cases} A_1 H_\sigma{}^{\alpha_1} e^{-\alpha_2 H_\sigma + \alpha_3 H_\sigma{}^2} & H_\sigma \leq 5 \\ A_2 e^{-0.25 H_\sigma} & H_\sigma > 5 \end{cases} \tag{A.6}$$

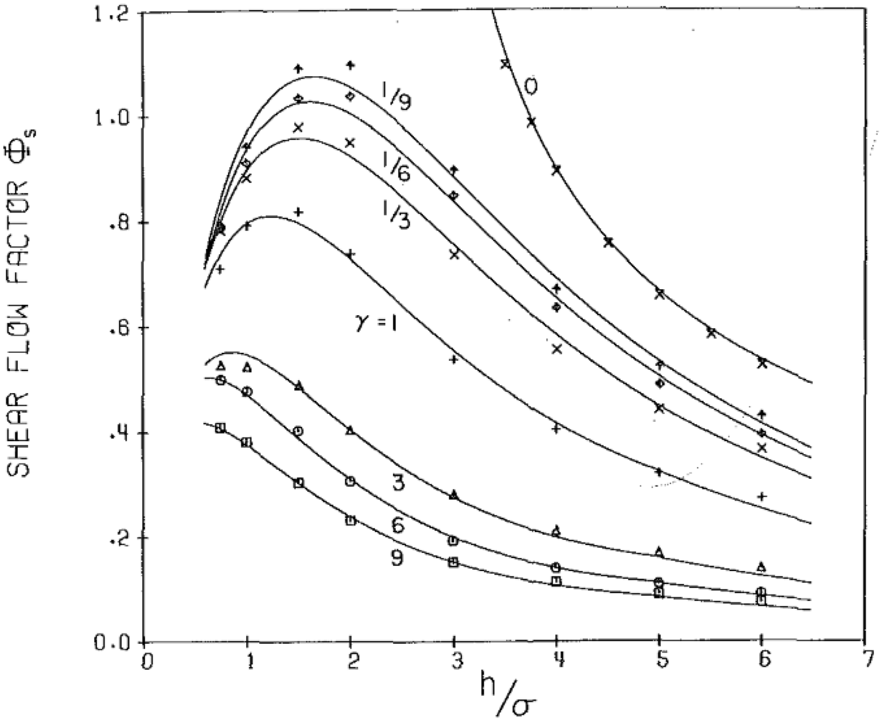

Figure A.3 : Shear flow factor [1]

Table A.2 : Coefficients of equation A.6 for shear flow factor Φ_s for the range $H_\sigma > 0.5$ [1].

γ	A_1	α_1	α_2	α_3	A_2
1/9	2.046	1.12	0.78	0.03	1.856
1/6	1.962	1.08	0.77	0.03	1.754
1/3	1.858	1.01	0.76	0.03	1.561
1	1.899	0.98	0.92	0.05	1.126
3	1.560	0.85	1.13	0.08	0.556
6	1.290	0.62	1.09	0.08	0.388
9	1.011	0.54	1.07	0.08	0.295

Contact Pressure and Viscous Shear Stress for a Rough Surface

Solid-to-solid contact pressure can be calculated with the asperity contact model of Greenwood and Tripp [25] which was given in equation 2.26 where

$$K = \frac{16\sqrt{2}}{15}\pi(N\beta'\sigma)\sqrt{\frac{\sigma}{\beta'}} \tag{A.7}$$

and

$$E' = \frac{1}{\dfrac{1-V_{r1}{}^2}{E_1} + \dfrac{1-V_{r2}{}^2}{E_2}} \tag{A.8}$$

is the composite Young's modulus. In equation A.7, N is the number of asperities per unit contact area and β' is the asperity radius of curvature. $F_{2.5}(H_\sigma)$ is the probability distribution of asperity heights. For the surface roughness with Gaussian distributed asperities, this formula is simplified by Hu et al. [57] as follows:

$$F_{2.5}(H_\sigma) = \begin{cases} A(\Omega - H_\sigma)^2 & H_\sigma \leq \Omega \\ 0 & H_\sigma > \Omega \end{cases} \tag{A.9}$$

where $\Omega = 4.0$, $A = 4.4068x10^{-5}$ and $Z = 6.804$. The authors of the same study also defines K in Eq. 2.26 as $1.198x10^{-4}$.

The formula for viscous shear stress on the rough skirt surface which is defined by Patir and Cheng [1] is given in equation 2.27.

In this formula, shear stress factor, ϕ_{fs}, is a correction term which arises from the combined effect of roughness and sliding, similar to the ϕ_s (equation A.4) in the mean flow. The functional dependence of ϕ_{fs} on the roughness parameters is also similar to that of ϕ_s:

$$\phi_{fs} = V_{r1}\Phi_{fs}(H_\sigma, \gamma_1) - V_{r2}\Phi_{fs}(H_\sigma, \gamma_2) \tag{A.10}$$

Φ_{fs} can be calculated using equation A.11. Coefficients of the equation are presented in Table A.3. The variation of Φ_{fs} with H_σ for different γ values is shown in Figure A.4.

$$\Phi_{fs} = \begin{cases} A_3 {H_\sigma}^{\alpha_4} e^{-\alpha_5 H_\sigma + \alpha_6 {H_\sigma}^2} & ,0.5 < H_\sigma \leq 7 \\ 0 & ,H_\sigma > 7 \end{cases} \tag{A.11}$$

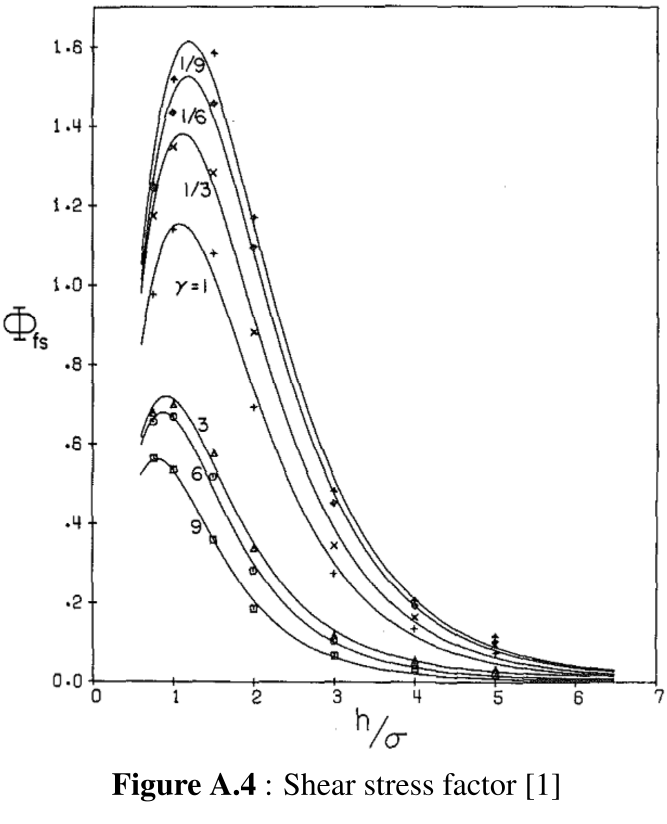

Figure A.4 : Shear stress factor [1]

Table A.3 : Coefficients of equation A.10 for shear stress factor Φ_{fs} for the range $0.5 < H_\sigma < 7$ [1].

γ	A_3	α_4	α_5	α_6
1/9	14.1	2.45	2.30	0.10
1/6	13.4	2.42	2.30	0.10
1/3	12.3	2.32	2.30	0.10
1	11.1	2.31	2.38	0.11
3	9.8	2.25	2.80	0.18
6	10.1	2.25	2.90	0.18
9	8.7	2.15	2.97	0.18

ϕ_f is another correction factor that arises from averaging the sliding velocity component of the shear stress. Details, as well as the following formula written in a suitable form for efficient numerical calculation, can be found in [1].

$$\phi_f = \begin{cases} \frac{35}{32} z \left[\left(1 - z^2\right)^3 \ln \frac{z+1}{\in^*} + A_4 \right] & , H_\sigma \leq 3 \\ \frac{35}{32} z \left[\left(1 - z^2\right)^3 \ln \frac{z+1}{z-1} + A_5 \right] & , H_\sigma \leq 3 \end{cases} \tag{A.12}$$

where

$$A_4 = \frac{1}{60} \left[-55 + z\left(132 + z\left(345 + z\left(-160 + z\left(-405 + z\left(60 + 147z\right)\right)\right)\right)\right) \right] \tag{A.13}$$

$$A_5 = \frac{z}{15} \left[66 + z^2 \left(30z^2 - 80\right) \right] \tag{A.14}$$

$$z = \frac{H_\sigma}{3} \tag{A.15}$$

$$\in^* = \frac{1}{300} \tag{A.16}$$

APPENDIX B

Piston Trajectories for Partially-Flooded Inlet

The following figures show piston trajectories for a complete power cycle for the cases with partially-flooded inlet.

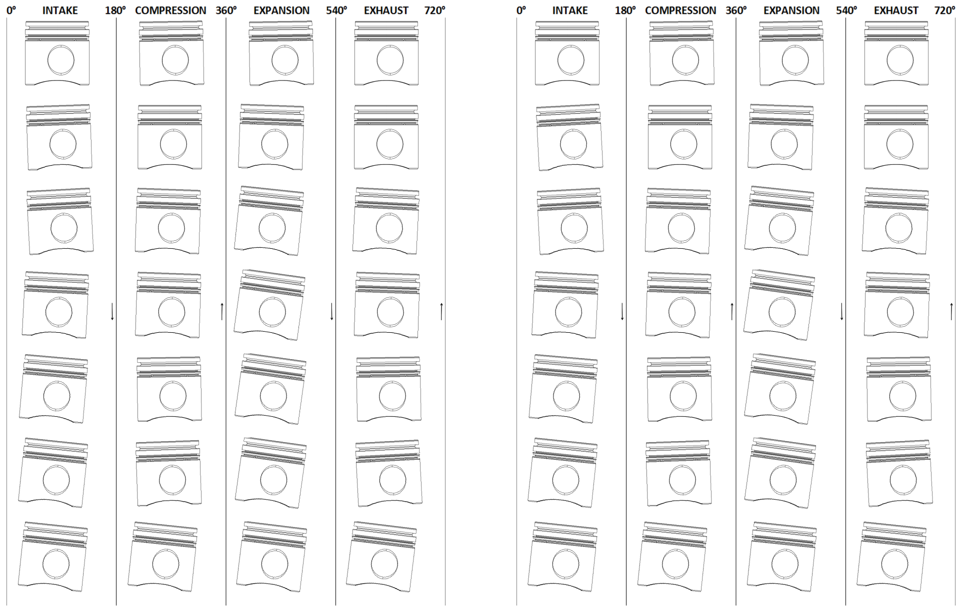

(a) 10W-50 (b) 10W-40 (baseline)

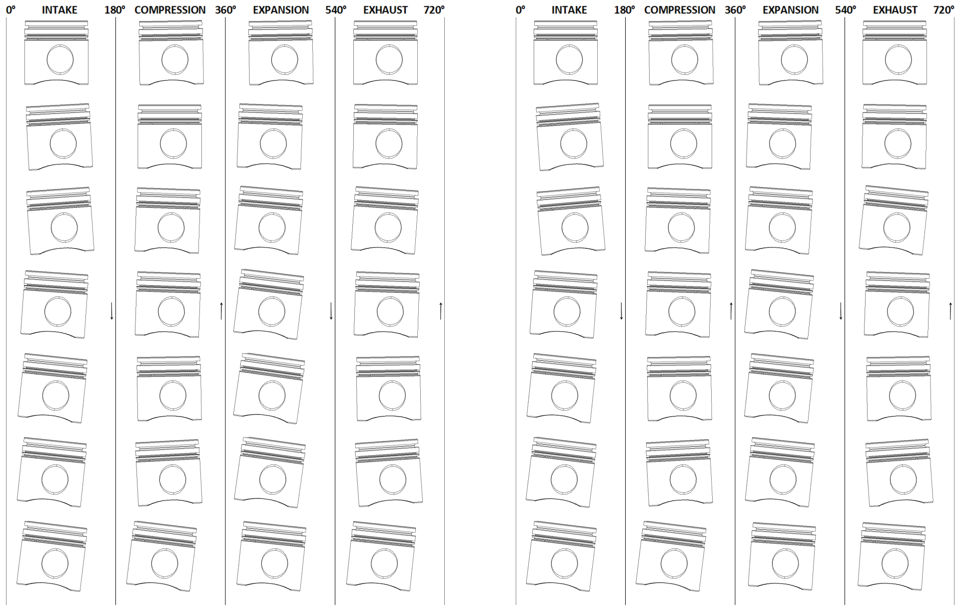

(c) 10W-30 (d) 10W-20

Figure B.1 : Piston trajectory for the change in oil viscosity (partially-flooded inlet).

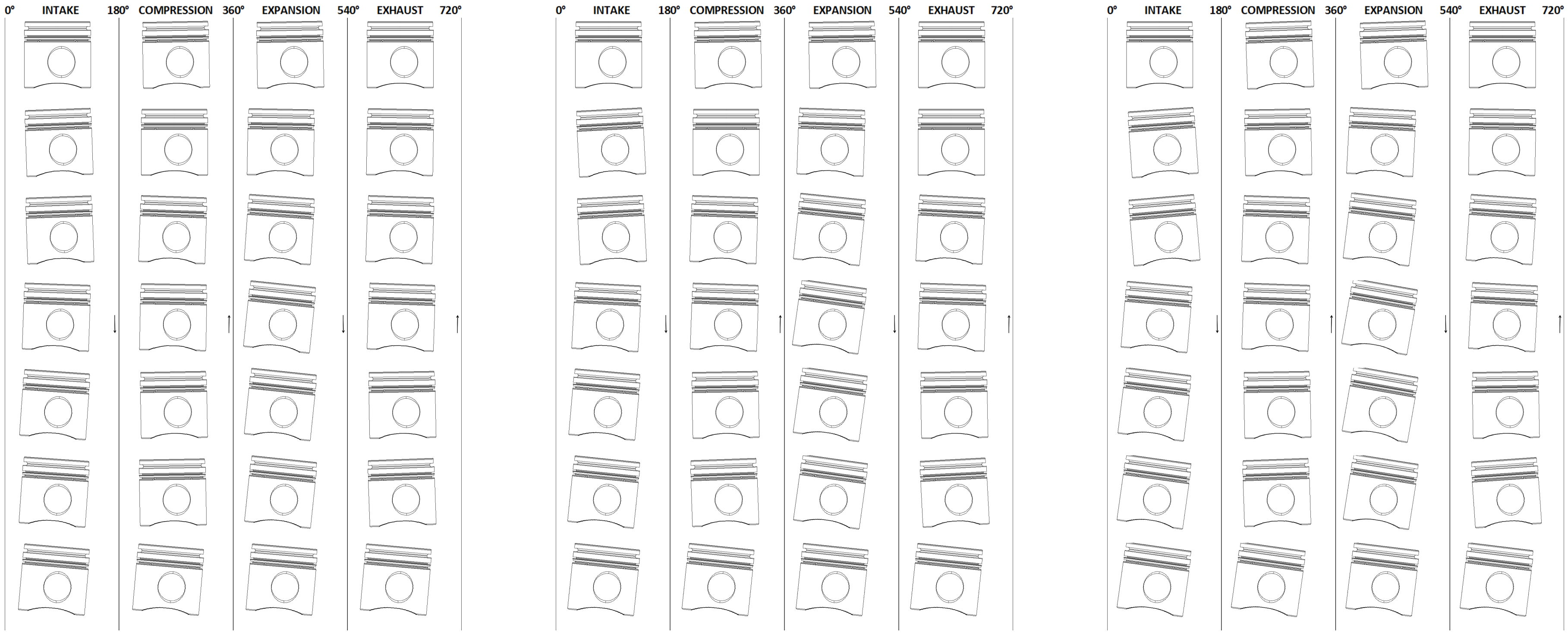

(a) Reduced barrel profile (b) Baseline barrel profile (c) Increased barrel profile

Figure B.2 : Piston trajectory for the change in barrel profile (partially-flooded inlet).

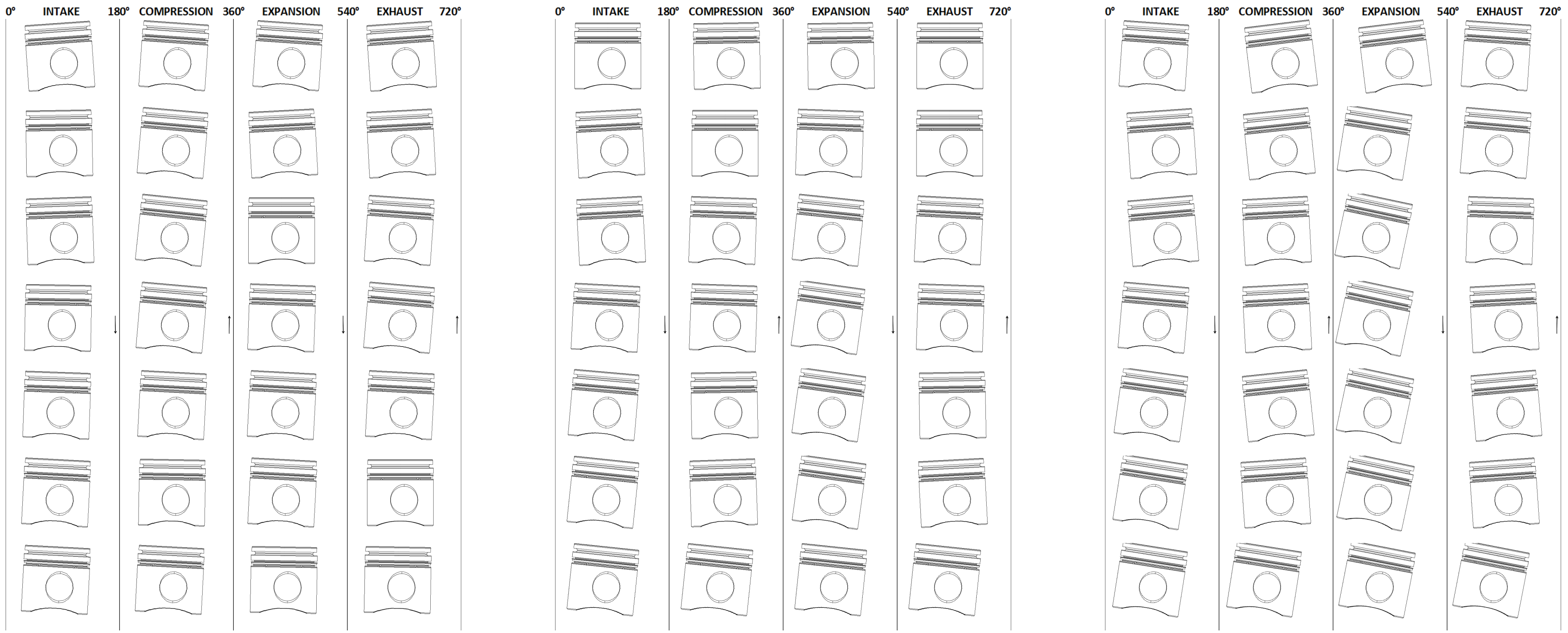

(a) Higher apex location (b) Baseline apex location (c) Lower apex location

Figure B.3 : Piston trajectory for the change in apex location (partially-flooded inlet).

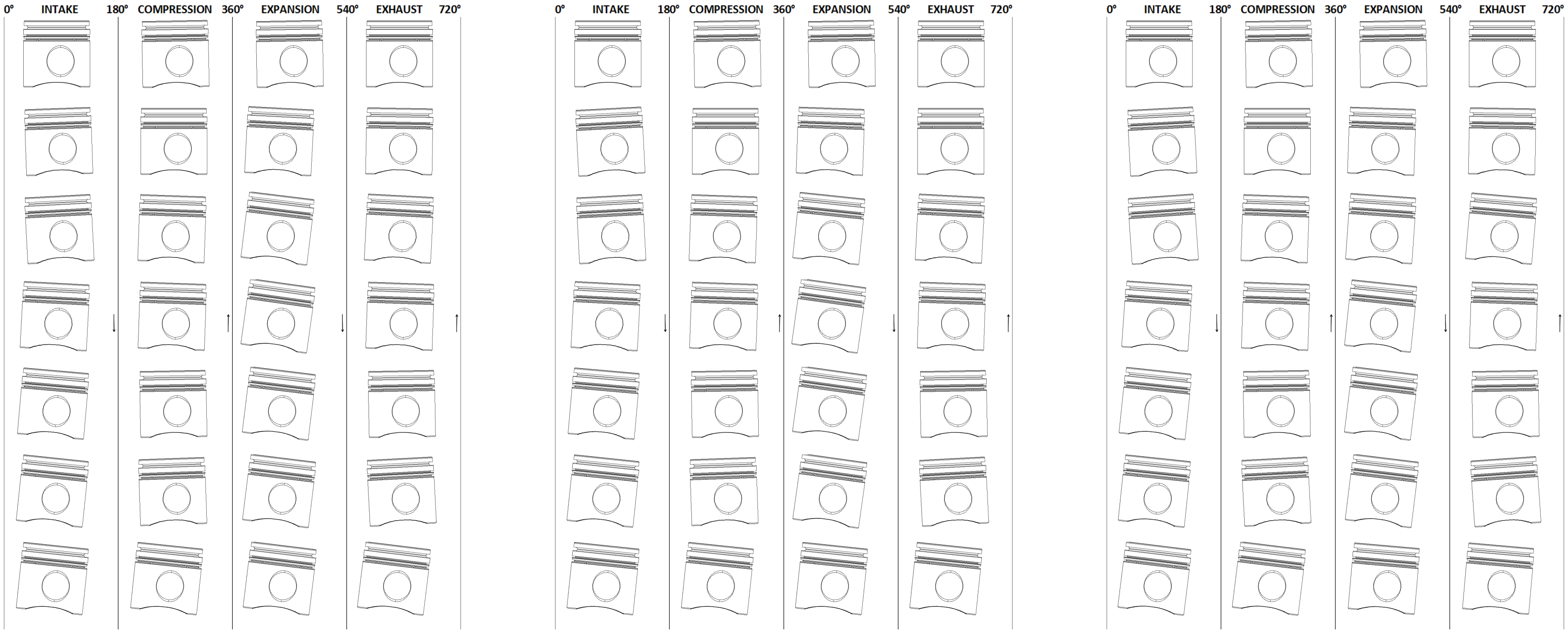

(a) Reduced oval profile

(b) Baseline oval profile

(c) Increased oval profile

Figure B.4 : Piston trajectory for the change in oval profile (partially-flooded inlet).

Piston Trajectories for Fully-Flooded Inlet

The following figures show piston trajectories for a complete power cycle for the cases with fully-flooded inlet.

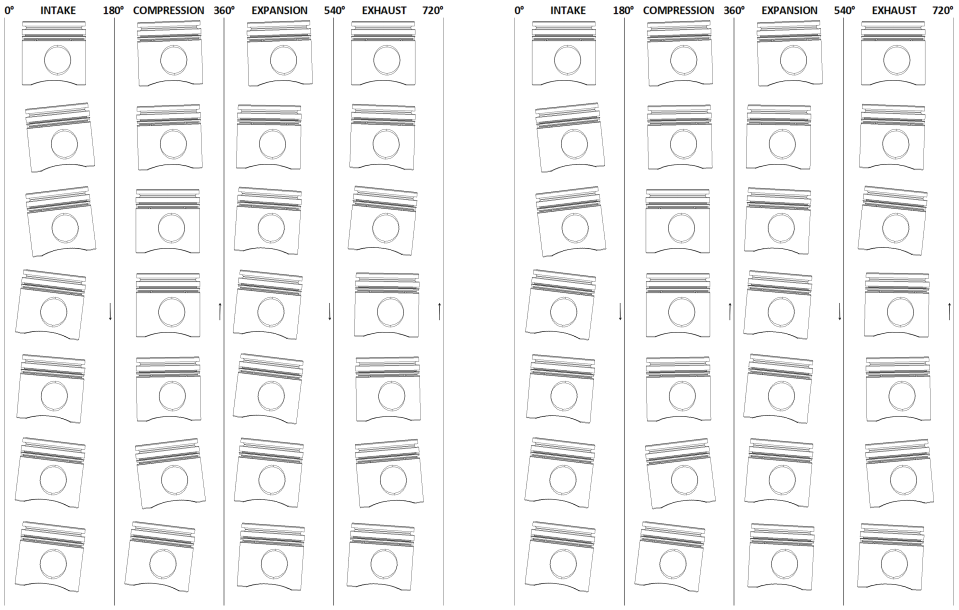

(a) 10W-50 (b) 10W-40 (baseline)

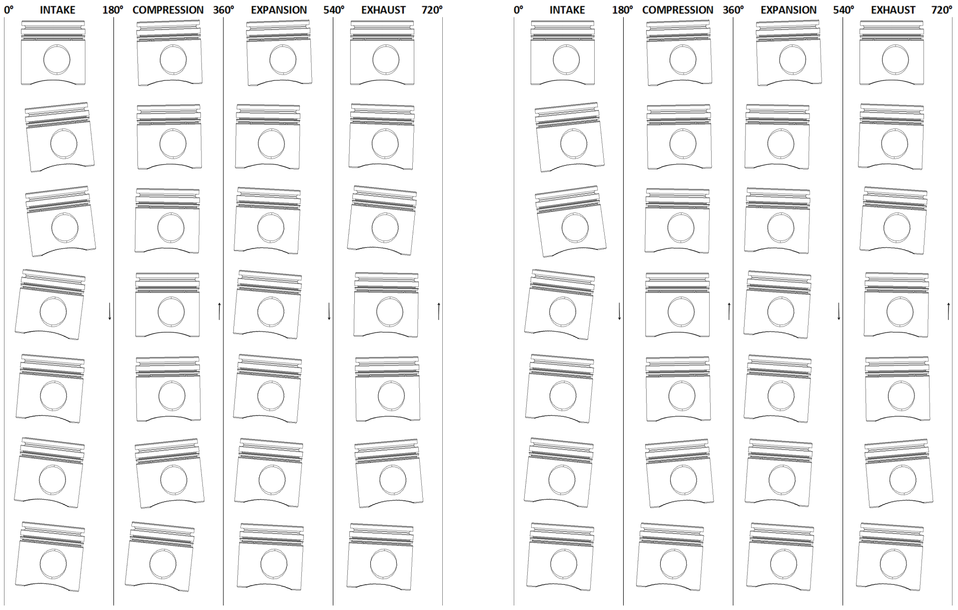

(c) 10W-30 (d) 10W-20

Figure B.5 : Piston trajectory for the change in oil viscosity (fully-flooded inlet).

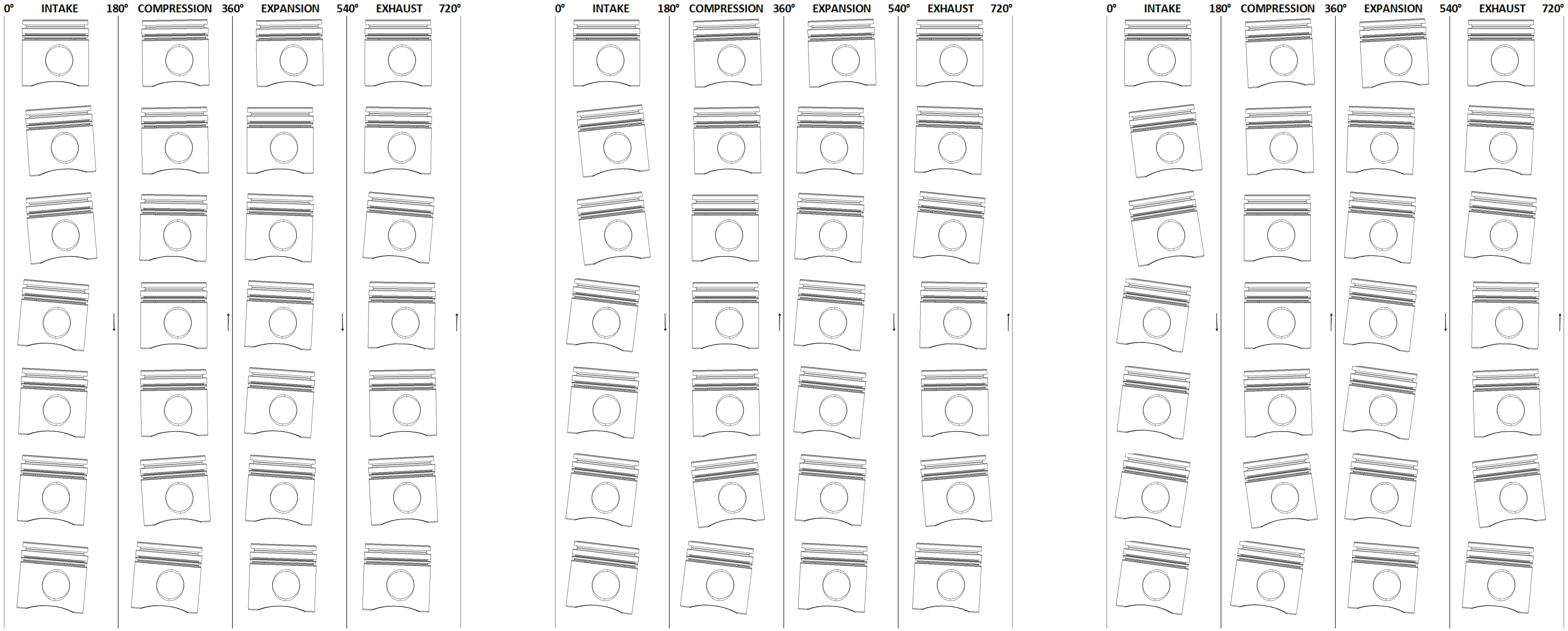

(a) Reduced barrel profile (b) Baseline barrel profile (c) Increased barrel profile

Figure B.6 : Piston trajectory for the change in barrel profile (fully-flooded inlet).

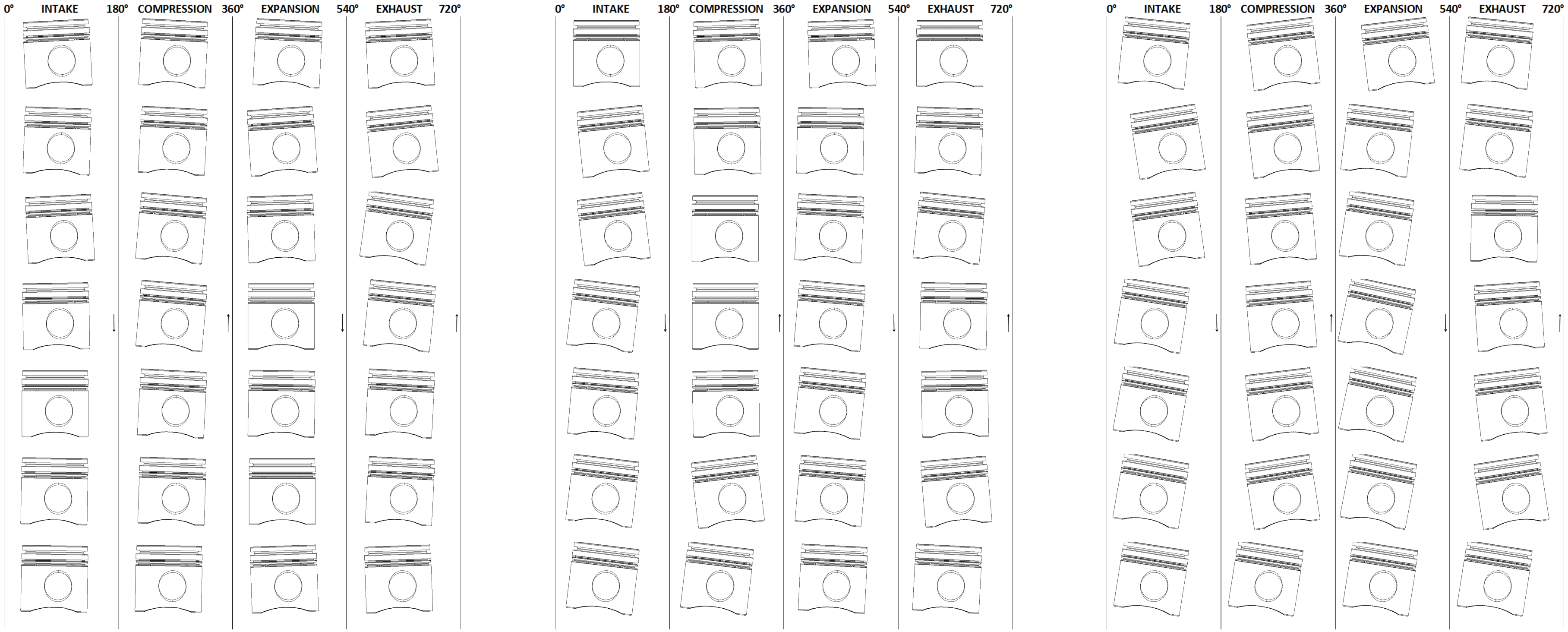

(a) Higher apex location (b) Baseline apex location (c) Lower apex location

Figure B.7 : Piston trajectory for the change in apex location (fully-flooded inlet).

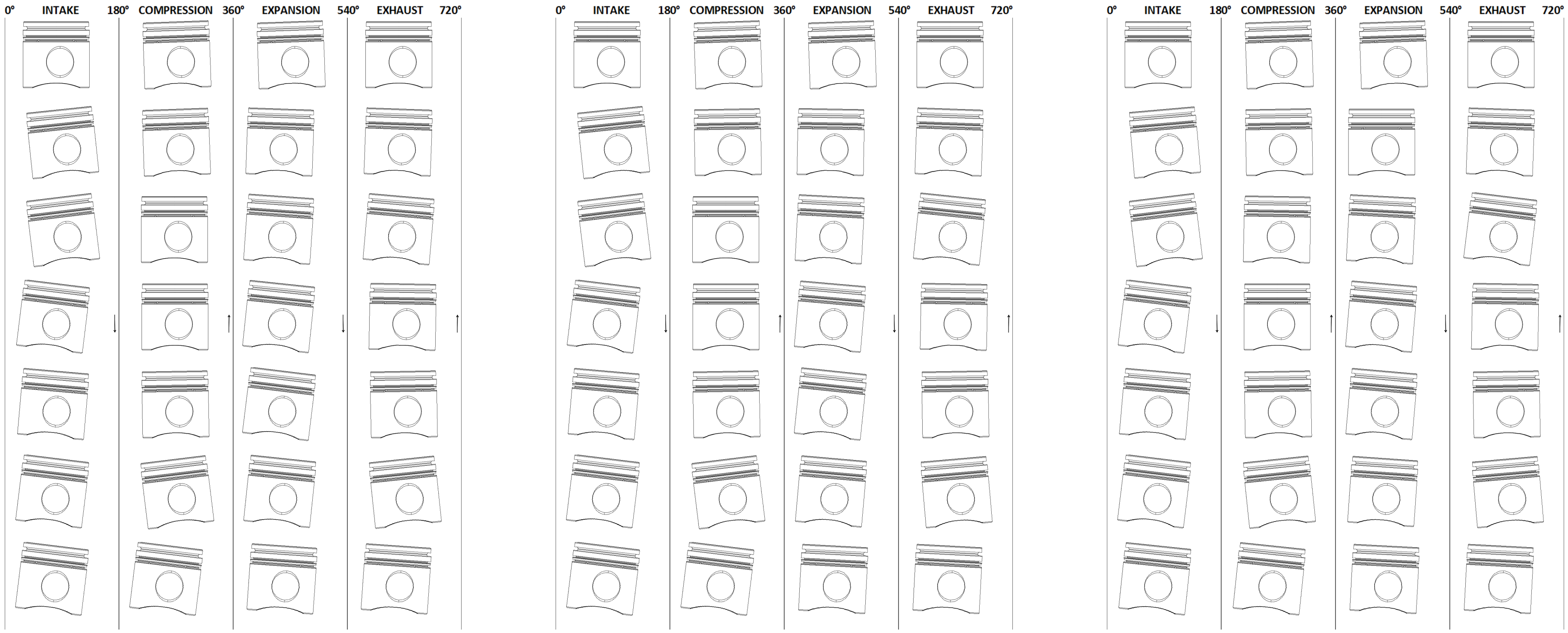

(a) Reduced oval profile (b) Baseline oval profile (c) Increased oval profile

Figure B.8 : Piston trajectory for the change in oval profile (fully-flooded inlet).

CURRICULUM VITAE

Name Surname: Özgür Günelsu

Place and Date of Birth: İzmit - 20 May 1980

Adress: İYTE Gülbahçe Yerleşkesi, Makina Mühendisliği Bölümü, 35430 Urla / İzmir / Türkiye

E-Mail: gunelsu@gmail.com

B.Sc.: Mechanical Engineering, Middle East Technical University - 2003

M.Sc.: Mechanical Engineering, Istanbul Technical University - 2006

Professional Experience and Rewards:

List of Publications and Patents:

PUBLICATIONS/PRESENTATIONS ON THE THESIS

- **Günelsu Ö.** and Akalın Ö. : Development of a Piston Secondary Motion Model for Skirt Friction Analysis. *Proceedings of the ASME Internal Combustion Engine Division 2012 Fall Technical Conference ICEF2012*, September 23-26, 2012, Vancouver, BC, Canada, ICEF2012-92166.
- **Günelsu Ö.** and Akalın Ö. : The Effects of Piston Skirt Profiles on Secondary Motion and Friction. *Journal of Engineering for Gas Turbines and Power*, June 2014, Vol. 136.